Statistical Mechanics of the Fluctuations of a Turbulent Quasi-Geostrophic Model of the Atmosphere: Instabilities and Feedbacks

Dissertation

with the aim of achieving a doctoral degree
at the Faculty of Mathematics, Informatics and Natural Sciences
Department of Earth Sciences

submitted by

Sebastian Schubert

in

Hamburg

2015

Day of oral defence: 4. November 2015

The following evaluators recommend the admission of the dissertation:
Prof. Dr. Valerio Lucarini
Prof. Dr. Gualtiero Badin

Abstract

Based on recent advances in dynamical system theory, we re-examine the variability in the mid latitudes induced by large scale baroclinic and barotropic processes. Classical approaches for investigating variability define an idealized background state and assess the stability of linear fluctuations in its vicinity or use the purely correlation based empirical orthogonal functions. Undoubtedly, these approaches have a great value for elucidating the relevant physical processes but they can not follow the evolution of a chaotic/turbulent atmosphere. The so-called covariant Lyapunov vectors (CLVs) provide a covariant basis which describes the directions of exponential expansion and decay of linear perturbations on a non-linear chaotic background. Their average growth rates equal the Lyapunov exponents (LE). We apply this extension of the classical stability analysis for the first time to a non-linearly evolving quasi-geostrophic (QG) model of the mid latitudes to re-examine the basic barotropic and baroclinic processes of the atmosphere. This QG model is a beta-plane two-layer model in a periodic channel driven by a forced meridional temperature gradient ΔT. We vary ΔT, representative for turbulence from relatively weak over intermediate to well-developed conditions.

By constructing the Lorenz energy cycle for each CLV, we identify a positive baroclinic conversion rate as a necessary but not sufficient condition of instability. Barotropic instability is present only for few very unstable CLVs for large values of ΔT. Slowly growing and decaying Lyapunov modes closely mirror some barotropic and baroclinic properties of the background flow. Following classical necessary conditions for barotropic/baroclinic instability, we find a clear relationship between the properties of the eddy fluxes of a CLV and its instability. CLVs with positive baroclinic conversion are potentially a useful set of modes which could be employed to construct a reduced model of the atmosphere dynamics.

In the next step, we extend the QG model by orography, in order to study fluctuations of the background state based on the emergence of blocking-like events. Blocking events in the mid latitudes atmosphere constitute a persistent deviation from the approximately zonally symmetric jet stream to the emergence of so-called blocking patterns. Such configurations are usually connected to exceptional local stability properties of the flow which are accompanied by an improved local forecast skill during the phenomenon. Yet, it is extremely hard to predict onset and decay of the pattern. Hence, we examine whether CLVs feature a signature of the blocking events and exploit that they are sensitive to orographic forcings.

Using a Tibaldi-Molteni scheme to detect blockings, we find that the global finite size LEs of the fastest growing CLVs are significantly higher than their long term averages. Thus, against intuitive expectations, the circulation is globally more unstable in blocked phases due to stronger barotropic and baroclinic conversion in the case of high temperature gradients. For low values of ΔT, the effect is only due to stronger barotropic conversion. In order to determine the localization of the

CLVs, we compare the meridionally averaged variance of the CLVs during blocked and unblocked phases. We find that on average the variance of the CLVs is clustered around the center of blocking. These results show that the blocked flow affects all time scales and processes described by the CLVs.

Our findings show that CLVs have a meaningful physical interpretation and provide a link between rather mathematical properties concerning the local direction of the stable and unstable manifold in autonomous system and the energetics of baroclinic and barotropic conversions. This opens new possibilities for exploiting dynamical system theory for applications in meteorology and geosciences regarding data assimilation, the correlations across multiple scales of motions and the partitioning of phase space with respect to their linear stability properties.

Zusammenfassung

Basierend auf neuen Entwicklungen in der Theorie der dynamischen Systeme, analysieren wir die Variabilität der mittleren Breiten der Erdatmosphäre, die durch großskalige barotrope und barokine Prozesse erzeugt wird. Klassische Methoden um diese Variabilität zu untersuchen basieren entweder darauf, einen Hintergrundzustand auszuwählen und die lineare Stabilität kleiner Störungen, beziehungsweise schwach nicht linearer Fluktuationen um diesen Zustand, zu bestimmen. Darüberhinaus, können die auf Korrelationen beruhenden, empirischen Orthogonalfunktionen untersucht werden. Es ist unbestreitbar, dass diese Methoden einen großen Anteil daran hatten und haben die relevanten physikalischen Prozesse zu erfassen. Jedoch besteht ein eher schwacher Zusammenhang der Dynamik der dort verwendeten Objekte mit der chaotischen/turbulenten Atmosphäre.

Die sogenannten kovarianten Lyapunov Vektoren (KLVs/CLVs) sind eine kovariante Basis des tangentiallinearen Raumes. Sie beschreiben die Richtungen des exponentiellen Wachstums und Abfalls einer linearen Störung auf einer nicht-linearen Lösung im Phasenraum. Die mittleren Wachstums-/Abfallraten entsprechen den Lyapunov Exponenten (LE). Diese Arbeit soll ein erstes Beispiel sein und demonstrieren, wie die hier vorgeschlagene Erweiterung der klassischen Stabilitätsanalyse angewandt wird auf ein sich nicht linear entwickelndes quasi-geostrophischen (QG) Modell der mittleren Breiten. Mit Hilfe der KLVs untersuchen wir dann die wesentlichen barotropen und baroklinen Prozesse in der Atmosphäre. Das QG Modell ist ein Zweischichtenmodel auf einem periodischen β Kanal und wird angetrieben durch einen vorgeschriebenen meridionalen Temperaturgradienten ΔT. Wir untersuchen verschiedene ΔT, welche das gesamte Spektrum der großskaligen Turbulenz abdecken von relativ schwachen bis hinzu gut entwickelten Bedingungen.

Wir entwickeln den Lorenz Energiezyklus für jeden KLV. Dieser beschreibt die Energieumwandlungen, die durch den Hintergrundzustand verursacht werden, als auch die Dissipation und Reibung, welche zum Verlust von Energie führen. Eine positive barokline Umwandlungsrate is eine notwendige aber nicht hinreichende Bedingung für Instabilität. Barotrope Instabilität wird nur für wenige KLVs beobachtet, wenn ΔT groß ist. Langsam wachsende und schrumpfende KLVs weisen in vielerlei Hinsicht ähnliche Eigenschaften wie der Hintergrundzustand auf. Klassischen notwendigen Bedingungen entsprechend für barokline/barotrope Instabilität, stellen wir eine klare Beziehung zwischen den Eigenschaften der Eddyflüsse der KLVs und deren Instabilität. KLVs mit positiver barokliner Energieumwandlung rekonstruieren verlässlich die Variabilität des Models und sind daher potentiell interessant um ein reduziertes Model der atmosphärischen Dynamik zu entwickeln.

Wir lassen dann die Analyse der langfristigen Variabilität hinter uns und erweitern das QG Model mit Orographie um Fluktuationen des Hintergrundzustandes an Hand von blockierten Großwetterlagen zu untersuchen. Die gaußförmige Orographie verstärkt die Entstehung von lokalisierten blockierten Lagen. Blockierte Lagen sind eine persistente Abweichung von dem mehr oder weniger zonal symmetrischen Jetstream. Solche Muster sind für gewöhnlich mit einer erhöhten lokalen Stabilität des Flusses verbunden, welche mit einer erhöhten Vorhersagequalität einhergeht. Allerdings ist es besonders schwer den Anfang und das Ende der blockierten Lage vorherzusagen. Deswegen ist es vielversprechend zu untersuchen, ob KLVs eine Signatur der blockierten Lagen aufzeigen, da sie sensitiv auf orographische Einflüsse reagieren.

Wenn die verwandte Tibaldi-Molteni Methode eine blockierende Lage detektiert, erhöht sich die Wachstumsrate der am schnellsten wachsenden KLVs signifikant. Dass heißt, entgegen der intuitiven Erwartungen, ist die globale Zirkulation instabiler während eines Blocks. Demzufolge erhöhen sich die lokalen LE im Vergleich zu den gemittelten LE. Dies wird verursacht durch eine erhöhte barokline und barotrope Umwandlungen im Falle höherer ΔT und alleinig durch die barotrope Umwandlung für niedrige ΔT. Um die Lokalisierung der KLVs zu untersuchen, bestimmen wir ihre meridional gemittelte Variabilität während der Blocks. Im Mittel sind sie verstärkt, um den Block herum lokalisiert. Wir schließen daraus, dass blockierte Lagen einen Zustand darstellen, der sich auf allen Zeitskalen und Prozessen, welche durch die KLVs beschrieben werden, auswirkt.

Die Ergebnisse dieser Arbeit zeigen, dass die KLVs sinnvoll physikalisch interpretiert werden können. Es kann eine Verbindung hergestellt werden zwischen einerseits den mathematischen Objekten (den KLVs), welche die stabile und instabile Mannigfaltigkeit tangential aufspannen und andererseits, der Energetik der baroklinen und barotropen Umwandlungen. Dies eröffnet neue Möglichkeiten dynamische Systemtheorie innerhalb der Meteorologie und Geowissenschaften anzuwenden hinsichtlich Datenassimilation, der Korrelationen hinweg über verschiedene zeitliche und räumliche Skalen der Dynamik und der Aufteilung des Phasenraums anhand der linearen Stabilitätseigenschaften.

Contents

Abstract **i**

Zusammenfassung **iii**

1 Introduction **1**
- 1.1 Motivation and Background 1
- 1.2 The Mid Latitudes Variability and Covariant Lyapunov Vectors . . 3
- 1.3 Weather Regimes and the Localization of Covariant Lyapunov Vectors 5

2 Covariant Lyapunov Vectors and Linear Stability Analysis **9**
- 2.1 Theory of Covariant Lyapunov Vectors 9
- 2.2 Application Of Covariant Lyapunov vectors In Dynamical System Theory 13
- 2.3 How to Compute Covariant Lyapunov Vectors 14

3 The Model and the Experimental Setup **17**
- 3.1 Description of the Model 17
- 3.2 The Experimental Setup 21
  - 3.2.1 Experiments without Orography in Chapter Four 21
  - 3.2.2 Experiments with Orography in Chapter Five 23

4 Instabilities and feedbacks of Covariant Lyapunov Vectors **25**
- 4.1 Atmospheric Circulation and the Lorenz Energy Cycle 25
- 4.2 The Lorenz Energy Cycle of Covariant Lyapunov Vectors 30
- 4.3 Physical Properties of Covariant Lyapunov Vectors 35
  - 4.3.1 The Lyapunov Spectra 35
  - 4.3.2 Results for the Lorenz Energy Cycle of Covariant Lyapunov Vectors 36
- 4.4 Explaining the Variability of the Background Flow 42
- 4.5 Summary and Discussion 45

5 Looking at Blocking Events using the formalism of Covariant Lyapunov Vectors **49**
- 5.1 Blocking Detection 49

5.2 Blocking Events 50
5.3 Properties of Covariant Lyapunov Vectors during Blocking 53
5.3.1 Linear Stability of Blocking States 54
5.3.2 Lorenz Energy Cycle during Blocking 57
5.3.3 Localization of Covariant Lyapunov Vectors 61
5.4 Summary and Discussion 65

6 Conclusion and Outlook 67

References xiv

Symbols xv

Acronyms xvii

Subscripts, Superscripts and Annotations xviii

List of Figures xxii

List of Tables xxiii

Acknowledgements xxv

Chapter 1

Introduction

1.1 Motivation and Background

In geophysics and meteorology in particular, we are almost exclusively confronted with high dimensional and chaotic systems. Predicting and understanding such systems has a high benefit for society when determining the influence of human activities and forecasting the huge variety of interconnected compartments of the earth system. Obviously, such an undertaking requires on the one hand observations of the real world and on the other hand theoretical investigations using computer simulations. Regarding the latter part, the increasing complexity and the vast number of coupled sub models make it increasingly hard to understand the mechanisms behind such systems (Held, 2005). It is therefore common scientific practice to employ a hierarchy of models from e.g. idealized models to full earth system models to investigate processes in the atmosphere, on the ocean or on land. For example, earth system models of intermediate complexity allow for demonstrating basic thermodynamic principles, study bi-stability of the climate and conduct broader surveys of climate impacts in various scenarios of climate change (see, e.g. Lucarini et al. (2010); Boschi et al. (2013); Holden et al. (2013)). Such results can then be used to substantiate results from the next level in the hierarchy, e.g. state-of-the-art earth system models. Moreover, a deeper understanding of the climate system is also offered by selecting tools and methods based on more mathematical concepts originating in dynamical system theory (Dymnikov and Filatov, 1996; Lucarini et al., 2014). Given that many methods, that dynamical system theory employs, are computationally expensive, we have to climb the hierarchy from below.

For these reasons, this thesis is not concerned with a model of the atmosphere that is realistic. Instead, we choose a model which captures essential processes in the large scale mid latitudes circulation and that is similar to the very old ”general circulation model” by Phillips (1956). Famously, in such simple quasi geostrophic (QG) models, the growth of small disturbances - the so-called normal modes - were investigated on idealized backgrounds of the mid latitudes atmosphere (Charney, 1947; Eady, 1949). Further studies of normal modes also included time-varying basic-states (Frederiksen, 1997) and more general but nevertheless fixed backgrounds (Eliassen, 1983). Different types of non-modal growth were also unraveled. Such can be created by superposition of modes (Cash and Lee, 2001) and non-hermitian Jacobians in e.g. shear flows (Volponi, 2005). These are unquestionable reasonable approaches to study stability of fixed states. In this thesis, we will instead investigate the properties of disturbances when growing on the asymptotic long term dynamics. This is an important improvement - as we will discuss further in this thesis - because small disturbances in fact grow on highly chaotic backgrounds instead of only feeding from energy of the already mentioned idealized states, like it is implied in e.g. Simmons and Hoskins (1978). In order to investigate such dynamics, we have to employ novel tools from dynamical system theory which allow for an investigation of the tangent linear dynamics on non-linearly evolving backgrounds. This was previously not possible, since no algorithms existed which could efficiently compute the so-called Covariant Lyapunov Vectors (CLVs) (Wolfe and Samelson, 2007; Ginelli et al., 2007). This basis of the tangent space is the only basis that can be interpreted in a physical way and their application is rather new for the meteorological community. Nevertheless, some results regarding Lorenz 96 models and the weakly non-linear QG model of Pedlosky (1987) already exist but they lack a thorough interpretation in terms of their physical interpretation (Wolfe and Samelson, 2007; Pazó et al., 2010). CLVs allow to access detailed information about the structure of the long-term statistically stationary climate of a dynamical system, the so called attracting set (Ruelle, 1980). They potentially allow for determining whether the long term dynamics can be embedded in an inertial manifold (Yang et al., 2009). Hence, CLVs have - apart from their mathematical value - high potential for applications in data assimilation and model reduction. Moreover, further benefits can be expected in ensemble predictions schemes (Pazó et al., 2010).

In order to contribute to the establishment of CLVs in meteorology, we will focus on the properties of CLVs from the perspective of meteorology. Aiming at this, we will generalize the concept of baroclinic and barotropic stability of normal modes following Eady and Charney and apply this to CLVs which growing on the non-linearly fluctuating atmosphere. We will explain in the remainder of this introduction in more detail the relation of CLVs to classical linear stability theory and what questions they can address beyond the classical approaches. More specifically, we will assess how this thesis will improve the understanding of the linear processes which contribute to creating the long-term variability in the mid latitudes (see Section 1.2) and how they characterize weather regimes like blocking events (see Section 1.3).

1.2 The Mid Latitudes Variability and Covariant Lyapunov Vectors

A classical example of dynamical meteorology and climate dynamics is the study of mid-latitude atmospheric variability and the investigation of the unstable eddies responsible for the synoptic weather. These unstable eddies affect predictability on time scales of the order of a few days and on spatial scales of the order of a few hundreds kilometers (Kalnay, 2003). They play a crucial climatic role of transporting heat poleward, therefore their accurate characterization is of utmost importance. Classical attempts at understanding their properties are based on linearization of some basic state and normal mode analysis, possibly extended to weakly non-linear regimes (Pedlosky, 1987) and on the provision of simple climatic closures (Stone, 1978), with stochastic models trying to fill the gap (Farrell and Ioannou, 1993). Two types of energy conversion between the background state and the fluctuations have been proposed. The first type, the barotropic instability, converts energy between the kinetic energy of the background state and the eddy field. As a result the momentum gradients in the background profile are reduced by an unstable barotropic process (Kuo, 1949). The second type of instability is related to the presence of a sufficient vertical shear in the background state (Charney, 1947; Eady, 1949; Kuo, 1952). The energetics of the so-called baroclinic instability is dominated by the following processes. The available potential energy of the zonal flow is converted into available potential energy of the eddy field, which is then converted into eddy kinetic energy. As a result of these processes, the center of mass of the atmosphere is lowered and heat is transported against the temperature gradient. Necessary instability conditions for the linear stability of generic zonal symmetric states are given by the Charney-Stern theorem (Charney and Stern, 1962; Eliassen, 1983). The baroclinic and barotropic energy conversions between the zonal mean and the eddies underpin the Lorenz energy cycle (LEC), thus providing the link between weather instabilities and climate (Lorenz, 1955; Lucarini, 2009; Lucarini et al., 2014), seen as a non-equilibrium steady state. Simple two layer QG models (Pedlosky, 1964; Phillips, 1954) provide a qualitative correct picture of the synoptic scale instabilities and energetics of the mid-latitude dynamics (Oort, 1964; Li et al., 2007).

The above described approaches study atmospheric variability based on defining a background state and studying the linear stability of the small fluctuations around such a state. Weakly non-linear theories can be constructed using higher order expansions terms. While these approaches provide useful insight into the mechanisms responsible for instabilities and the non-linear stabilization, they miss the crucial point of allowing for the investigation of the actual properties of the turbulent regimes, where the system evolves with time in a complex manner, and is far from being in the idealized base state considered in the instability analysis (Speranza and Malguzzi, 1988; Hussain, 1983).

This thesis approaches the problem of studying the instabilities of the atmosphere in a turbulent regime by taking advantage of some recent tools of dynamical systems theory and statistical mechanics, namely the CLVs (Ginelli et al., 2007; Wolfe and Samelson, 2007). These allow for studying linear perturbations of chaotic atmospheric flows and investigating the dynamics of the tangent space. In the past, Lyapunov vectors were proposed as bases to study the growth and decay of linear perturbations and to associate such features to the predictability of the flow and use them in data assimilation, see (Legras and Vautard, 1996; Kalnay, 2003). Ruelle (1979) first proposed the idea of a covariant splitting of the tangent linear space (see also Trevisan and Pancotti (1998)). The covariance of this basis is the critical property for a linear stability analysis, since the basis vectors can be seen as actual trajectories of linear perturbations. Moreover, the average growth rate of each CLV equals one of the Lyapunov exponents (LE). Note that the LEs describe the asymptotic expansion and decay rates of infinitesimal small perturbations of a chaotic trajectory (Eckmann and Ruelle, 1985) and have been studied extensively in meteorology . The CLVs provide explicit information about the directions of asymptotic growth and decay in the tangent linear space. For stationary states the CLVs reduce to the normal modes. In the case of periodic orbits the CLVs coincide with the Floquet vectors which for example have been obtained for the weakly unstable Pedlosky model (Samelson, 2001a). Samelson also extended this analysis to unstable periodic orbits (Samelson, 2001b).

Recently, new methods to compute CLVs for arbitrary chaotic trajectories have been developed by Ginelli et al. (2007) as well as Wolfe and Samelson (2006, 2007, 2008). We will give a short introduction to the theory of CLVs in Chapter two. For a comprehensive introduction we refer to Kuptsov and Parlitz (2012). These methods allow for computing CLVs for high dimensional chaotic systems and have led to a renewed interest in the related theory. CLVs have been successfully obtained for one and two dimensional systems (Yang et al., 2009; Yang and Radons, 2010; Takeuchi et al., 2011). Moreover, they have been studied for simple models of geophysical relevance (Pazó et al., 2010; Herrera et al., 2011) elucidating the potential benefits of CLVs in Ensemble Prediction Systems over bred vectors and orthogonal Lyapunov vectors. Note that by spanning the tangent space of the attractor, CLVs allow in principle a precise calculation of the response operator to an arbitrary perturbation of a dynamical system (Lucarini et al., 2014; Lucarini and Sarno, 2011; Ruelle, 2009). In Chapter four, we construct CLVs for the simple two layer QG model introduced by Phillips (1956) and consider three values of the equator-to-pole relaxation temperature difference ΔT, corresponding to low, medium, and high baroclinic forcing, and correspondingly developed turbulence (see Section 3.2.1). This is intended as a first step in the direction of studying a hierarchy of more complex models of geophysical flows. The model is introduced and its use justified in Chapter three.

It is of great interest to link the mathematical properties of the various CLVs to their energetics. Hence, a straightforward generalization of the concepts concerning baroclinic and barotropic conversions as part of a LEC developed for normal modes is desired. Thanks to covariance, we are able to construct the Lorenz energy cycle for each CLV, and then deduce the rate of barotropic and baroclinic energy conversion, as well as of frictional dissipation (see Section 4.2). In this way, we are able to associate the overall asymptotically growing or decaying property of each CLV to specific physical processes (see Section 4.3).
In Section 4.4, as a preliminary idea we take a first step towards a comparable concept employing CLVs. We investigate how much variance of the background trajectories can be explained by the CLVs. Usually, explaining the variability based on correlations employs Empirical Orthogonal Functions (EOFs) (Peixto and Oort, 1992) which can be used to construct models of reduced complexity (Selten, 1995; Franzke et al., 2005) because they are optimal vectors in phase space to explain the variance. The downside of this approach is that the EOFs are solely based on correlations and are not related to the actual dynamics of the flow. Therefore, CLVs are a much more interesting choice for this.

The study of the mid latitudes in a long term statistical sense is only the one part of this thesis. In the next subsection, we will therefore introduce how the CLVs can be employed to characterize persistent fluctuations of the background state as well.

1.3 Weather Regimes and the Localization of Covariant Lyapunov Vectors

The study of weather regimes in the atmosphere is a key topic in meteorology and geosciences. In particular, blocking highs have been early on identified as persistent, large scale deviations from the zonally symmetric general circulation (Baur, 1947; Rex, 1950). Traditionally, the detection and description of these events employs objective indicators based on pressure anomalies in the atmosphere obtained from observational data or output of general circulation models (Lejenäs and Økland, 1983; Tibaldi and Molteni, 1990; Schalge et al., 2011). Such blocking events and related large scale weather regimes provide an important contribution to the low frequency variability of the atmosphere. In particular, one can interpret the mid-latitude atmosphere as jumping between a zonal regime and a blocked regime, or, more in general, a regime where long waves are strongly enhanced (Benzi et al., 1986; Sutera, 1986; Molteni et al., 1988; Ruti et al., 2006; Majda et al., 2006; Franzke et al., 2008). One needs to remark that the so-called bi-modality theory as well as the analyses which have confirmed - at least partially - its validity have been criticized in the literature, see e.g. Nitsche et al. (1994) and Ambaum (2008). Charney and DeVore (1979) and Charney and Straus (1980) have speculated that the existence of multiple stationary equilibria in simple models of the atmospheric circulation is the root cause for weather regimes. In their investigation of highly truncated QG models, several stationary states exist due to an orographic forcing. Different weather regimes are then associated with the neighborhood of the various stationary states. Contrary to this theory of multiple equilibria, it was found that in less severely truncated models, which adopted realistic forcings, stationary states are far away from the attractor (Reinhold and Pierrehumbert, 1982; Tung and Rosenthal, 1985) and/or only one stationary state exists, as we have already pointed out in the previous section (Speranza and Malguzzi, 1988).

Coming from a dynamical system theory, the attempt to define atmospheric weather regimes is based on investigating the density of the attractor of a dynamical system. It is not surprising that in highly chaotic systems, a characterization of the full statistics of an attractor is not possible using a few stationary points. Therefore, the concept of switching between the neighborhood of unstable stationary states, can be generalized to the neighborhood of weakly unstable orbits to define weather regimes (Gritsun, 2013). Also, heteroclinic connections between unstable stationary states were found in a highly truncated barotropic model (Crommelin, 2003). In models with higher complexity ”ruins” of these structures are found and correlate with transitions between different weather regimes (Kondrashov et al., 2004; Sempf et al., 2007). In a reduced model phase space, this allows for identifying different dynamically stable weather regimes and less stable transitions paths between them (Tantet et al., 2015).

In this thesis, we will build upon the classical point of view on the dynamics of blocking, which focuses on the analysis of the linear instabilities of low-order models. Thus, we consider more earth-like - at least, qualitatively - background turbulent atmospheric conditions. While the attractors we consider are strange geometrical objects, we follow a mathematical approach such that we are able to stick to the investigation of linear stability properties. This allows for a relatively easy interpretation of the underlying physical mechanisms. Ever since Lorenz (1963), it is clear that linear stability is a measure of predictability of the atmosphere. Therefore, the difficulty of predicting - in time - the onset and decay of weather regimes and their persistence should be reflected in local stability properties. Consequently, blocking patterns have been assessed in regard of their linear stability properties in various bases. It is important to note, that for an analysis of linear perturbations a meaningful basis has to be chosen (Pazó et al., 2010). The analysis of optimal perturbations indicated that the leading optimal perturbation localizes where blocking occurs (Buizza and Molteni, 1996). In a study by Frederiksen (1997) normal modes for a time varying basic state were investigated. It was also found that blocking can only be explained by accounting for non-linear effects if linear perturbations of single states of the atmosphere are considered (Naoe and Matsuda, 2002).

In Chapter five, we will use CLVs to investigate this problem. Investigating linear stability of weather regimes with CLVs combines the benefits of the various mentioned approaches to linear stability. First, they possess the already mentioned benefits of covariance and they generalize the classical normal modes. Second and more importantly for models employing orographic forcings, the CLVs will respond to orographic disturbances (Szendro et al., 2008). Taking these points into consideration, it is suggestive to consider CLVs as a superior choice over other orthogonal, hence norm-dependent Lyapunov vectors for the studies of weather regimes enhanced by orographic forcings.

The analysis of a weather regime like blocking will complete the investigation of Chapter four. There, we will address how the average energy and momentum transports of the CLVs are related to their growth and decay in respect to the background state and how they explain the variance of the background state. This will provide a bridge between the growth rate of the CLVs and the physical mechanisms of instability of the quasi-geostrophic flow, namely the barotropic and baroclinic instability, as components of a detailed analysis of the Lorenz Energy cycle of each CLV. We note that our focus there will be exclusively on the long-term properties of the flow, of its CLVs, and of the corresponding LEs. Instead for the analysis of blocking events in Chapter five, we will be concerned with weather regimes in the background state, hence we will study the fluctuations of the CLVs and look at some properties of finite-time LEs. The rationale for the study of blockings is then the following. Using the classical Tibaldi-Molteni scheme blocking detection, we will determine when the flow is unblocked and when/where the flow switches to a blocked state (Tibaldi and Molteni, 1990). We will then address two questions. First, how do the growth rates of the linear perturbations change during blocked phases with respect to the regular zonal flow conditions and second, how does the localization of the CLVs change during blocking in the background state. Note that the second question is different from the average localization of the CLVs investigated in Szendro et al. (2008). In order to enhance blocking events, we will add an orographic forcing to our QG model (following (Charney and Straus, 1980), see Section 3.1). The orography in our investigation is a Gaussian bump in the middle of the domain with horizonal scale of $O(1000)\ km$. We explore the sensitivity of the problem by considering multiple setups featuring different heights of the gaussian bump and different values of ΔT of the baroclinic forcing, parameterized through a the relaxation temperature gradient (see Section 3.2.2). Again, every setup will exhibit chaotic conditions with many positive LEs.

Let us summarize how we continue after this introductory chapter. In Chapter two, we will explain the more precise mathematical background of the CLVs in order to show explicitly how they differ from other approaches and how they are applied in dynamical system theory. In Chapter three, we describe the QG model used in our studies and introduce the experimental setup. We then continue with the analysis of the mid latitudes variability and the energetics of the CLVs in Chapter four featuring a setup without orography. After this, in Chapter five, we use the model extended by an orographic forcing to investigate blocking events with the CLVs. In Chapter six, the thesis will be finished with a summary and concluding remarks which point towards future work.

Chapter 2

Covariant Lyapunov Vectors and Linear Stability Analysis

We start the chapter be laying a foundation for understanding the CLVs and their importance for characterizing the tangent linear dynamics. Before presenting the model used in our study in Chapter three and before beginning a detailed investigation of the model with the CLVs, we recapitulate the mathematical background of the CLVs in Section 2.1. Being a basis of all linear perturbations to a given background trajectory of a dynamical system, they fulfill two important properties. First, they are covariant, hence each element of the basis is a time-dependent solution to the tangent linear equation (see below Equation (2.3)). This means the basis vectors are linearized approximations of nearby evolving trajectories and we can identify physical processes between them and the background state[1]. Second, the long-term time average of the growth rates of the single CLVs is equal to the Lyapunov exponents. Consequently, they explore the whole tangent space of a dynamical system. This makes them extremely valuable in many fields of dynamical system theory which are also of interest in meteorology (see Section 2.2). In Section 2.3, we will then also explain in some more detail the algorithm used to compute the CLVs.

2.1 Theory of Covariant Lyapunov Vectors

Let us look at the mathematical concepts necessary to understand CLVs in some detail. For a much more complete and thorough discussion, we refer to a review paper on CLVs by Kuptsov and Parlitz (2012). We consider covariant linear perturbations of the non-linear autonomous dynamical system

$$\frac{\mathrm{d}}{\mathrm{d}t}\mathbf{x} = f(\mathbf{x}), \tag{2.1}$$

---

[1] An example of this is the LEC between the CLVs and the background state described in Section 4.2.

where $\mathbf{x} \in \mathbb{R}^n$. We perform a linear stability analysis by studying the evolution of an infinitesimal perturbation $\mathbf{v}$ to a solution $\mathbf{x}_B$ of equation 2.1. This means, that two assumptions are made. First, we assume $x_B + v$ is a solution of equation (2.1) and, second, we assume $\mathbf{v}$ to be small at all times. This allows for a first order expansion of the tendency equation around $\mathbf{x}_B$.

$$\begin{aligned} \frac{\mathrm{d}}{\mathrm{dt}}\left(\mathbf{x}_B + \mathbf{v}\right) &= f(\mathbf{x}_B + \mathbf{v}) \\ &\approx f\left(\mathbf{x}_B\right) + \sum_i \frac{\partial f_j}{\partial x_i}\left(\mathbf{x}_B\right)\ \mathbf{v}_i \end{aligned} \tag{2.2}$$

Therefore, in the limit, where $\mathbf{v}$ is infinitesimal, $\mathbf{v}$ obeys the tangent linear equation.

$$\frac{\mathrm{d}}{\mathrm{dt}}\mathbf{v}_j(t) = \sum_i \frac{\partial f_j}{\partial x_i}\left(\mathbf{x}_B(t)\right)\ \mathbf{v}_i(t) =: \sum_i \mathcal{J}_{ji}\left(\mathbf{x}_B(t)\right)\ \mathbf{v}_i(t). \tag{2.3}$$

Here, $\mathcal{J}$ is called the tangent linear operator or Jacobian of the system evaluated at $\mathbf{x}^B(t)$. Solutions of equation 2.3 are linear representations of nearby trajectories of $\mathbf{x}_B$.

We now would like to construct a covariant basis of n vectors and explain how they are able to span the tangent space, each associated to a specific Lyapunov exponent. For this we first define the propagator $\mathcal{F}$ which evolves linear perturbations through time if they are solutions of equation 2.3.

$$\mathbf{v}(t_2) = \mathcal{F}(t_2, t_1)\ \mathbf{v}(t_1) \tag{2.4}$$

Considering the asymptotic far future and far past of $\mathcal{F}$, bases of the tangent space can be constructed. The commonly used orthogonal forward and backward Lyapunov vectors (FLV, BLV) are derived from these limits and are the eigenvectors of the far past operator $W^-(t)$ (BLV) and the far future operator $W^+(t)$ (FLV).

$$\begin{aligned} W^-\left(t\right) &= \lim_{t' \to -\infty}\left[\mathcal{F}\left(t, t'\right)^{-T}\mathcal{F}\left(t, t'\right)^{-1}\right]^{\frac{1}{2(t-t')}} \\ W^+\left(t\right) &= \lim_{t' \to +\infty}\left[\mathcal{F}\left(t', t\right)^{T}\mathcal{F}\left(t', t\right)\right]^{\frac{1}{2(t'-t)}} \end{aligned} \tag{2.5}$$

Note that often the BLV are also called Gram-Schmidt vectors or just Lyapunov vectors. In the course of this thesis, we will refer to them mainly as BLV because this expression is much more precise. The eigenvectors of the far past operator are the BLV $B_j(t)$ and the eigenvalues are given in the form $e^{-\lambda_j}$, which means they have an asymptotic growth rate of λ_j in the interval $[-\infty, t]$. For the sake of simplicity we assume the multiplicity of all eigenvalues to be one. The λ_j are the LEs in descending order. We can span the so called backward subspaces in the following way $V_j^-(t) = span\{B_1(t), ..., B_j(t)\}$ (Osedelec, 1968). The meaning of the

BLV can be understood by the following examples. Starting at a time t at "minus infinity" with an arbitrary phase space volume $dv_k(t = -\infty)$ of dimension k, the final phase space volume at time t, the volume $dv_k(t)$, is a subset of the backward subspace $V_k^-(t)$. The average growth rate of the volume is proportional to the sum of the first k Lyapunov exponents.

$$\lim_{t' \to -\infty} \mathcal{F}(t,t')dv_k(t') \subset V_k^-(t) \tag{2.6a}$$

$$\lim_{t' \to -\infty} \mathrm{vol}(\mathcal{F}(t,t')dv_k(t')) \propto e^{\sum_{j=1}^{k} \lambda_j \cdot (t-t')} \tag{2.6b}$$

For the far future operator the relations are similar. The new eigenvectors F_j are the FLV and span the forward subspaces V_j^+. We have $V_j^+ = span\{F_{n-j+1}, ..., F_n\}$ and the eigenvalues are $e^{\lambda_{n-j+1}}$ which means they have an asymptotic growth rate of λ_{n-j+1} in the interval $[t, \infty]$. The interpretation is similar to the BLV.

$$\lim_{t' \to +\infty} \mathcal{F}(t',t)^{-1}dv_k(t') \subset V_{n-k+1}^+(t) \tag{2.7a}$$

$$\lim_{t' \to +\infty} \mathrm{vol}(\mathcal{F}(t',t)^{-1}dv_k(t')) \propto e^{\sum_{j=1}^{k} \lambda_j \cdot (t-t')} \tag{2.7b}$$

These two kinds of bases are not covariant with equation 2.3. Nevertheless, the backward and forward subspaces are covariant.

$$\begin{array}{ll} B_j(t_2) \neq \mathcal{F}(t_2,t_1)B_j(t_1) & V_j^-(t_2) = \mathcal{F}(t_2,t_1)V_j^-(t_1) \\ F_j(t_2) \neq \mathcal{F}(t_2,t_1)F_j(t_1) & V_j^+(t_2) = \mathcal{F}(t_2,t_1)V_j^+(t_1) \end{array} \tag{2.8}$$

Fortunately, we can use them to find a covariant basis (the CLVs). The easiest way to understand this is to rewrite the definition of the forward and backward subspaces by characterizing their elements with respect to their growth rates.

$$V_j^-(t) = \left\{ v \,\middle|\, \lim_{t' \to \infty} \frac{1}{t'} log\left(||v(t+t')||\right) \geq \lambda_j \right\} \tag{2.9a}$$

$$V_{n-j+1}^+(t) = \left\{ v \,\middle|\, \lim_{t' \to \infty} \frac{1}{t'} log\left(||v(t+t')||\right) \leq \lambda_j \right\} \tag{2.9b}$$

We know that the cut of covariant subspaces is covariant as well. Therefore, the cut of the subspaces $V_j^-(t)$ and $V_{n-j+1}^+(t)$ contains only vectors which have an asymptotic grow rate of λ_j on the interval $[-\infty, \infty]$. The cut should be exactly one dimensional if degeneracy is neglected and consistently the dimension of $V_j^-(t)$ is j and the dimension of $V_{n-j+1}^+(t)$ is $n - j + 1$. Hence, the cut is a one dimensional subspace described by normalized vectors $\{\mathbf{c}_j(t)\}_{j=1...n}$. These vectors are the CLVs.

Let us summarize some important properties of the CLVs and explain how we refer to them throughout this study. Since the CLVs are covariant, they cannot be orthogonal in general. Additionally, the covariance forces them to be norm independent. Note that the BLV and FLV are dependent on the chosen norm, because they are orthogonal. We also emphasize that there is a one-to-one relationship between the normalized vector $\mathbf{c}_j\,(t)$ (the CLV) and a time series of growth rates $\lambda_j(t)$ whose average is equal to the j^{th} LE with $\lambda_j = \lim_{T\to\infty}\frac{1}{T}\int_0^T dt\lambda_j(t)$. A solution $\mathbf{v}$ of equation 2.3 at time t with the initial condition $\mathbf{v}(t_0) = \mathbf{c}_j(t_0)$ has then the following form.

$$\mathbf{v}(t) = e^{\int_{t_0}^{t} dt'\lambda_j(t')}\,\mathbf{c}_j(t) \tag{2.10}$$

The normalized CLVs $\mathbf{c}_j(t)$ solve the following slightly altered equation.

$$\dot{\mathbf{c}}_j(t) = \mathcal{J}(\mathbf{x}_B(t))\mathbf{c}_j(t) - \lambda_j(t)\mathbf{c}_j(t) \tag{2.11}$$

Imagine now, we chose an arbitrary initial condition x_0 at time t_0, hence a superposition of possibly all CLVs

$$x_0 = \sum_j \mathbf{c}_j(t_0)A_j.$$

Consequently, the solution $\mathbf{x}$ for Equation (2.3) with $\mathbf{x}(0) = x_0$ has the following form in the basis of the CLVs.

$$\mathbf{x}(t) = \sum_j e^{\int_{t_0}^{t} dt'\lambda_j(t')}\,\mathbf{c}_j(t)A_j$$

This means the expansion of perturbations into the basis of CLVs allows it to investigate also very slow growing linear perturbations without interference of the fast growing directions (see Section 2.2). Following Szendro et al. (2008), we also expect that in the specific case where the system is prepared in such a way that a localized perturbation breaks otherwise symmetric boundary conditions, one can observe localization phenomena (not exclusively in the vicinity of the perturbation) for the CLVs of the system. This last property is extremely attractive for the problem of blocking events studied in Chapter five. These properties are unique to CLVs. Other Lyapunov vectors (e.g. Gram-Schmidt vectors; see (Kuptsov and Parlitz, 2012)) are not solutions of Equation (2.3) and are norm dependent which means they are confined by orthogonality. In contrast to those bases, CLVs describe - to first order - solutions of Equation (2.1) that are nearby to $\mathbf{x}_B$. Consequently, they have a straightforward physical interpretation. Moreover, energy conversions and feedbacks of the CLVs connected to the background can be obtained (shown in Sections 4.2 and 4.3). It is also possible to explain the variance of the background in a meaningful way similar to EOFs (see Section 4.4).

The CLVs relate to other bases in the tangent linear space. They are a generalization of the classical normal modes of stationary solutions. It is well known that if $\mathbf{x}_B$ is a stationary solution, the CLVs are identical to the eigenvectors of the time independent tangent linear operator $\mathcal{J}$ from Equation (2.3) (Wolfe and Samelson, 2007). For periodic background they coincide with the Floquet vectors (Floquet, 1883; Samelson, 2001a; Wolfe and Samelson, 2006, 2008).

After having clarified these basic definitions, let us explain in the upcoming section how CLVs are used in the context of dynamical system theory.

2.2 Application Of Covariant Lyapunov Vectors in Dynamical System Theory

We would like to give some examples for applications of CLVs outside of the field of geophysics and the scope of this thesis.

For many autonomous - time independent - dynamical systems, an attracting set exists which ”attracts” almost all points in the phase space. These sets are a well researched topic in the framework of Axiom A dynamical systems. The concept of an attracting set can be compared to the general observation of the spin up time in climate models after which the flow converges to a well defined ”climate’ if no time dependent forcing is imposed. For the precise mathematical details, we refer to Ruelle (1980) and Eckmann and Ruelle (1985). These attracting sets possess a stable and unstable manifold. Simply said, such manifolds are the sets of points in phase space that either converge exponentially fast to points on the attracting set (called the stable manifold) or have diverged exponentially fast in the past from points on the attracting set (called the unstable manifold). There is a noteworthy subtlety about the definition of the unstable manifold. A point belongs to the unstable manifold if it has diverged exponentially fast during the time frame $[-\infty, t]$. However, this does not imply that it will continue in this fashion. Thus, all points on the attracting set belong to the unstable manifold. For points on the attracting set the CLVs are locally tangent to the different directions of exponential growth or decay within these manifolds. Regarding research in geophysics, the question might be asked why it is relevant to investigate such structures beyond the scope of this thesis. It is well known that attractors have a fairly complicated structure. In certain directions, they are smooth manifolds, in other directions they exhibit a fractal and discontinuous structure. In fact, the smooth part of the attractor is equal to the unstable manifold. Therefore, knowing exactly which directions in the phase space span locally the unstable manifold is potentially very beneficial, especially in applications to data assimilation (Pazó et al., 2010; Palatella et al., 2013).

Furthermore, the CLVs can be used to determine the angle between the unstable and the stable manifold. A dynamical system is called hyperbolic if the angle between the stable and unstable manifold is non zero and has a minimum finite size. This is an important requirement for a special group of dynamical systems called Axiom A systems. For such systems many useful mathematical theorems are known. Unfortunately, almost all dynamical systems of physical interest are non-hyperbolic. Therefore, they can not be strictly considered Axiom A systems. Nevertheless, computing the degree of hyperbolicity of a system is interesting when considered in the context of the chaotic hypothesis. This hypothesis states that for macroscopic observables most dynamical systems behave in an ”Axiom A” like fashion (Gallavotti and Cohen, 1995). This might explain why some rigorous results in Axiom A systems can therefore be applied also in non-hyperbolic systems (e.g. in the context of linear response theory (Ruelle, 1998; Ragone et al., 2015)).

Furthermore, in terms of model reduction, the knowledge about the angles between the different directions of the unstable and stable manifold can be beneficial beyond such purely mathematically motivated goals. In Yang et al. (2009) and Takeuchi et al. (2011), the CLVs of several 1D and 2D dynamical systems were investigated. They found that for a sufficiently high resolution, the CLVs can be separated into two categories. First, there are the so-called physical modes which include unstable as well as parts of the least stable CLVs. These CLVs are frequently almost collinear. Second, there are the spurious modes. They are the remaining very stable CLVs. In contrast to the physical CLVs, spurious CLVs are more or less plane waves that are hyperbolically isolated from all other CLVs. They conjecture that the physical modes are a local approximation of the inertial manifold. This manifold is the ”smallest” smooth manifold in which the attracting set can be embedded. Proving the existence and finite dimension of the inertial manifold has potentially important applications for defining a ”sufficient” resolution of a model and for a systematic approach to model reduction (Foias et al., 1988; Dymnikov and Filatov, 1996).

In the last section of this chapter, we will complete the general discussion of CLVs by explaining the method developed by Ginelli et al. (2007) to obtain them.

2.3 How to Compute Covariant Lyapunov Vectors

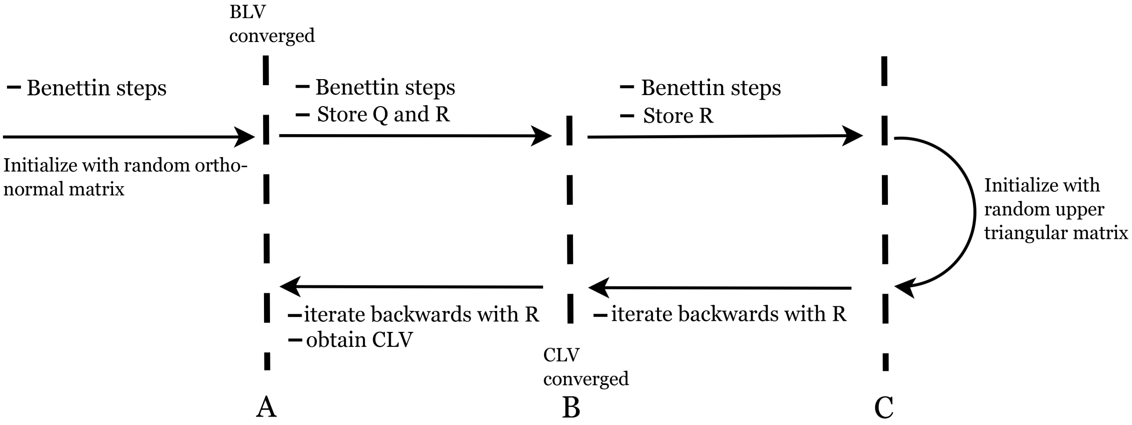
BLV
converged
– Benettin steps
Initialize with random ortho-normal matrix
– Benettin steps
– Store Q and R
– Benettin steps
– Store R
Initialize with random upper triangular matrix
–iterate backwards with R
–obtain CLV
– iterate backwards with R
CLV
converged
A
B
C

Figure 2.1: A schematic view of the algorithm proposed by Ginelli et al. (2007). The picture is inspired by Kuptsov and Parlitz (2012)

In order to compute the CLVs, we use the algorithm proposed by Ginelli et al. (2007). A detailed explanation is also found in Kuptsov and Parlitz (2012). Figure 2.1 gives a schematic view of the algorithm. A, B and C mark three points on a long integration of the dynamical system of interest that is statistically stationary. First, the algorithm computes the backward vectors and the corresponding backward subspaces (with the classical method of Benettin steps (Benettin et al., 1980)). After the convergence of the BLVs (see Equation (2.6)), the BLVs are obtained on the background trajectory between A and B. It is this time frame where the CLVs are later obtained. We then continue with Benettin steps until C. Here, at the end of this forward integration, we stop and start a backward iteration in the tangent linear model along the trajectory of the forward steps. Note that we choose a new set of initial vectors. This initial choice is random, but each vector lies in one of the backward spaces $\left\{V_j^-(C)\right\}_{j=1\cdots n}$. Additionally, the coordinate system of the tangent space is changed to the backward vector basis $B_j(t)$ for all t between A and C. In this basis, the propagator $\mathcal{F}$ as well as the chosen initial random vectors have a upper triangular shape. The propagator in this basis is called R and had been already obtained as a byproduct of the Benettin steps. The upper triangularity of R ensures algebraically that the vectors stay in their initial backward subspaces. This is necessary, since otherwise any vector would align with the fastest growing direction of the backward dynamics due to the finite computational accuracy. Moreover, also from a mathematical perspective, vectors of one backward subspace should always stay in the corresponding subspace (see equation 2.8). The backward iteration leads to a vector which aligns with the fastest growing vector of the backward dynamics in the respective backward subspaces. The time between B and C should be sufficiently large to ensure this. Note that the backward iterated vector is covariant to equation 2.3 and converges towards a vector, with a growth rate equal to the respective Lyapunov exponent (see equation 2.9) which depends on the initial backward subspace. Hence, during the backward iteration between B and A the desired CLVs are obtained. Note that this algorithm already encodes a fundamental difference to how normally a convergent algorithm is defined. In many applications there is a convergence for a limit going to infinity. Instead, the CLVs converge on the interval [A,B] and there is a convergent process coming from the before and after the interval. For example, in order to assess the convergence of the CLVs a cascade of nested intervals of [A,B] would be necessary.

This chapter has mainly dealt with the mathematical definition of CLVs and how they are obtained. Before, starting with the detailed numerical analysis of the CLVs, the next chapter will introduce in detail our QG model and the experimental setup.

Chapter 3

The Model and the Experimental Setup

This is the first time that CLVs are computed for a meteorological model, in order to study the properties of linear perturbations of its chaotic solutions. Of course, it is necessary to conduct such studies in more sophisticated models of the atmosphere, but as a first step, we have chosen a quasi-geostrophic two layer model which we will further explain in Section 3.1. In Sections 3.2.1 and 3.2.2, we explain the experimental setups used in Chapters 4 and 5.

3.1 Description of the Model

Our model is a spectral version of the classical model introduced by Phillips (1956). Such a model uses the quasi-geostrophic approximation which is obtained from the Navier-Stokes equation by conducting a scale analysis in respect to the temporal and spatial scales of the free atmosphere in the mid latitudes. This means a small Rossby number is assumed, $R = \frac{U}{Lf}$. U is the typical velocity scale, L the typical length scale and f the Coriolis parameter. This approximation means that the atmosphere is not in a simple geostrophic balance between pressure gradient and coriolis force. Instead, a small ageostrophic velocity is allowed, but assumed to be much smaller than the geostrophic velocity. Furthermore, the advection term is approximated with the geostrophic velocity which is an important difference to the semi-geostrophic equations (Chynoweth and Sewell, 1991) and allows for determining the state of the system with the geostrophic stream function alone. The other approximation concerns the coriolis parameter f which is linearly approximated at 45° N by the β parameter, $f(y) \approx f_0 + \beta y$. For more details, we refer to the textbook literature on this subject, e.g. Holton (2004). Our model contains further constraints. The domain is rectangular and only two vertical layers are resolved. We would like to stress that this model does not attempt to be realistic but instead

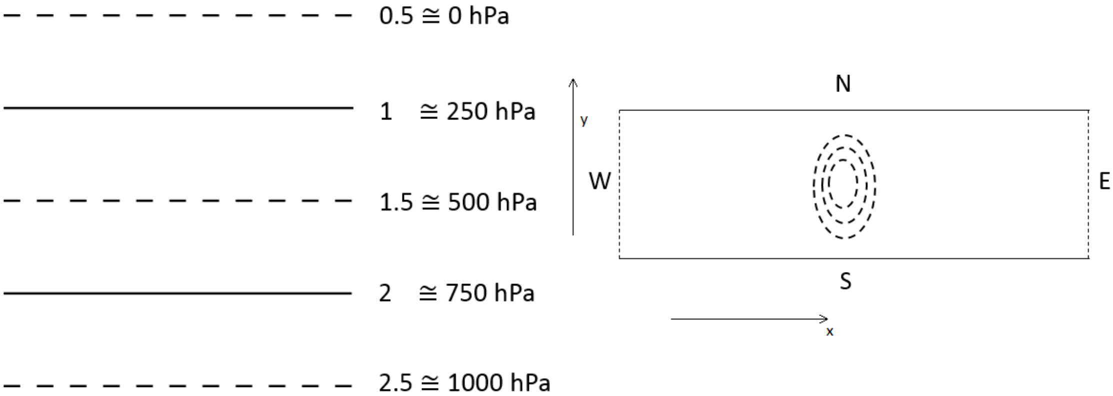

(a) Vertical Structure (b) Horizontal Domain

Figure 3.1: The domain of the QG model. The right panel shows in dashed lines a potential orographic forcing imposed on $\omega_{2.5}$

represent the very basic large scale behavior of the jet stream created by baroclinic and barotropic processes (Phillips, 1954, 1956).

Let us turn to the details of the model. As mentioned before, the horizontal domain is rectangular $(x, y) \in [0, L_x] \times [0, L_y]$. Also, it is periodic in the x-direction and a no flux condition is imposed at $y = 0, \pi$ (see Figure 3.1b). In the vertical, two layers are resolved (see Figure 3.1). We are solving the quasi-geostrophic vorticity equation at the two pressure levels $p_2 = 750hPa$ and $p_1 = 250hPa$ and the thermodynamic equation at $p_{1.5} = 500hPa$ (see Figure 3.1a).

In this setting, the hydrostatic equation also gives a simple expression for the temperature by employing the geostrophic stream function ψ.

$$T_{1.5} = \frac{f_0}{R}(\psi_1 - \psi_2) = \frac{2f_0}{R}\psi_T \tag{3.1}$$

The evolution equations are expressed in form of a partial differential equations (PDE) and are given by

$$\frac{\mathrm{d}}{\mathrm{dt}}\Delta\psi_1 = -\,\mathbf{V}_1 \cdot \nabla\left(\Delta\psi_1 + f_0 + \beta y\right) + f_0\frac{\omega_{1.5} - \omega_{0.5}}{\Delta p} + k_h\Delta^2\psi_1 \tag{3.2a}$$

$$\frac{\mathrm{d}}{\mathrm{dt}}\Delta\psi_2 = -\,\mathbf{V}_2 \cdot \nabla\left(\Delta\psi_2 + f_0 + \beta y\right) + f_0\frac{\omega_{2.5} - \omega_{1.5}}{\Delta p} + k_h\Delta^2\psi_2 \tag{3.2b}$$

$$\frac{\mathrm{d}}{\mathrm{dt}}\psi_T = -\,\frac{\mathbf{V}_1 + \mathbf{V}_2}{2} \cdot \nabla\psi_T + S_p\omega + \frac{J}{c_p} + \kappa\Delta\psi_T. \tag{3.2c}$$

Equations (3.2a) and (3.2b) describe the dynamics of the vorticity at the pressure levels 1 and 2 respectively and Equation (3.2c) describes the evolution of the temperature field (Holton, 2004). At the top-level ($p_{0.5}$) the vertical velocity ω is set to zero. The lowest sub layer accounts for Ekman pumping and orography h via the vertical p-velocity $\omega_{2.5} = \frac{\Delta p}{f_0}\, 2r\Delta\psi_2 - \frac{\Delta p}{H} J(\psi_2, h)$ (e.g. (Charney and Straus, 1980)). H is the height of the atmosphere ($7.3km$). Note that for this implementation of orography we have to ensure that h/H is small. We express the advection in terms of the Jacobian $J(A, B) = \frac{\partial A}{\partial x}\frac{\partial B}{\partial y} - \frac{\partial A}{\partial y}\frac{\partial B}{\partial x}$ using the geostrophic stream function ψ. The geostrophic velocity $\mathbf{V} = (u, v)$ is given by $(-\partial_y\psi, \partial_x\psi)$. The forcing to the models comes from diabatic heating J given by the newtonian cooling term $c_p r_R\,(\psi_e - \psi_T)$. ψ_e accounts for diabatic heating and cooling and provides the baroclinic input into the system. We consider $\psi_e = \frac{R\Delta T}{4f_0} cos(\frac{y\pi}{L_y})$ where ΔT is the equator-to-pole temperature difference the system is relaxed to by fast processes such as radiation and convection. As it is commonly known, if ΔT is low, the stationary solution is stable. Respectively, for higher values of ΔT baroclinic instability kicks in, so that when increasing ΔT, through various bifurcations, we reach a state of turbulent motion. Of course it is possible to conduct a sensitivity analysis on ΔT (e.g. (Lucarini et al., 2007)), but we will focus solely on three scenarios where the stationary solution is unstable and the steady state of the system is turbulent (see Figure 3.2 and table Table 3.1). The full equations of motion in terms of the baroclinic field $\psi_T = \frac{1}{2}\,(\psi_1 - \psi_2)$ and the barotropic field $\psi_M = \frac{1}{2}\,(\psi_1 + \psi_2)$ have then the following form:

$$\begin{aligned}\frac{\mathrm{d}}{\mathrm{dt}}\,\Delta\psi_M =& -J(\psi_M, \Delta\psi_M + \beta y) - J(\psi_T, \Delta\psi_T) - r\Delta(\psi_M - \psi_T)\\ &+ k_h\Delta^2\psi_M + \frac{1}{2}J(\psi_2, h)\end{aligned} \tag{3.3a}$$

$$\begin{aligned}\frac{\mathrm{d}}{\mathrm{dt}}\,\Delta\psi_T =& -J(\psi_T, \Delta\psi_M + \beta y) - J(\psi_M, \Delta\psi_T) + r\Delta(\psi_M - \psi_T)\\ &+ k_h\Delta^2\psi_T - \frac{1}{2}J(\psi_2, h) + \frac{f_0}{\Delta p}\omega\end{aligned} \tag{3.3b}$$

$$\frac{\mathrm{d}}{\mathrm{dt}}\,\psi_T = -J(\psi_M, \psi_T) + S\frac{f_0}{\Delta p}\omega + r_R\,(\psi_{Te} - \psi_T) + \kappa\Delta\psi_T. \tag{3.3c}$$

Note that $S = S_p\frac{R\Delta p}{2f_0^2}$. The choice of parameters will be based on Phillips (1956) and Lucarini et al. (2007). A list of all parameters and their values is given in Table 3.1.

Note that besides the already mentioned boundary conditions, a second boundary condition is necessary

$$\int_0^{L_x} dx \frac{\partial\psi}{\partial y}\bigg|_{y=0,L_y} = 0, \tag{3.4}$$

since a secondary PDE is solved (ageostrophic boundary condition) (Pedlosky, 1987). The adimensionalization is performed according to table 3.1. In the following, we will only use the adimensional model equations. The newtonian cooling

Variables, Operators & Constants	Symbol	Unit	Scaling Factor	Value of Scaling Factor
Stream Function	ψ	m^2/s	$L^2 f_0$	$10^{10}/\pi^2$
Temperature	T	K	$2f_0^2 L^2/R$	705.97
Velocity	$\mathbf{v}$	m/s	Lf_0	$10^3/\pi$
Laplace Operator	Δ	$1/m^2$	$1/L^2$	$\pi^2/10^{14}$
Jacobian	$J(\cdot,\cdot)$	$1/m^2$	$1/L^2$	$\pi^2/10^{14}$
Orography	h	m	H	$7.3\ km$

Parameters	Symbol	Dimensional Value	Unit	Scaling Factor	Adimensonal Value
Forced Meridional Temperature Gradient	ΔT	$40 - 76$	K	$2f_0^2 L^2/R$	$0.0567 - 0.1076$
Width of Mountain	σ_x, σ_y	1000, 2000	km	L	0.1π, 0.2π
Eddy-Heat Diffusivity	κ	10^5	m^2/s	$L^2 f_0$	$9.8696 \cdot 10^{-5}$
Eddy-Momentum Diffusivity	k_h	10^5	m^2/s	$L^2 f_0$	$9.8696 \cdot 10^{-5}$
Thermal Damping	r_R	$1.157 \cdot 10^{-6}$	$1/s$	f_0	0.011
Ekman Friction	r	$2.2016 \cdot 10^{-6}$	$1/s$	f_0	0.022
Stability Parameter	S	$3.33 \cdot 10^{11}$	m^2	L^2	0.0329
Coriolis Parameter	f_0	10^{-4}	$1/s$	f_0	1
Beta	β	$1.599 \cdot 10^{-11}$	$1/(ms)$	f_0/L	0.509
Aspect Ratio	a	0.6896	1	-	0.6896
Zonal Length	L_x	$2.9 \cdot 10^7$	m	L	$\frac{2\pi}{a}$
Meridional Length	L_y	10^7	m	L	π
Height Of Atmosphere	H	7.4	km		
Specific Gas Constant	R	287.06	$J/(kgK)$	$R/2$	2
Pressure	Δp	$500hPa$	N/m^2	Δp	1

Table 3.1: Parameters and Variables used in this model and the respective adimensionalization scheme. Note that the scales for time and length are $t = 10^4 s = 1/f_0$ and $L = \frac{10^7}{\pi} m$

stream function in the adimensional form is $\psi_{Te} = \frac{\Delta T}{2} cos(y)$.

$$
\begin{aligned}
\frac{\mathrm{d}}{\mathrm{dt}} \Delta\psi_M =& - J(\psi_M, \Delta\psi_M + \beta y) - J(\psi_T, \Delta\psi_T) - r\Delta(\psi_M - \psi_T) \\
& + k_h \Delta^2 \psi_M + \frac{1}{2} J(\psi_2, h) \\
\frac{\mathrm{d}}{\mathrm{dt}} \Delta\psi_T =& - J(\psi_T, \Delta\psi_M + \beta y) - J(\psi_M, \Delta\psi_T) + r\Delta(\psi_M - \psi_T) \\
& + k_h \Delta^2 \psi_T - \frac{1}{2} J(\psi_2, h) + \omega \\
\frac{\mathrm{d}}{\mathrm{dt}} \psi_T =& - J(\psi_M, \psi_T) + S\omega + r_R \left(\frac{1}{2} \Delta T cos(y) - \psi_T \right) + \kappa \Delta\psi_T .
\end{aligned}
\tag{3.5}
$$

With the boundary conditions and the adimensionalization, the stream function has the following form in spectral space.

$$
\begin{aligned}
\psi(x, y, t) =& \sum_{k,l=1}^{N_x, N_y} \left(\psi^r(k, l, t) \cos(akx) + \psi^i(k, l, t) \sin(akx) \right) \sin(ly) \\
& + \sum_{l=1}^{N_y} \psi^r(0, l, t) \cos(ly)
\end{aligned}
\tag{3.6}
$$

Where the spectral cutoff is in the zonal direction at N_x and in the meridional direction at N_y. The total dimension of the model phase space is $2N_y(2N_x + 1)$.

3.2 The Experimental Setup

For later reference in the Chapters 4 and 5, this section what the experimental setup of the model is in the respective chapters.

3.2.1 Experiments without Orography in Chapter Four

For the study in Chapter four, we will investigate the model without orography. This means $h = 0$. Furthermore, we choose $N_x = 10$ and $N_y = 12$ giving a total phase space dimension of 504. The meridional resolution is chosen to accurately approximate the Jacobian J in spectral space. Since its spectral representation requires a projection along the meridional direction we need a sufficiently high N_y. The zonal resolution is chosen to include at least all classically unstable normal modes for similar setups of two layer QG models (Holton, 2004). ΔT will be chosen in order to cover a weak, medium and chaotic behavior of the model ($39.81K$, $49.77K$ and $66.36K$). The integrations are performed in spectral space using a 4^{th} order Runge-Kutta-Scheme with a fixed time step of 1 (2.78 hours). In Chapter four all results are obtained using a 80000 (25 years) long time series.

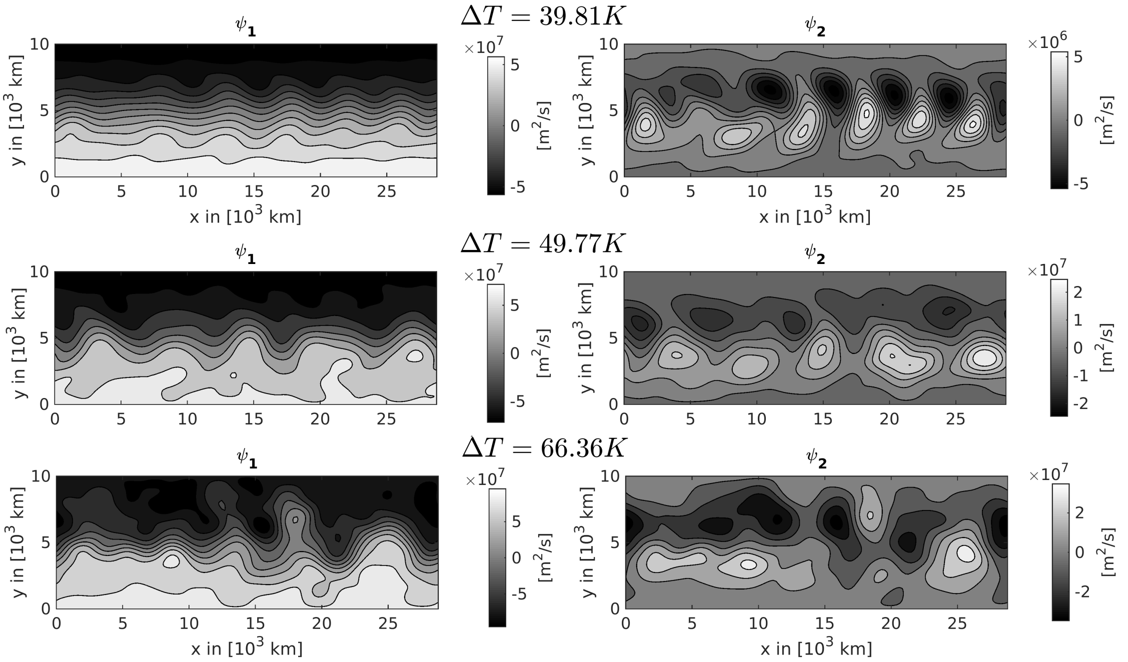

Figure 3.2: These snapshots show the stream function fields for the upper and lower layer. The upper is on the left side and the lower layer is found on the right side. Note that in order to use a grey scale, the scale of the colorbars is different in every panel. The flow shows a clearly baroclinically unstable and barotropically stable configuration (see Section 4.1)

The resolution in chosen studies regarding solutions of a closely related two layer QG models is significantly higher (Wolfe and Samelson, 2006, 2008). They obtained Floquet vectors, which are a special case of CLVs obtained if the background state is periodic. In our study, we are obtaining the CLVs for aperiodic background states over a much longer time period of ca. 25 years after a spin up time of ca. 30 years. Hence, due to our lower resolution we will not be able to study the turbulent cascade, but we will be able to study the behavior of the large scale baroclinic and barotropic processes. Clearly, it would be desirable to use higher resolution, but the fundamental aspects we want to emphasize in this study can already be captured with the current setting. This is also suggested by Figure 3.2, which shows the snapshots of the stream functions. The fields show baroclinically unstable eddies moving eastward which can be seen from the phase shift between the upper and lower layer. At the same they are barotropically stable, which can be seen from the angle of the stream function iso lines in regard to the zonal flow. We will discuss this classical large scale description of the mid latitude dynamics represented by an eddy field and a zonal mean in Section 4.1.

3.2.2 Experiments with Orography in Chapter Five

In Chapter five, we will study blocking events in the model which are enhanced by orography (see Section 5.2). The orography is an idealized Gaussian bump designed to resemble loosely the scales of the Rocky Mountains placed in the middle of the horizontal domain. Hence, we choose

$$h = h_0 e^{-\left(\frac{x-L_x}{\sigma_x}\right)^2 - \left(\frac{y-L_y}{\sigma_y}^2\right)},$$

with $\sigma_x = 1000\,km$ and $\sigma_y = 2000\,km$. We will use the same spectral cutoff as in the case without orography, hence $N_x = 10$ and $N_y = 12$. We perform a spin up run of 30 years. All results will be based on a time series of 31 years, except the control runs which have a length of 25 years. We investigate three different mountain heights h_0 (1.48 km, 2.96 km and 4.44 km) and four different meridional temperature gradients ΔT (40 K, 50 K, 66 K and 76 K). This ensures the investigation of different states of large scale turbulence and the assessment of the impact of orography. In control runs, the experiments are repeated without orography. The implemented 4^{th} order Runge-Kutta-Scheme uses a fixed time step of 1 (2.78 hours) except for the highest $\Delta T = 76K$. Here, we chose 0.25 (0.67 hours). The analysis of the data is then sampled every 2.77 hours.

Chapter 4

Instabilities and Feedbacks of Covariant Lyapunov Vectors[2]

After having introduced our model and the CLVs in the previous chapters, this chapter deals with the LEC of the CLVs and their ability to explain the variability of the flow. A brief summary of the most important aspects of the classical LEC describing the energy conversions between the eddy field and the zonal mean is presented in Section 4.1. In Section 4.2, we construct a LEC for each of the CLVs describing the energy conversions to the CLVs imposed by the background state and discuss its relation to the transports of heat and momentum. We have already described the experimental setup in Section 3.2.1. In Section 4.3, the main results of our experiments are discussed. We present the properties of the Lyapunov spectrum followed by the results for the LEC of the CLVs. Furthermore, we draw connections between the background state and the stable and unstable processes described by the CLVs. Finally, in Section 4.4, we report on the reconstruction of the variance of the background trajectories using CLVs, comparing the efficiency of using unstable versus stable modes. We conclude the chapter with a summary.

4.1 Atmospheric Circulation and the Lorenz Energy Cycle

We recapitulate here the essentials of the classical understanding of the mid-latitudes atmosphere and its turbulent features based on a separation of the trajectory into a zonal mean field ($[\psi] = \frac{1}{L_x}\int_0^{L_x} dx\,\psi$) and an eddy field ($\psi^E = \psi - \frac{1}{L_x}\int_0^{L_x} dx\,\psi$) (Saltzman and Vernekar, 1968) making reference to our model.

---

[2] **Schubert, S.**, & Lucarini, V. (2015). Covariant Lyapunov vectors of a quasi-geostrophic baroclinic model: analysis of instabilities and feedbacks. Quarterly Journal of the Royal Meteorological Society, doi:10.1002/qj.2588

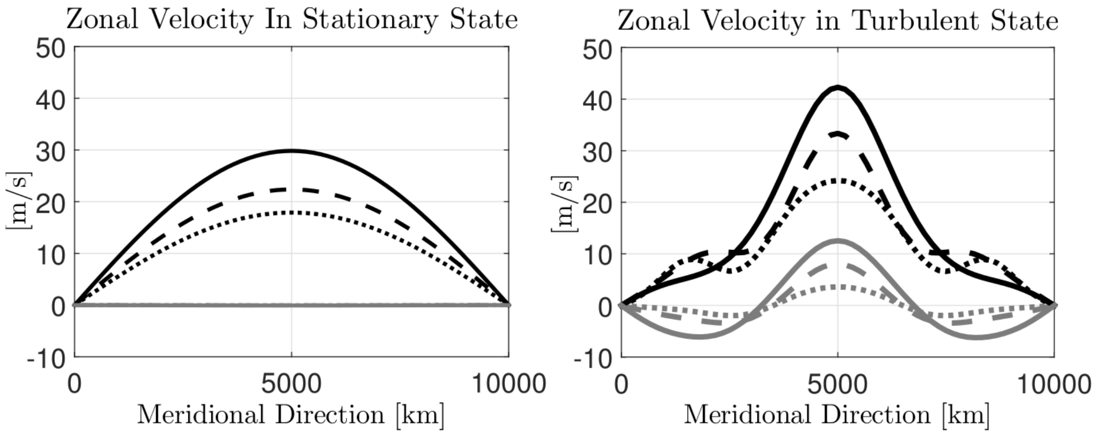

(a) Long term average of [U] in the stationary state for upper layer (black) and lower layer (gray).

(b) Long term average of [U] in the turbulent state for upper layer (black) and lower layer (gray).

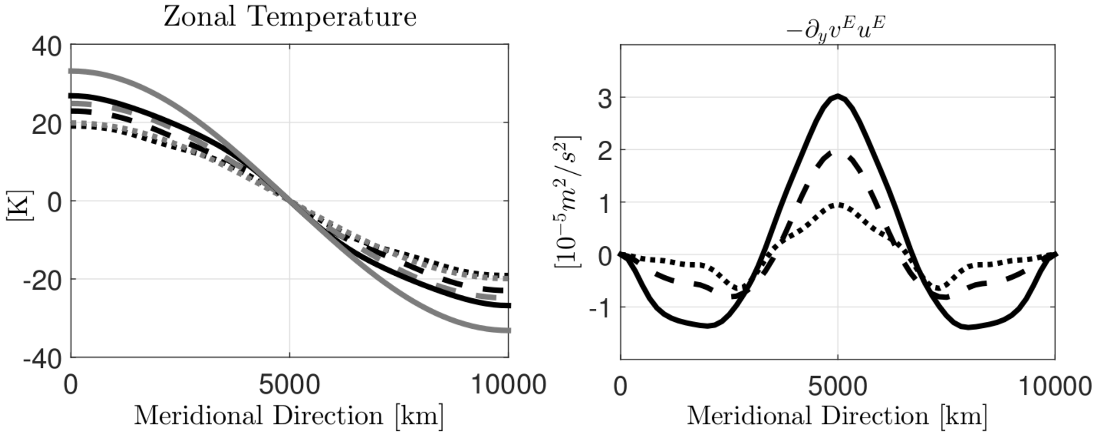

(c) Average temperature for stationary state (gray) and the turbulent state (black).

(d) Mean Convergence of Momentum Transport $-\partial_y u^E v^E$.

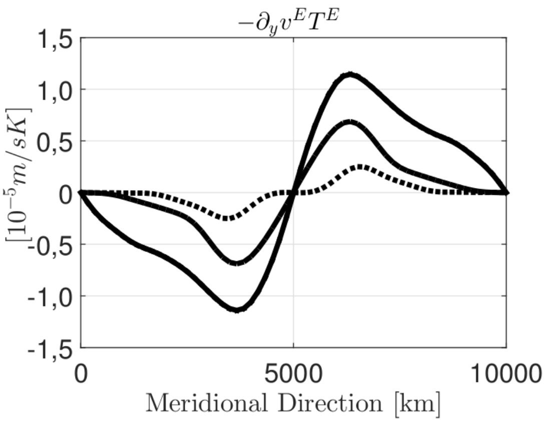

(e) Mean Convergence Of Northward Heat Transport $-\partial_y v^E T^E$

Figure 4.1: The mean state of the trajectory (averaged over a period of 25 years) for the three forced meridional temperature gradients ΔT (dotted: $39.81K$, dashed: $49.77K$, solid: $66.36K$). The superscript E indicates the eddy terms.

We refer to this approach as the eddy-mean decomposition (EMD). We study such a decomposition for three different values of the forced meridional temperature gradient ΔT (dotted: $39.81K$, dashed: $49.77K$, solid: $66.36K$). All setups feature an unstable stationary solution and an attractor corresponding to a turbulent solution.

The stationary state is unstable and therefore never observed in the turbulent flow. It is an idealized Hadley equilibrium (Held and Hou, 1980) which describes a balance of diffusion and newtonian cooling. Recalling the equations of motion (see equation 3.5), the stationary state is the following

$$\psi_M^S = \psi_T^S \cdot \left(\frac{1}{1 + \frac{k_h}{r}} \right) \tag{4.1a}$$

$$\psi_T^S = \frac{(r_R + \kappa)}{(r_R + \kappa) + S\frac{k_h}{r+k_h} + Sk_h} \psi_{Te}. \tag{4.1b}$$

Here, ΔT is almost equal to the observed temperature difference between the $y = \pi$ and $y = 0$ boundary, except for the $\frac{k_h}{r}$ correction term (see Figure 4.1 c). The upper layer features a broad baroclinic jet, the lower layer features a small easterly flow (see Figure 4.1 b). In the turbulent solution, eddies are transporting heat northward and momentum to the middle of the channel (see Figure 4.1 d, e). This feedbacks on the zonal mean state creating a sharper baroclinic jet with higher velocity gradients than in the stationary state (see Figure 4.1 a, b, d). In the lower layer, a small eastward jet emerges in the middle of the channel. North and south of the westerly jet, westward return flows are present in the lower layer balancing the long-term average momentum budget. The transports do not depend qualitatively on ΔT and are intensified with a higher ΔT.

We can further study the turbulence by decomposing the kinetic and potential energy into the zonal mean and eddy contributions. The conversions of energy between these energy reservoirs and the energy losses constitute the Lorenz energy cycle (LEC). Note that here we use the convention $\int d\sigma = 1/(L_x L_y) \int_0^{L_x} \int_0^{L_y} d(x,y) \ldots$.

$$\begin{aligned} E_{kin} &= \frac{1}{2} \int d\sigma \, (\nabla\psi_1)^2 + (\nabla\psi_2)^2 \\ &= \overbrace{\frac{1}{2} \int d\sigma \, ([\nabla\psi_1])^2 + \int d\sigma \, ([\nabla\psi_2])^2}^{[E_{kin}]} + \overbrace{\frac{1}{2} \int d\sigma \, (\nabla\psi_1^E)^2 + \int d\sigma \, (\nabla\psi_2^E)^2}^{E_{kin}^E} \end{aligned} \tag{4.2}$$

$$E_{pot} = \frac{1}{S} \int d\sigma \, \psi_T^2 = \underbrace{\frac{1}{S} \int d\sigma \, (\psi_T^E)^2}_{[E_{pot}]} + \underbrace{\frac{1}{S} \int d\sigma \, [\psi_T]^2}_{E_{pot}^E} \tag{4.3}$$

The LEC is obtained by decomposing the equations of motion into a system of coupled tendency equations for the zonal mean and the eddies (Phillips, 1956).

The resulting energy conversions and sinks can then be labeled in the following way. [3]

$$
\begin{aligned}
\frac{\mathrm{d}}{\mathrm{dt}} E^E_{kin} &= C_{ZK\to EK} + C_{EP\to EK} + S_{EEF} + S_{EKD} \\
\frac{\mathrm{d}}{\mathrm{dt}} E^E_{pot} &= C_{ZP\to EP} - C_{EP\to EK} + S_{ENC} + S_{EHD} \\
\frac{\mathrm{d}}{\mathrm{dt}} [E_{kin}] &= -C_{ZK\to EK} + C_{ZP\to ZK} + S_{ZEF} + S_{ZKD} \\
\frac{\mathrm{d}}{\mathrm{dt}} [E_{pot}] &= -C_{ZP\to EP} - C_{ZP\to ZK} + S_{ZNC} + S_{ZHD}
\end{aligned}
\tag{4.4}
$$

The conversions are the following.

Baroclinic Conversion $$\mathcal{C}_{ZP\to EP} = -\int d\sigma\, \frac{2}{S}[v^E_M \psi^E_T]\,[\partial_y \psi_T] \tag{4.5a}$$

Conversion Of Eddy Energy $$\mathcal{C}_{EPEK} = -\int d\sigma\, 2\omega^E \psi^E_T \tag{4.5b}$$

Conversion of Zonal Energy $$\mathcal{C}_{EK\to ZK} = -\int d\sigma\, 2\,[\omega]\,[\psi_T] \tag{4.5c}$$

Barotropic Conversion $$\mathcal{C}_{ZPEP} = -\int d\sigma \sum_{i=1}^{2} [\partial_y u_i]\left(v^E_i u^E_i\right) \tag{4.5d}$$

The long-term averages of these energy conversions are shown in Figure 4.2 and are intimately linked to the transports of heat and momentum of the eddies as we will describe in the following. The baroclinic conversion $\mathcal{C}_{ZP\to EP}$ quantifies the exchange between the potential energies of the mean and the eddy fields. In our model, the baroclinic conversion is positive, hence the eddies transport heat against the temperature gradient in the zonal mean state (see also figures 4.1 c,e). The barotropic conversion $\mathcal{C}_{ZK\to EK}$ quantifies the exchange between the kinetic energy of the mean and the eddy fields and is negative. This means the eddies transport momentum intensifying velocity gradients in the zonal mean state (see Figure 4.1 a,b). There are conversions from potential to kinetic energy for the zonal mean $\mathcal{C}_{ZP\to ZK}$ as well as for the eddy field $\mathcal{C}_{EP\to EK}$. $\mathcal{C}_{EP\to EK}$ is more relevant and is positive. Hence, on average warmer air ($\psi_T > 0$) rises or colder air ($\psi_T < 0$) sinks and thereby lowering the center of mass of the atmosphere. As a result kinetic energy is produced. There are also sinks of energy related to the various terms of friction, diffusion and newtonian cooling. Note that all of them are positive sinks of energy whereas the newtonian cooling of the zonal mean is the main input of

---

[3] Z stands for zonal, E for eddy. P is potential energy, K is kinetic energy. NC is newtonian cooling, EF is Ekman friction and KD and HD are kinetic and heat diffusion.

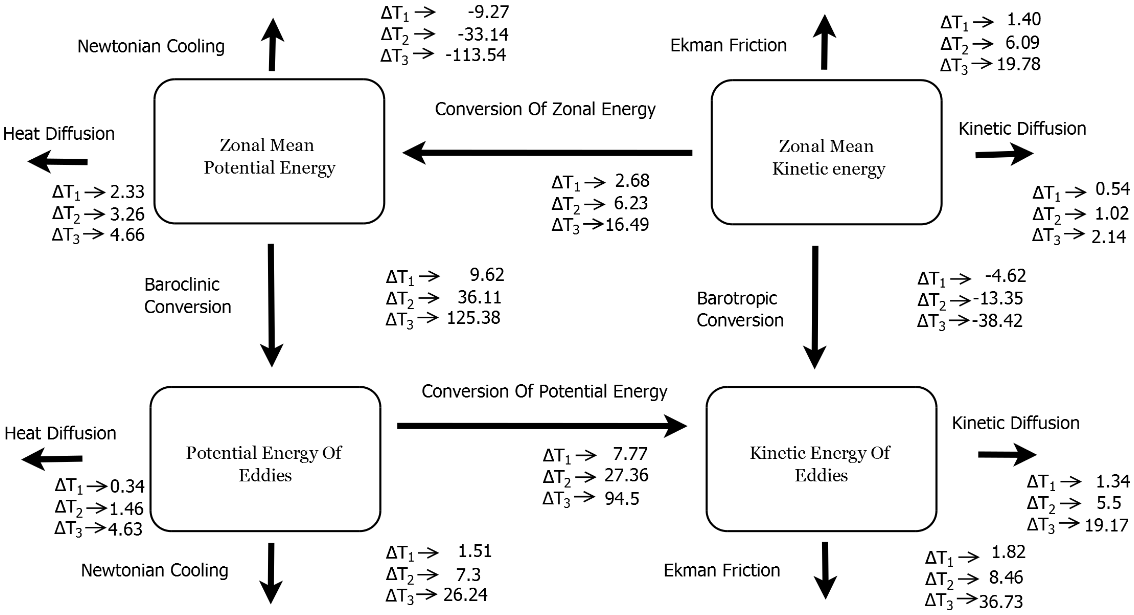
Newtonian Cooling
ΔT1-> -9.27
ΔT2-> -33.14
ΔT3-> -113.54
Ekman Friction
ΔT1-> 1.40
ΔT2-> 6.09
ΔT3-> 19.78
Heat Diffusion
Zonal Mean Potential Energy
Conversion Of Zonal Energy
Zonal Mean Kinetic energy
Kinetic Diffusion
ΔT1-> 2.33
ΔT2-> 3.26
ΔT3-> 4.66
ΔT1-> 2.68
ΔT2-> 6.23
ΔT3->16.49
ΔT1-> 0.54
ΔT2-> 1.02
ΔT3-> 2.14
Baroclinic Conversion
ΔT1-> 9.62
ΔT2-> 36.11
ΔT3-> 125.38
Barotropic Conversion
ΔT1-> -4.62
ΔT2->-13.35
ΔT3->-38.42
Conversion Of Potential Energy
Heat Diffusion
Potential Energy Of Eddies
ΔT1-> 7.77
ΔT2-> 27.36
ΔT3-> 94.5
Kinetic Energy Of Eddies
Kinetic Diffusion
ΔT1->0.34
ΔT2->1.46
ΔT3->4.63
ΔT1-> 1.34
ΔT2-> 5.5
ΔT3->19.17
Newtonian Cooling
ΔT1-> 1.51
ΔT2-> 7.3
ΔT3-> 26.24
Ekman Friction
ΔT1-> 1.82
ΔT2-> 8.46
ΔT3->36.73

Figure 4.2: Flow Chart of the Lorenz energy cycle for three ΔT (Units of Conversions are $10^5 m^2/s^3$). The arrows indicate the average sign of the energy conversions, sinks and sources of the zonal and eddy energies. For every temperature gradient ($\Delta T_1 = 39.81K$, $\Delta T_2 = 49.77K$ and $\Delta T_3 = 66.36K$) the dominant source of energy is Newtonian cooling, which inputs energy to the zonal mean potential energy. The important conversions are the baroclinic conversion which is related to the northward heat transport (see Figure 4.1 c) and the barotropic conversion related to the center pointed momentum transport (see Figure 4.1 d). The main energy losses occur by converting the potential energy of the eddies into kinetic energy, where it is lost mainly due to kinetic diffusion and Ekman friction. We observe an intensification of the cycle for a larger meridional temperature gradient ΔT.

energy to the LEC.

$$\begin{aligned}
&\text{Eddy Kinetic Diffusion} && \text{Eddy Ekman Friction} \\
&\mathcal{S}_{EKD} = -\int d\sigma k_h \sum_{i=1}^{2} \left(\Delta\psi_i^E\right)^2 && \mathcal{S}_{EEF} = \int d\sigma r \psi_2^E \Delta\psi_2^E \\
&\text{Eddy Heat Diffusion} && \text{Eddy Newtonian Cooling} \\
&\mathcal{S}_{EHD} = \int d\sigma 2\frac{\kappa}{S}\psi_T^E \Delta\psi_T^E && \mathcal{S}_{ENC} = -\int d\sigma 2\frac{r_R}{S}\left(\psi_T^E\right)^2 \\
&\text{Zonal Kinetic Diffusion} && \text{Zonal Ekman Friction} \\
&\mathcal{S}_{ZKD} = -\int d\sigma k_h \sum_{i=1}^{2} \left(\partial_y^2\left[\psi_i\right]\right)^2 && \mathcal{S}_{ZEF} = \int d\sigma r \left[\psi_2\right]\partial_y^2\left[\psi_2\right] \\
&\text{Zonal Heat Diffusion} && \text{Zonal Newtonian Cooling} \\
&\mathcal{S}_{ZHD} = \int d\sigma 2\frac{\kappa}{S}\left(\partial_y\left[\psi_T\right]\right)^2 && \mathcal{S}_{ZNC} = -\int d\sigma 2\frac{r_R}{S}\left[\psi_T\right]^2
\end{aligned} \tag{4.6}$$

Energy is mainly lost by kinetic diffusion and Ekman friction. The variation of the imposed meridional temperature gradient ΔT does not change the overall picture of the decomposition into eddy and zonal mean flows. Furthermore, also the heat and momentum transports and the LEC are not changing qualitatively. Overall, eddy energy is gained by baroclinic processes which tends to equilibrate the system, while barotropic processes create a "pointy" jet.

After this short review of the classical concept of the LEC, we continue in the next section by describing the growth and decay of the CLVs by a LEC between the background state and the CLVs.

4.2 The Lorenz Energy Cycle of Covariant Lyapunov Vectors

Classical stability analysis interprets the growth of the normal modes by introducing a Lorenz energy cycle between the normal modes and the zonal background state (see, e.g. Holton (2004)). This is based on the classical LEC described in the previous chapter. We apply this methodology for studying the energy exchange between the CLVs and the turbulent background flow.

In order to derive a meaningful definition of a LEC between the background trajectory and the CLVs, it is necessary to bring together the mathematical and the physical perspective on the evolution of the non-linear trajectory and the CLVs. The growth/decay and correlations in the phase space are measured with the help of norms and scalar products. We can connect growth and decay to physical processes when considering a suitable physical norm. In our model, this role is played by the total energy E_{tot}. We can decompose E_{tot} into a sum of kinetic energy E_{kin} and potential energy E_{pot}[4].

$$E_{tot} = \frac{1}{2}\sum_{i=1}^{2}\int d\sigma\ (\nabla\psi_i)^2 + \frac{1}{S}\int d\sigma\,\psi_T^2 \tag{4.7}$$

$$E_{kin} = \frac{1}{2}\sum_{i=1}^{2}\int d\sigma\ (\nabla\psi_i)^2 \tag{4.8}$$

$$E_{pot} = \frac{1}{S}\int d\sigma\,\psi_T^2 \tag{4.9}$$

Note that in our case, besides E_{tot}, the kinetic energy is a (squared) norm as well, whereas the potential energy is not a norm. Nevertheless, we will use the potential energy here like a norm and use it to define a "scalar product". This is then basically a "correlation like" bilinear form which gives the correlation between two states with respect to the potential energy. Thus, we can use these norms (meaning the square root of the energies) to define a bilinear scalar product $\langle A, B\rangle = \frac{1}{4}\left(||A+B||^2 - ||A-B||^2\right)$. The average growth rates of the CLVs measured in these or any other norms is equal to the Lyapunov exponents. This can be seen by a simple calculation. Let $||\cdot||$ be an arbitrary norm, $\mathbf{c}_j(t)$ the jth CLV and $\lambda_j(t)$ the corresponding time series of the local Lyapunov exponent (for more details see the solution along one CLV in Equation (2.10)). Then the average growth rate r is given in the following way.

---

[4] For the averages over the horizontal domain we define $\frac{a}{2\pi^2}\int_0^{2\pi/a} dx \int_0^{\pi} dy \cdots = \int d\sigma \ldots$.

$$\begin{aligned} r &= \lim_{T\to\infty}\frac{1}{T}\int_0^T dt \frac{\frac{\mathrm{d}}{\mathrm{dt}}||\mathbf{c}_j(t)e^{\int_0^t dt'\lambda_j(t')}||}{||\mathbf{c}_j(t)e^{\int_0^t dt'\lambda_j(t')}||} \\ &= \lim_{T\to\infty}\frac{1}{T}\int_0^T dt\ \frac{\mathrm{d}}{\mathrm{dt}}\log\left(||\mathbf{c}_j(t)e^{\int_0^t dt'\lambda_j(t')}||\right) \\ &= \lim_{T\to\infty}\frac{1}{T}\left\{\log\left(||\mathbf{c}_j(T)e^{\int_0^T dt'\lambda_j(t')}||\right) - \log\left(||\mathbf{c}_j(0)||\right)\right\} \end{aligned} \tag{4.10}$$

Since our model has a finite dimensional phase space, all norms are equivalent. Hence, for an arbitrary number of vectors with the same length in one norm possess a universal finite upper and lower bound for their length in any other norm (MacCluer, 2009). Therefore, the norm of $\mathbf{c}_j(t)$ is always smaller then a constant $K > 0$: $||\mathbf{c}_j|| < K$, because its euclidean norm is one. Therefore, the growth rate r can be explicitly calculated.

$$r = \lim_{T\to\infty}\frac{1}{T}\int_0^T dt\lambda_j(t). \tag{4.11}$$

Hence, the average growth rate of a CLV computed in an arbitrary norm equals always the respective Lyapunov exponent. Since $E_{tot} = E_{kin} + E_{pot}$, the same is valid for the average growth rate of potential energy "norm". In our calculations, we have verified that all three rates equal the doubled Lyapunov exponents given the numerical accuracy. This means that while a CLV is growing or decaying, the ratio of its potential versus kinetic energy is approximately (in a logarithmic sense) constant.

Let us now consider a linearized solution. Such a solution is the sum of a linear perturbation (ψ'_T, ψ'_M), a solution of Equation (2.3) composed by one CLV and the corresponding local growth time series $\lambda(t)$, and the chaotic background solution (ψ^B_M, ψ^B_T) (see Equation (2.10)). The energy of this superposition is the sum of the individual energies of the background state and the linear perturbation and an interference term.

$$\begin{aligned} E_{tot} =& E_{kin} + E_{pot} \\ E_{kin} =& \sum_i \int d\sigma\ (\nabla\psi^B_i)^2 + \sum_i 2\int d\sigma\ \nabla\psi^B_i\nabla\psi'_i + \sum_i\int d\sigma\ (\nabla\psi'_i)^2 \\ E_{pot} =& \frac{1}{S}\int d\sigma\ (\psi^B_T)^2 + \frac{2}{S}\int d\sigma\ \psi^B_T\psi'_T + \frac{1}{S}\int d\sigma\ (\psi'_T)^2 \end{aligned} \tag{4.12}$$

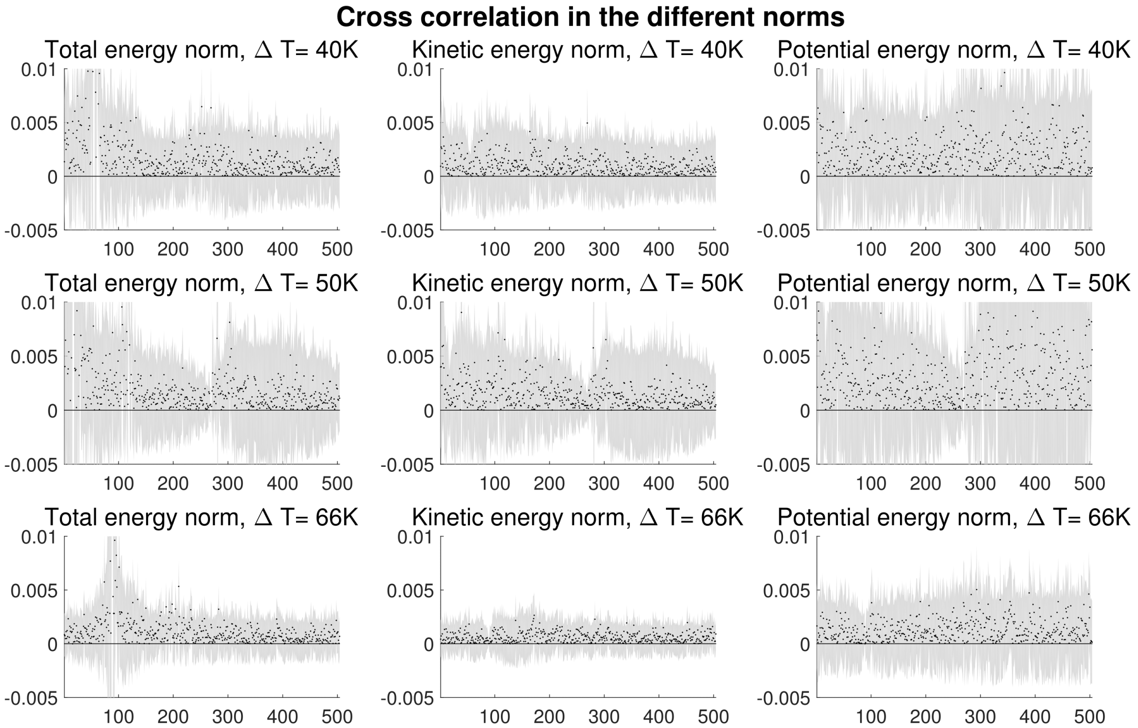

Figure 4.3: The graphs show the modulus of the average correlation $\frac{<\psi^B,\psi'>}{||\psi^B||||\psi'||}$ between the background state and the CLVs, where the bilinear product $< \cdot, \cdot >$ is defined via the kinetic, potential and total energy. The grey shaded areas are the 3 σ confidence intervals. We estimated the effective number of degrees of freedom by dividing the time series into blocks corresponding to the e folding time of the autocorrelation function (Leith, 1973). The x axis indexes the CLVs. Similar results have been obtained for non zonal stationary states (Niehaus, 1981)

We are interested in the long-term average behavior of these terms. A non vanishing long term averaged interference term means that the CLVs evolve "towards" the trajectory. Mathematically, this is equal to a non vanishing average correlation between the linear perturbation and the background state. This is not the case for any of the three defined energies (see the average correlations in Figure 4.3). By estimating the effective number degrees of freedom, we can show that with a significance level of 3 σ the correlations can be estimated to be zero. In fact, this is a necessary prerequisite, because a non vanishing correlation would imply that the background trajectory is not in a non-equilibrium steady state. This means the trajectory is in a steady state where no growth or decay occurs on average. Note that this is also fulfilled by the CLVs with zero LE. This is expected, because the zero growing CLVs are spanned by the tendency $\frac{\mathrm{d}}{\mathrm{dt}}\psi$ and the meridional velocity $\partial_x\psi$.

What leads linearized solutions to either converge to the background state, to stabilize or to grow infinitely? In order to answer this question, we have to consider the average derivative of energy (by applying $\frac{\mathrm{d}}{\mathrm{dt}}$ to Equation (4.12)). First, the energy of the background state does not grow or decay, therefore it cannot contribute to the linearized solution growing or decaying on the average. Second, even tough the interference term is linearly dependent on ψ', it is not contributing to the long term energy growth or decay either, since we showed that the correlation with the background state vanishes (see Figure 4.3). Thus, we are left with the time derivative of the third term of Equation (4.12) which only depends on the linear perturbation ψ'.

$$
\begin{aligned}
\frac{\mathrm{d}}{\mathrm{dt}} E'_{kin} &= -\int d\sigma \left(\psi'_1 \frac{\mathrm{d}}{\mathrm{dt}} \Delta\psi'_1 + \psi'_2 \frac{\mathrm{d}}{\mathrm{dt}} \Delta\psi'_2 \right) \\
\frac{\mathrm{d}}{\mathrm{dt}} E'_{pot} &= \frac{2}{S} \int d\sigma \left(\psi'_T \frac{\mathrm{d}}{\mathrm{dt}} \psi'_T \right)
\end{aligned}
\tag{4.13}
$$

From here on we can use the tangent linear equations. The physical interpretation of these terms is then inspired by the classical Lorenz energy cycle used for the EMD picture (see Section 4.1). The equations of motion of the tangent linear model are the following.

$$
\begin{aligned}
\frac{\mathrm{d}}{\mathrm{dt}} \Delta\psi'_M &= -J(\psi'_M, \Delta\psi^B_M + \beta y) - J(\psi^B_M, \Delta\psi'_M) - J(\psi'_T, \Delta\psi^B_T) \\
&\quad - J(\psi^B_T, \Delta\psi'_T) - r\Delta(\psi'_M - \psi'_T) + k_h \Delta^2 \psi'_M \\
\frac{\mathrm{d}}{\mathrm{dt}} \Delta\psi'_T &= -J(\psi^B_T, \Delta\psi'_M) - J(\psi'_T, \Delta\psi^B_M + \beta y) - J(\psi^B_M, \Delta\psi'_T) \\
&\quad - J(\psi'_M, \Delta\psi^B_T) + r\Delta(\psi'_M - \psi'_T) + k_h \Delta^2 \psi'_T + \omega' \\
\frac{\mathrm{d}}{\mathrm{dt}} \psi'_T &= -J(\psi'_M, \psi^B_T) - J(\psi^B_M, \psi'_T) + S\omega' - r_R \psi'_T + \kappa \Delta\psi'_T .
\end{aligned}
\tag{4.14}
$$

By using the boundary conditions of the model and some algebraic rearrangements we get the following.

$$
\begin{aligned}
\frac{\mathrm{d}}{\mathrm{dt}} E'_{kin} = \int d\sigma \, \big[&\Delta\psi'_1 \mathbf{v}'_1 \cdot \nabla\psi^B_1 - k_h \left(\psi'_1 \Delta^2 \psi'_1 \right) + \langle 1 \leftrightarrow 2 \rangle \\
&-2\psi'_T \omega' + 2r\psi'_2 \Delta\psi'_2 \big]
\end{aligned}
\tag{4.15}
$$

$$
\begin{aligned}
\frac{\mathrm{d}}{\mathrm{dt}} E'_{pot} = \int d\sigma \, \Big[&-\frac{2}{S} \psi'_T \mathbf{v}'_M \cdot \nabla\psi^B_T + 2\psi'_T \omega' + 2\frac{\kappa}{S} \psi'_T \Delta\psi'_T \\
&-2\frac{r_R}{S} \psi'^2_T \Big]
\end{aligned}
\tag{4.16}
$$

The interpretation of terms in Equation (4.15) to (4.16) is similar to what was reported in Section 4.1. In Section 4.1, we studied the exchange of energy between the zonal mean state and the eddies. Using the above equations, we study the energy conversion between a full non-linear background state and the CLVs.

The conversion from the background potential energy to the perturbation potential energy is the baroclinic conversion $\mathcal{C}_{BC}$.

$$
\mathcal{C}_{BC} = \int d\sigma \left[-\frac{2}{S} \psi'_T \mathbf{v}'_M \cdot \nabla\psi^B_T \right]
\tag{4.17}
$$

After applying integration by parts, this term equals the negative correlation between the convergence of heat transport of the CLV $(-\partial_y(v_M'\psi_T') - \partial_x(u_M'\psi_T'))$ and the temperature of the background state. Hence, a positive rate means a transport of heat against the temperature gradient in the background state. The conversion of potential into kinetic energy is described by $\mathcal{C}_{PK}$.

$$\mathcal{C}_{PK} = -2\int d\sigma\, \psi_T'\omega' \tag{4.18}$$

Barotropic processes are contained in the remaining conversion term. This term converts energy to the perturbation kinetic energy, the barotropic conversion $\mathcal{C}_{BT}$.

$$\mathcal{C}_{BT} = \int d\sigma \left[\Delta\psi_1'\mathbf{v}_1' \cdot \nabla\psi_1^B + \Delta\psi_2'\mathbf{v}' \cdot \nabla\psi_2^B\right] \tag{4.19}$$

We can rewrite this term to explicitly see the connection to the momentum transport of the CLVs and the horizontal divergences in the background flow.

$$\mathcal{C}_{BT} = \int d\sigma \left[-v_1'u_1'\frac{\partial v_1^B}{\partial x} - v_1'v_1'\frac{\partial v_1^B}{\partial y} - u_1'u_1'\frac{\partial u_1^B}{\partial x} - v_1'u_1'\frac{\partial u_1^B}{\partial y} + \langle 1 \leftrightarrow 2\rangle\right] \tag{4.20}$$

A positive rate means that the CLVs equilibrate the momentum distribution in the background state. Note that by defining a momentum transport matrix $\mathbb{M}$

$$\mathbb{M}_i = \begin{pmatrix} u_i'^2 & u_i'v_i' \\ u_i'v_i' & v_i'^2 \end{pmatrix} \tag{4.21}$$

We then get

$$\mathcal{C}_{BT} = \sum_i \int d\sigma \left(\mathbb{M}_i \begin{pmatrix} \partial_x \\ \partial_y \end{pmatrix}\right) \cdot \begin{pmatrix} u_i^B \\ v_i^B \end{pmatrix}. \tag{4.22}$$

The other terms are the sinks of the energy cycle due to eddy and heat diffusion, newtonian cooling and Ekman friction and each of them can be correspondingly related to their counterparts in the LEC of the eddies.

Eddy Diffusion $$D_E = \int d\sigma \left[-2k_h\left(\psi_T'\Delta^2\psi_T' + \psi_P'\Delta^2\psi_P'\right)\right] \tag{4.23}$$

Ekman Friction $$F_E = \int d\sigma\; r\psi_2'\Delta\psi_2' \tag{4.24}$$

Heat Diffusion $$D_H = \int d\sigma \left[2\frac{\kappa}{S}\psi_T'\Delta\psi_T'\right] \tag{4.25}$$

Newtonian Cooling $$NC = \int d\sigma \left[-2\frac{r_R}{S}\psi_T'^2\right] \tag{4.26}$$

Due to the fact that the CLVs are growing and decaying asymptotically, it is useful to consider rates instead of time derivatives. Therefore, we normalize all the terms of the LEC by the total energy of the CLVs (at every instant of time). In this way, we will obtain the exponential growth/decay rates of all quantities of the LEC. In

Table 4.1: Properties of the attractor

ΔT in [K]	Positive Exponents	Kaplan Yorke Dimension	Metric Entropy in [1/day]
39.81	17	35.83	0.25
49.77	55	125.82	3.15
66.36	88	206.80	12.51

general, the mean rate of an energy norm or energy conversion observable A will be the following.

$$\lim_{T\to\infty} 1/T \int dt \frac{\frac{\mathrm{d}}{\mathrm{dt}} A}{E_{tot}}$$

After having introduced, the basic ideas on the LEC and the CLVs, we continue in the next section by presenting the results for our experimental setup and show in detail the relationship between the various constituents of the LEC.

4.3 Physical Properties of Covariant Lyapunov Vectors

In this section, we present the actual features of the LEC and the associated transports for the CLVs. Additionally, we show the properties of chaoticity that can be derived from the Lyapunov spectrum.

4.3.1 The Lyapunov Spectra

The properties of the Lyapunov spectra are presented in this section. We further assume that the system at hand is "Axiom A"-like and a Sinai-Ruelle-Bowen measure exists in our model which describes its asymptotic statistical properties (Gallavotti and Cohen, 1995). All three cases correspond to settings of strong chaos with many positive Lyapunov exponents. This is also reflected in the Kaplan-Yorke dimension and the metric entropy production (see Figure 4.4 and Table 4.1). The Kaplan-Yorke dimension is defined as $D_{KY} = k + \frac{\sum_{i=1}^{k} \lambda_i}{|\lambda_{k+1}|}$, where k is chosen in such a way, that the sum of the first k Lyapunov Exponents is positive and the sum of the first $k+1$ is negative. This dimension is an upper bound of the fractal dimension of the attractor of the system. The metric entropy describes the information creation of the model and is given by the sum of the positive Lyapunov exponents (Eckmann and Ruelle, 1985). With increasing ΔT the Kaplan Yorke dimension and the metric

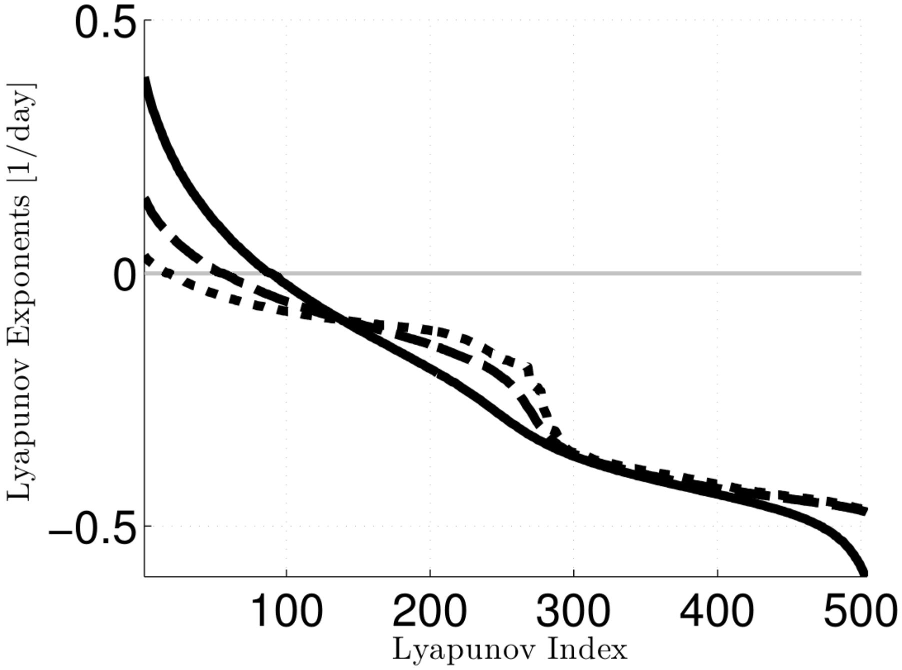

Figure 4.4: Lyapunov Exponents [1/day] for three meridional temperature gradients (dotted: $39.81K$, dashed: $49.77K$, solid: $66.36K$)

entropy grow monotonically as it was reported by Lucarini et al. (2007). While the observed motions are indeed chaotic for the three studied values of ΔT, we can clearly see from these dynamical indicators that turbulence is much better developed for higher values of ΔT.

4.3.2 Results for the Lorenz Energy Cycle of Covariant Lyapunov Vectors

Energy Conversion Terms and Sinks

Now we can unravel the connection of the physics of the CLVs captured by the LEC to their stability properties. The LEC of the CLVs is given by the long-term averages of the energy budget - normalized to the total energy of the CLV - between a single CLV and the background trajectory (see Section 4.2). With an abuse of language we will refer to a conversion as "unstable" if it is positive and "stable" if it is negative. The barotropic and baroclinic stability properties of the conversions of the LEC versus the value of the corresponding LE for all considered values of ΔT are shown in Figure 4.5. The baroclinic conversion is positive for roughly half of the CLVs independently of ΔT. This includes all growing CLVs and part of the decaying CLVs. The barotropic conversion on the other hand is only positive for some unstable CLVs in the case of intermediate/large ΔT. Instead for low ΔT the barotropic conversion is always negative. Hence, with increasing

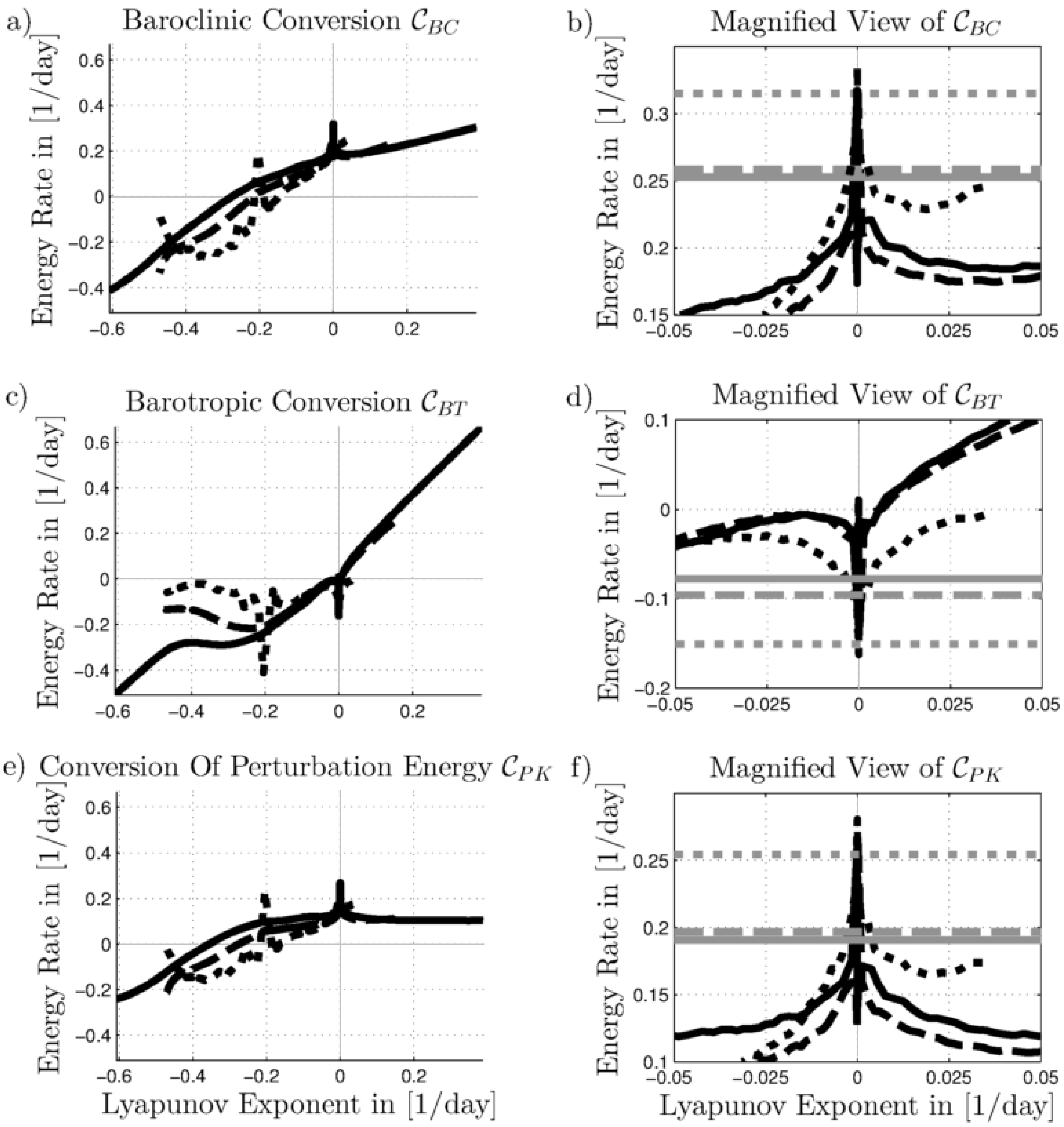

Figure 4.5: Left Side: The three figures show the dependence of the inputs and the conversion of the Lorenz energy cycle on the corresponding Lyapunov exponent for each of the three meridional temperature gradients (dotted: $39.81K$, dashed: $49.77K$, solid: $66.36K$). The magnified view (right side) shows the CLVs with near zero growth rate including the corresponding average eddy observables from the classical Lorenz energy cycle (gray horizontal lines). The y axis units are in 1/day.

ΔT, the barotropic conversion of all unstable CLVs turns from negative to positive values for the fast growing CLVs. Additionally, the conversion of the perturbation energy $\mathcal{C}_{PK}$ follows the sign of the baroclinic conversion $\mathcal{C}_{BC}$. We can also observe that being baroclinically unstable is not sufficient to let the CLVs grow because of the effects of friction and diffusion. This result should be considered in respect to findings in more complex models: Here, a high baroclinicity does not always lead to a baroclinic unstable energy growth of the eddies, because a certain threshold of baroclinicty has to be passed (Ambaum and Novak, 2014).

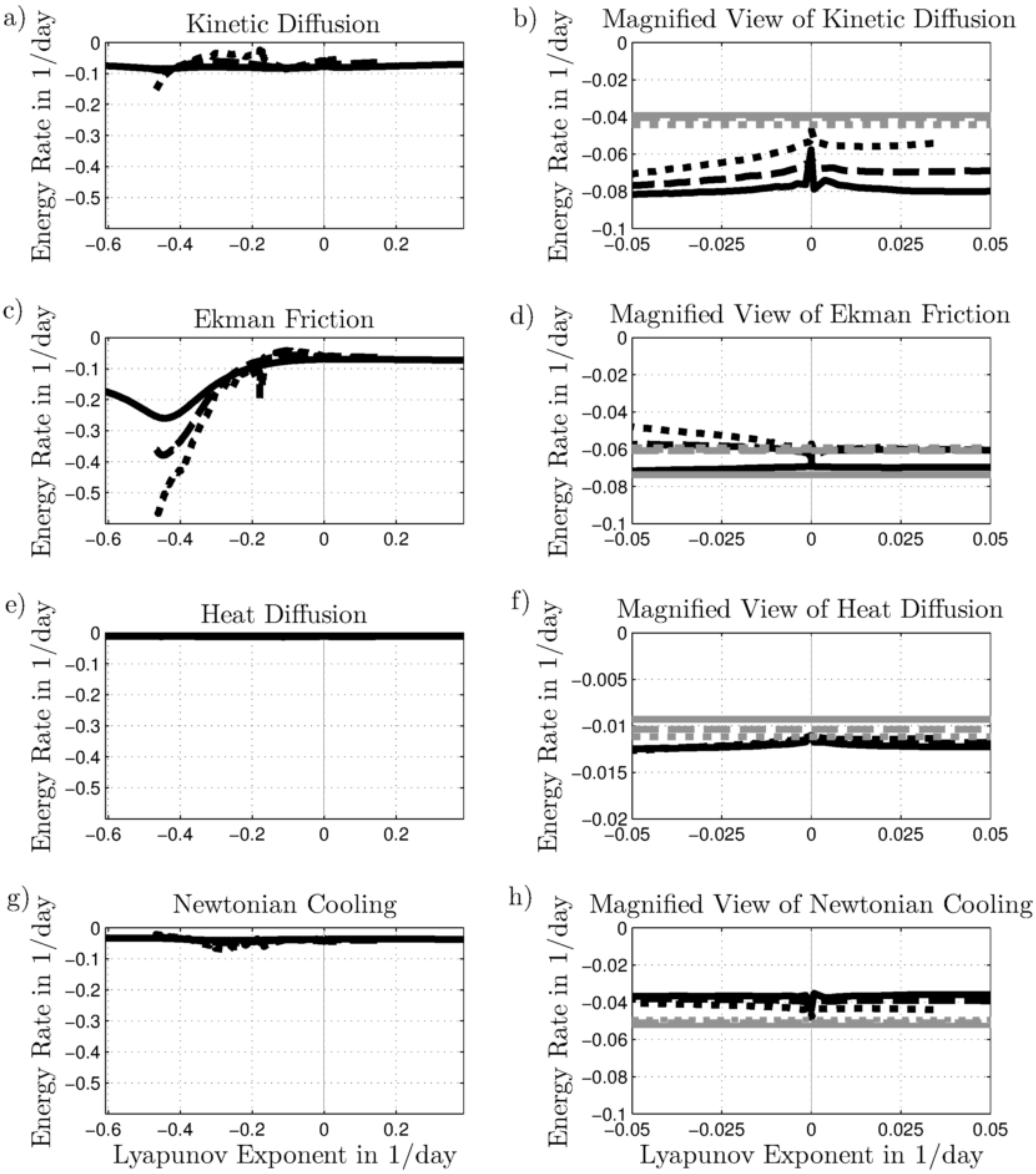

Figure 4.6: Left Side: The four figures show the dependence of the different sinks of the Lorenz energy cycle on the corresponding Lyapunov exponent for each of the three meridional temperature gradients (dotted: $39.81K$, dashed: $49.77K$, solid: $66.36K$). The magnified view (right side) shows the CLVs with near zero growth rate including the corresponding average eddy observables from the classical Lorenz energy cycle (gray horizontal lines). The y axis units are in 1/day.

Let us now look at the energy sinks of the LEC (see Figure 4.6). Newtonian cooling, kinetic and heat diffusion show little dependence on the CLVs and ΔT. The energy loss rate by Ekman friction is large for very stable CLVs (low Lyapunov exponents).

Since the Ekman friction (see Equation (4.24)) is proportional to the kinetic energy of the lower layer of the model, this corresponds to a localization of the flow in the lower layer. CLVs with the lowest LEs are stable through losses of kinetic energy through $\mathcal{C}_{PK}$ and Ekman Friction.

The slow growing CLVs are of particular interest (see Figure 4.5), because they are related to the hydrodynamic Lyapunov modes (HLM) discovered in other non-linear system (Yang and Radons, 2008; Posch and Hirschl, 2000). Note that CLVs are superior to orthogonal Lyapunov vectors for finding significant HLMs due to their norm independence (Romero-Bastida et al., 2012). Such CLVs are covariantly evolving solutions of the full non-linear equations which decorrelate very slowly with the background trajectory due to the slow growth rate. Therefore, it is expected that they might closely represent the properties of the large-scale dominating eddies resulting from removing the mean flow from the actual trajectory of the system. We compare the slow growing/decaying CLVs with the decomposition of the flow into zonal mean and the eddies (see Section 4.1) in the magnified view on the right side of the Figures 4.5 and 4.6. They show that the sign and magnitude of conversions from the classical Lorenz energy cycle are comparable to the LEC conversions of these CLVs. We also see a shift in the behavior of the fast growing CLVs which become barotropically unstable for higher ΔT and are less comparable to the LEC conversions of the EMD.

We note that the CLVs with corresponding LEs between -1.8 1/day and -3.8 1/day have properties which depend less regularly on the ordering number. This effect results from the fact that these CLVs are quasi-degenerate because of the small difference between the LEs of consecutive CLVs (Kuptsov and Parlitz, 2012).

Convergence of Heat and Momentum Transport and Vertical Velocity

The previously discussed energy conversion ($\mathcal{C}_{BC}$, $\mathcal{C}_{BT}$ and $\mathcal{C}_{PK}$) shown in Figure 4.5 are intimately related on the heat transport $\mathbf{v}'_M T'$, the momentum transport tensor $\mathbf{u}'\mathbf{v}'$ and the vertical heat transport $S\omega'$ of the CLVs (see Equations (4.18), (5.3) and (5.4), respectively). Table 4.2 shows systematically the connection between the eddy transports of the CLVs and the gradients of the background state. If the transports and corresponding gradients have a negative correlation, then a corresponding conversion is positive. If $\mathcal{C}_{BC}$ ($\mathcal{C}_{BT}$) is positive, $\mathbf{v}'_M T'$ ($\mathbf{u}'\mathbf{v}'$) transports heat (momentum) against the gradient of temperature (momentum) in the background state. If $\mathcal{C}_{PK}$ is positive, warmer air rises and colder air sinks (see Section 4.2). We report on the convergence of momentum transport $-\partial_y \sum_i u'_i v'_i$ (see Figure 4.7 a,c,e), the convergence of heat transport $-\partial_y v'_M T'$ (see Figure 4.7 b,d,f) and the vertical advection $S\omega'$ (see Figure 4.8 a-c). An integration by parts of Equations (5.3) and (5.4) shows that the convergence terms describe the spatial structure of the redistribution of momentum and heat (see Section 4.2). We restrict

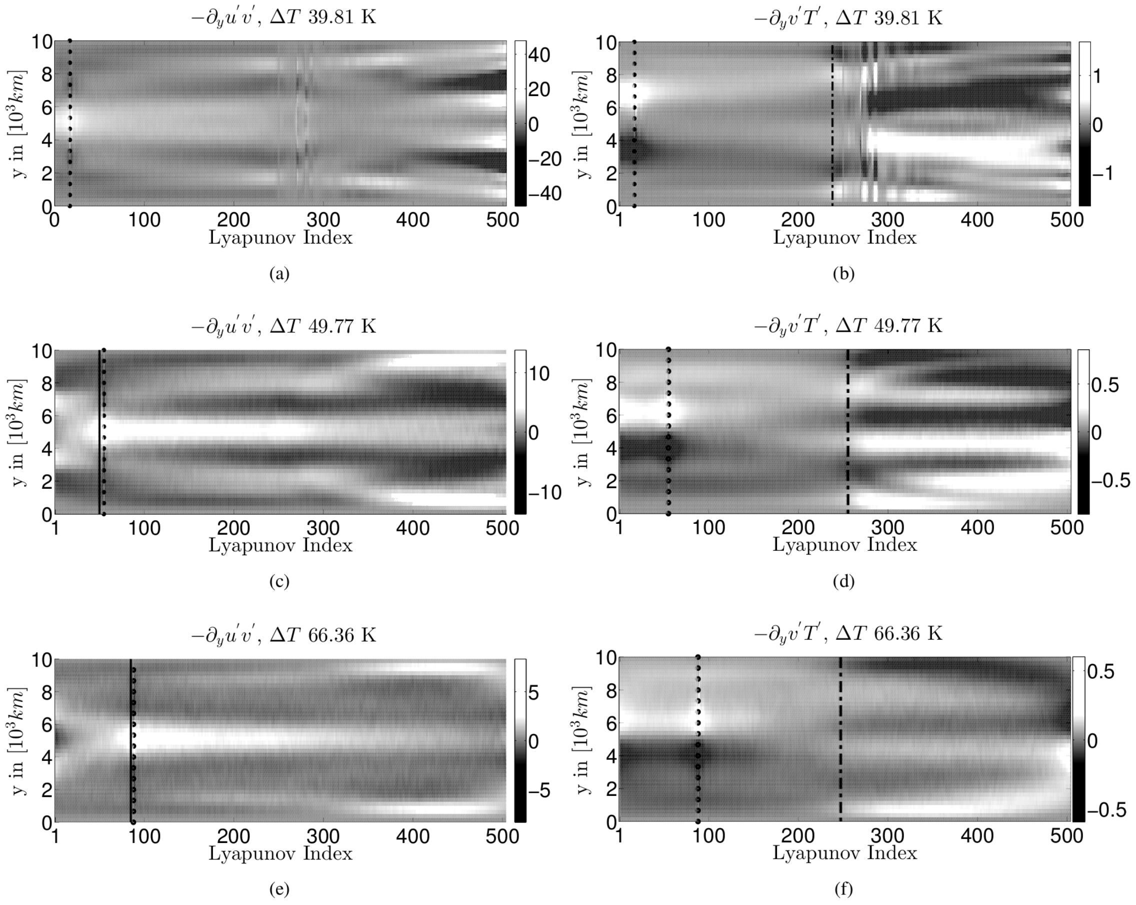

Figure 4.7: Left (a, c, e): The mean zonal profiles of Convergence of Momentum Transport. Right (b, d, f): Northward Heat Transport (b, d, f). The x axis indicates the jth CLV. In (a, c, e) the solid lines indicate the sign switch of the barotropic conversion $\mathcal{C}_{BT}$ from positive to negative. In (b, d, f) the dash-dotted lines indicate the sign switch of the baroclinic conversion $\mathcal{C}_{BC}$ from positive to negative. The black dotted lines show the CLV with smallest positive LE. The y axis shows the distribution in the meridional direction in $10^3 km$.

ourselves to zonally averaged quantities, because long-term averages converge to zonally symmetric fields which is due to the zonal symmetry of the model.

For CLVs with positive baroclinic conversion $\mathcal{C}_{BC}$, we have northward heat transport (see Figure 4.7 b,d,f), while a reversed transport is found for CLVs featuring a negative value of $\mathcal{C}_{BC}$. For lower values of ΔT, the convergence of heat transport is largest near the center of the channel. As ΔT increases, the area affected by the transport is extended in the north and south of the channel. The larger the baroclinic forcing, the more efficient are the CLVs with positive baroclinic conversion in transporting heat northwards, thus reducing substantially the meridional temperature gradient. Since heat is removed from the very low latitudes and deposited in the very high latitudes, one expects a flattening of the temperature profile. Note that the near zero CLVs are qualitatively similar, in terms of heat transports, to

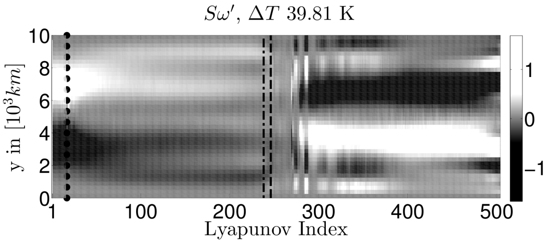

(a)

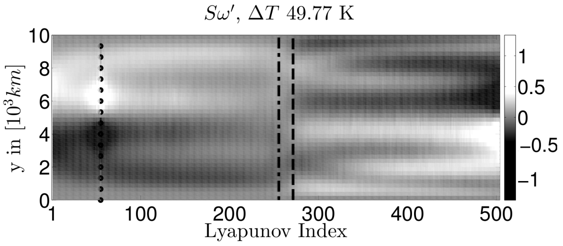

(b)

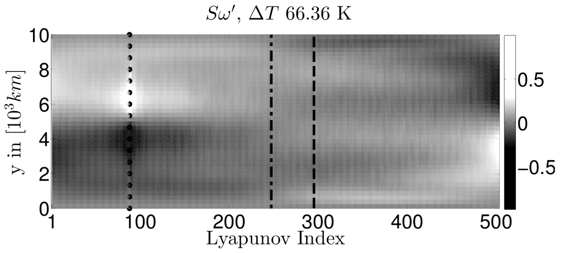

(c)

Figure 4.8: The mean zonal profiles of the conversion of heat $S\omega$ for the three meridional temperature gradients plotted for every CLV ((a) $\Delta T = 39.81$ K, (b) $\Delta T = 49.77$ K and (c) $\Delta T = 66.36$ K). The black vertical dash-dotted lines indicate the change of sign from positive to negative of the baroclinic conversion $\mathcal{C}_{BC}$. The dashed lines indicate the change of sign in the conversion from potential to kinetic energy $\mathcal{C}_{PK}$. The black dotted lines show the CLV with the smallest positive LE. The y-axis shows the distribution in the meridional direction in units of 103 km. The x-axis indicates the j^{th} CLV.

the most unstable CLVs (see position of the zero LE).

We recall that the barotropic conversion is related to the momentum transport. As discussed before, in the case of the lowest considered temperature gradient, no CLV features a positive barotropic conversion. Correspondingly, the momentum transports of the CLVs cause a convergence of momentum in the center of the channel, resulting a pointier jet (see Figure 4.7 a). Things get more complicated when larger values of ΔT are considered. In this case, the first CLVs are barotropically unstable, and, in fact, the implied momentum transport (see Figure 4.7 c,e) of these CLVs causes a depletion on the jet at the center of the channel. This is possible because the horizontal velocity gradients in the background state become sufficiently large (see Figure 4.1 b). For the more turbulent cases, the slow CLVs still feature momentum transport profiles which, instead, support momentum transport towards

Quantity	Conversions	Transport	Gradients
Zonal Potential to Eddy Potential Energy	$\mathcal{C}_{BC}$	$\mathbf{v}'_M T'$	$\nabla \Psi_T^B$
Zonal Kinetic to Eddy Kinetic Energy	$\mathcal{C}_{BT}$	$\mathbf{u}'.\mathbf{v}'$	$\nabla. \left(u_i^B, v_i^B\right)^T$
Eddy Potential to Eddy Kinetic Energy	$\mathcal{C}_{PK}$	$S\omega$	ψ_T^B

Table 4.2: Transports and Conversions - The conversion is positive if the correlation between gradient of the background state and eddy transport of the CLVs is negative. Note that for $\mathcal{C}_{PK}$ the baroclinic stream function ψ_T is proportional to the vertical gradient of the stream function.

the center of the channel. This results into the fact that we do observe a pointy jet as mean state of the system (see also Figure 4.1 a, b). Note that most decaying CLVs feature a positive convergence of momentum transport in the middle and on the flanks of the channel. This is connected to the smaller secondary jets on the flanks visible in the mean background state (see Figure 4.1 b).

In Figure 4.8 a-c, we explore the vertical heat transport $S\omega'$ caused by the CLVs. We immediately recognize the signature of baroclinic processes. The CLVs with positive baroclinic conversion feature upward and northward heat transport, while the opposite holds for the CLVs with negative baroclinic conversion rate. This corresponds exactly to the process of release (or creation, in the second case) of available potential energy.

After having presented the central results of the LEC for the CLVs, the next section will explore how the CLVs are able to explain variance of the background state in relation to their respective growth rates and the sign of the baroclinic conversion.

4.4 Explaining the Variability of the Background Flow

So far, we have studied the linear stability of our model by determining physical properties of CLVs (see Section 4.3). This is equivalent to the physical properties of nearby trajectories to the background trajectory. We can utilize these results to investigate the background state. Their divergent (convergent) evolution is directly linked to the variability of the background state, since the variability in a chaotic solution is caused by the divergence and convergence of nearby trajectories. It is expected that the diverging nearby trajectories dominate the variability over converging nearby trajectories. A classical example for this relation of linear stability

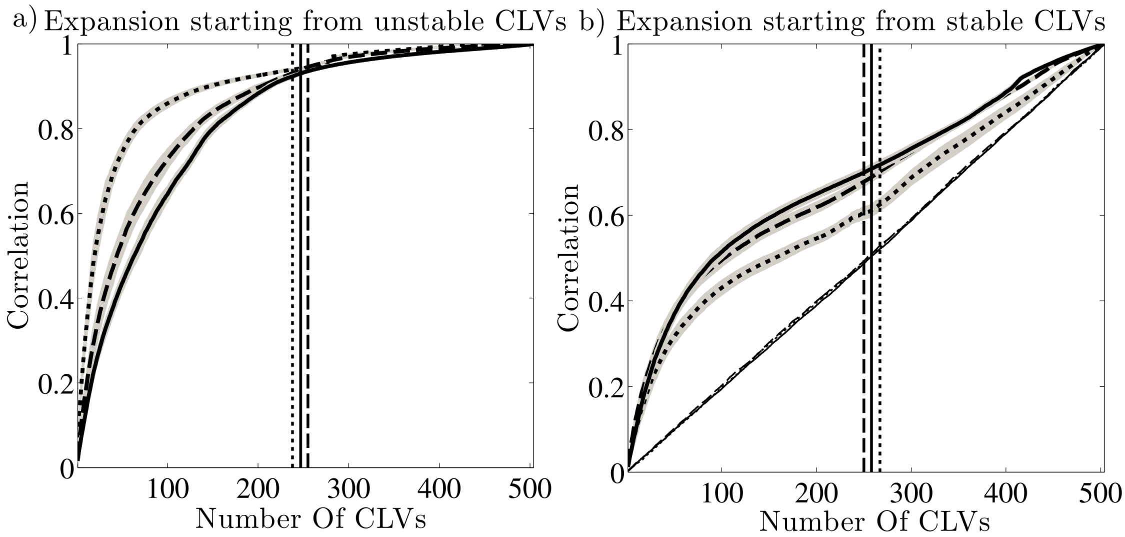

Figure 4.9: The panels show the average correlation (solid lines) of the subspaces spanned by the n fastest growing CLVs (a) and the n fastest decaying CLVs (b) with the considered trajectories of ΔT (dotted: $39.81K$, dashed: $49.77K$, solid: $66.36K$). The parameter n is indicated on the x axis. The average is done over the mean correlation for different reference points of the CLVs (41 reference points, equally distributed over a 12 years period). The corresponding σ area is indicated by the grey shaded regions. The vertical dashed dotted lines indicate where the expansion includes exactly all baroclinically unstable CLVs (a) or all baroclinically stable CLVs (b). (b) also shows the expansion into a randomly chosen basis (almost diagonal dashed lines). The comparison of both panels shows the higher explanatory power of CLVs with a higher LE.

and variance can be found interpreting the results of the Eady (1949) model. The linear instability analysis of the Eady model gives as a result modes and corresponding growth/decay rates. The most unstable modes explain qualitatively the variability of the mid latitudes atmosphere to a larger extent. Also, the length scales and growth rates of these modes are comparable to the typical scales of cyclones when reasonable parameters are inserted in the model. Moreover, the Eady modes grow (decay) similar to cyclones due to a vertical westward (eastward) tilt of the troughs and lows which induces a positive (negative) baroclinic energy transfer to the modes from the respective zonal background state and a northward (southward) eddy heat transport. Correspondingly, the CLVs gain (lose) energy by a northward (southward) heat transport $\int d\sigma\, v'T'$ and the positive (negative) baroclinic conversion $C_{BC} = -\frac{2}{S}\int d\sigma\, (\psi'_T \mathbf{v}'_M \cdot \nabla\psi^B_T)$. Note that our model features horizontal velocity divergences and therefore the stability of the CLVs is also dependent on the barotropic conversion (see Section 4.2). Having the Eady model in mind, we want to address two questions. First, what is the relation between the Lyapunov exponents and the explained variance of the respective CLVs? Second, how well do baroclinically unstable versus baroclinically stable CLVs explain the variance of the background trajectory? In contrast to other Lyapunov bases of chaotic trajectories the latter question can only be addressed with CLVs due to their covariance. Note that single CLVs are not correlated with the background trajectory (see Section 4.2), therefore we will consider subspaces spanned by multiple CLVs.

We address first how these subspaces of CLVs are constructed. If we consider the CLVs at a reference time t_R as a basis, we have to shift the center of our coordinate system to the corresponding point on the trajectory ($\mathbf{x}_R = (\psi_M(t_R), \psi_T(t_R))$). Note that the CLVs $\{\mathbf{c}_j(t_R)\}$ always form a basis, since they are linear independent by construction. For our purposes, we choose the following two cascades of sets spanned by CLVs. The first cascade

$$\mathcal{B}_n^{un}(t_R) = \text{span}\,\{c_j(t_R)|j = 1, \ldots, n\}$$

contains the CLVs with the n highest LE, the second cascade

$$\mathcal{B}_n^{s}(t_R) = \text{span}\,\{c_j(t_R)|j = d-n+1, \ldots, d\}$$

contains the CLVs with the n lowest LE (d is the total phase space dimension). The correlation with the subspaces is then defined in the following way. For each cascade $\mathcal{B}_n^{un/s}(t_R)$ the Gram Schmidt algorithm gives an orthogonal basis $\left\{{}^{un/s}\mathbf{O}_j^n(t_R)\right\}_{1\leq j\leq n}$ at the reference point $\mathbf{x}_R$. Hence, the projection of the normalized state vector at time t onto the subspace is

$$\mathbf{p}_n^{un/s}(t, t_R) = \sum_{j=1}^{n} {}^{un/s}\mathbf{O}_j^n(t_R) \left\langle {}^{un/s}\mathbf{O}_j^n(t_R), \frac{\mathbf{x}(t)}{||\mathbf{x}(t)||} \right\rangle. \tag{4.27}$$

The scalar product $\langle \ldots, \ldots \rangle$, is defined in the spectral representation of our model, where $\mathbf{x}$ is represented by $(\psi_M^r(k,l), \psi_M^i(k,l), \psi_T'^r(k,l), \psi_T'^i(k,l))$ and the scalar product of is defined in the following way.

$$\begin{aligned}
&\langle(\psi_M, \psi_T), (\psi_M', \psi_T')\rangle = \\
&\sum_{l=1}^{N_y} \Bigg\{ \left(\sum_{k=1}^{N_x} \psi_M^r(k,l)\psi_M'^r(k,l) + \psi_M^i(k,l)\psi_M'^i(k,l) + \psi_T^r(k,l)\psi_T'^r(k,l) + \psi_T^i(k,l)\psi_T'^i(k,l) \right) \\
&+\psi_M^r(0,l)\psi_M'^r(0,l) + \psi_M^i(0,l)\psi_M'^i(0,l) + \psi_T^r(0,l)\psi_T'^r(0,l) + \psi_T^i(0,l)\psi_T'^i(0,l) \Bigg\}
\end{aligned}$$

The correlation of $\mathbf{x}$ with a subspace $\mathcal{B}_n^{un/s}(t_R)$ at the chosen reference point is then

$$\lim_{T\to\infty} \frac{1}{T} \int_0^T \left\langle \frac{\mathbf{x}(t)}{||\mathbf{x}(t)||}, \mathbf{p}_n^{un/s}(t, t_R) \right\rangle. \tag{4.28}$$

The average correlation is one if the trajectory lies completely in the subspace defined by $\mathcal{B}_n^{un/s}(t_R)$. For the average, we sample the trajectory every 24 hours over a period of 25 years.

Figure 4.9 shows the average correlation as a function of n for the mean and standard deviation of $\mathcal{B}_n^{un/s}(t_R)$ obtained from a series of 41 equally distributed reference points over 12 years. In this figure we also compare the $\mathcal{B}_n^s$ cascade with a randomly chosen basis. For the same n the correlation of $\mathcal{B}_n^{un}$ is always higher than the correlation of $\mathcal{B}_n^s$. Hence, CLVs with higher LEs tend to explain the variance of the background trajectory better than CLVs with lower LEs. Nevertheless, the expansion into $\mathcal{B}_n^s$ is performing better than a random basis with the same size. This means the explanatory power of the CLVs is related to their stability as we expected it from the Eady model. For the second question, we can use the cascades for comparing the baroclinically stable versus the baroclinically unstable CLVs. The baroclinically unstable CLVs are one of the cascades $\mathcal{B}_n^{un}$, whereas the baroclinically stable CLVs are one of the cascades $\mathcal{B}_n^s$ (see vertical lines in Figure 4.9). The expansion into the baroclinically unstable CLVs correlates highly with the trajectory (≈ 0.94), whereas the expansion into the baroclinically stable CLVs has a lower correlation with the trajectory (≈ 0.66). The randomly chosen basis of the same size has a correlation of approximately 0.5 because its size is about half of the full phase space dimension (see Figure 4.9 b). Thus, the baroclinically unstable CLVs have a significantly higher correlation than the baroclinically stable CLVs. Baroclinic instability does not determine the overall stability of the CLVs, but baroclinically unstable CLVs dominate the explanation of the variance of the non linear flow. Moreover, while the Eady modes are rather idealized linear modes, the CLVs are a more general characterization of the flow since they are trajectories of nearby trajectories.

This allows to suggest a path for further studies of CLVs. The high quality of the reconstruction variance with the baroclinically unstable CLVs and the weak dependence on ΔT suggests that this might be a robust way to construct a reduced order model. Traditionally, empirical orthogonal functions of the trajectory are used to construct such a model of the underlying dynamical system (Holton, 2004; Franzke et al., 2005). The main limitation of these methods is that they rely solely on correlations of the trajectory and are not connected to the equations of motion or to the tangent linear dynamics which are intimately related to the stable and unstable processes. Due to their explanatory power and their covariance CLVs could provide a useful tool for further studies in this direction.

4.5 Summary and Discussion

Our objective in this chapter was to determine the physical properties of the tangent linear space of a quasi-geostrophic model of the mid latitudes atmosphere. Aiming at this, we made use of new tools (Covariant Lyapunov Vectors) which allow for obtaining a covariant basis of this space and allow for investigating linear stability far away from the stationary state of the flow. Traditional linear stability analysis of the atmosphere investigates normal modes which define the linear stability of typically stationary or zonally symmetric states. This understanding of the dynamics is linked to the decomposition of the atmospheric flow into a zonal mean state and an eddy field. For our stability analysis of a turbulent background flow, we studied the evolution of non-linear flows close to a turbulent non-linear background. This was described by a superposition of the background and linear perturbations. The instabilities and stabilizations of these linear perturbations along the background cannot be reduced to the tangent linear dynamics of a mean profile. We then studied the physical mechanisms responsible for growth and decay of the small perturbations, by focusing on their energy exchange with the background trajectory using an analysis similar to the traditional Lorenz energy cycle. Furthermore, we investigated baroclinic and barotropic conversion processes and then study the feedbacks.

The CLVs provide the appropriate mathematical tool to conduct such an analysis. They span the tangent space in the asymptotic time limit, and they are covariant with the tangent linear dynamics so that they represent actual perturbations to the background trajectory (Ruelle, 1979). This allowed to examine the link between the stability of the CLVs and their energetic properties given by the energy exchange between the background state and the CLV. We obtained the CLVs with the algorithm proposed by Ginelli et al (Ginelli et al., 2007).

As a first step towards more sophisticated geophysical models we used a QG two layer model in a periodic channel of the Phillips type (see Section 3.1). It features the basic baroclinic and barotropic processes of the mid-latitudes and is computationally feasible. Three experiments were conducted with a varying forced meridional temperature gradient ΔT ($39.81K$, $49.77K$, $66.36K$). These three turbulent regimes feature an increasing Kaplan-Yorke-Dimension and an increasing number of positive LE, thus chaoticity is enhanced. These properties of the LE are consistent with previous findings in a QG model (Lucarini et al., 2007). All setups feature a baroclinic jet in the upper layer which becomes pointier while increasing ΔT. We can further characterize the chaotic and turbulent behavior by a decomposition of the flow into a zonal mean and an eddy field. The Lorenz energy cycle of this system features a positive baroclinic conversion accompanied by a northward heat transport and a negative barotropic conversion accompanied by a transport of momentum to middle of the channel. Hence, the turbulent flow reduces the temperature gradients, but intensifies the velocity gradients in the mean state via the meridional transports of the eddies. These processes intensify with increasing ΔT.

The CLVs have a one-to-one relationship to the Lyapunov exponents which are the average growth rates of the CLVs in the euclidean norm. Given that the average growth rates of the CLVs are the same in any norm, a link is provided between physical properties and mathematical properties. Consequently, an energy cycle can be defined between the CLVs and the background flow similar to the classical LEC of the decomposition into eddy field and zonal mean. This allows for connecting baroclinic and barotropic processes and the closely connected heat and momentum transports of the CLVs to their stability properties. Roughly half of the CLVs have a positive baroclinic conversion and a northward heat transport against the average temperature gradient of the background state. As for the barotropic conversion, only fast growing CLVs in the two cases with a higher ΔT have a positive rate. Hence, they equilibrate the momentum gradients in the background state, if the jet of the background state has a sufficiently high meridional velocity gradient. All unstable CLVs have a positive baroclinic conversion, yet this is not sufficient for a growing CLV, since friction caused by Ekman pumping and kinetic diffusion counteract this input of energy. The barotropic conversion depends largely on ΔT. Unstable CLVs have a positive barotropic conversion, if the background state features a baroclinic jet with sufficiently large velocity gradients.

In Section 4.3, we systematically compared the conversions, sinks and transports of the LEC of the CLVs with the classical LEC obtained by decomposition of the background trajectory into eddy and a zonal mean field. The slowly growing and decaying CLVs exhibit similar properties as they all feature terms of a positive baroclinic conversion and a negative barotropic conversion including the associated momentum transport to the middle of the channel and the northward heat transport. This is due to the slow decorrelation of the slow growing/decaying CLVs with the background trajectory. In the case of low forcing (low ΔT), we saw a correspondence between the classical linear stability analysis (Pedlosky, 1964) and our generalized stability analysis with CLVs. In this case even the fastest growing CLVs are slow growing and the mean state is close to the stationary state. Therefore, the most unstable directions exhibit properties similar to the normal modes.

In Section 4.4, we tried to "close the cycle" and use the CLVs to construct a reduced basis for describing the dynamics of the system, taking into consideration that they describe the unstable and stable modes of variability. This approach differs from EOF-based approaches because the latter use basis that are only loosely related to the dynamics. Instead, the CLVs are covariant and therefore linked to the dynamics of the turbulent motion. CLVs with positive baroclinic conversion deliver a significantly better explanation of the variance (≈ 0.94) then the CLVs with a negative baroclinic conversion (≈ 0.65). This is a robust qualitative and quantitative result regardless of the value of ΔT. Moreover, CLVs with a higher growth rate explain on average the variance of the background trajectory better than a CLVs with a lower growth rate. This agrees with the general notion that in the end the divergence of nearby trajectories creates the variability found in chaotic models. This reflects e.g. the classical interpretation of the Eady model, where the most unstable linear modes are considered representative of the actual observed variability of the fields.

Chapter 5

Looking at Blocking Events Using the Formalism of Covariant Lyapunov Vectors[5]

After having analysed the energetics of the CLVs and their ability to represent in the variability in detail in the last chapter. We continue employing the same model extended by orography (see Section 3.2.2) to investigate blocking events. This means instead of only focusing on the long-term average properties of the flow we investigate the fluctuations of the background state and in consequence also the fluctuations of the CLVs and the respective LE. We structure the chapter in the following way. The blocking detection method is described in Section 5.1. In Section 5.2, we discuss the resulting blocked and unblocked regimes. In Sections 5.3.1 to 5.3.3, we present the results of our investigation of the linear stability and the localization of the CLVs. Finally, we will summarize the findings and point the reader towards future work on this topic (in Section 5.4).

5.1 Blocking Detection

We describe briefly the adapted Tibaldi-Molteni scheme (Tibaldi and Molteni, 1990) for detecting blocking highs in our model. Since the model is spectral, we are using a fft-algorithm to transform the spectral fields to a [64 × 32] grid (64 grid points in the x direction, 32 grid points in the y direction). Note that in the y-direction we use the fft by doubling the domain in the y-direction by using the prescribed basis functions in this direction (see Equation (3.6)). We consider a particular coordinate x blocked if the blocking lasts at least two days. We will consider only blocking in the barotropic stream function ψ_P, since it is the best representation of the 500 hPa layer in our model discretization. In order to detect blocking high anomalies, we study the occurrence at some longitude of reversals in the direction of the zonal wind with respect to normal conditions. We construct the average zonal wind in the northern and southern sector by constructing the quantities $u_N(x, \Delta) = -\delta\psi_N(x, \Delta)/(y_N - y_0)$ and $u_S(x, \Delta) = -\delta\psi_S(x, \Delta)/(y_0 - y_S)$, where $\delta\psi_N(x, \Delta) = \psi_P(x, y_N + \Delta) - \psi_P(x, y_0 + \Delta)$ and $\delta\psi_S(x, \Delta) = \psi_P(x, y_0 + \Delta) - \psi_P(x, y_S + \Delta)$.

---

[5] **Schubert, S.**, & Lucarini, V. (2015): Dynamical Analysis of Blocking Events: Spatial and Temporal Fluctuations of Covariant Lyapunov Vectors, submitted.

A blocking event is said to occur if at a particular coordinate x u_S is negative and u_N is sufficiently positive. We also allow for a deviation Δ from the chosen y-coordinates. Summarizing this we have the following criteria.

$$\begin{aligned} &u_N(x, y_0 + \Delta) > 9\,m/s \\ &u_S(x, y_0 + \Delta) < 0\,m/s \\ &y_N = 8437\,km;\ y_0 = 6250\,km;\ y_S = 4375\,km \\ &\Delta = (-940\,km\ 0\,km\ 940\,km) \end{aligned} \tag{5.1}$$

A word of caution is needed at this point since the Tibaldi-Molteni index was originally developed for a spherical geometry and considered either observational data or more realistic data taken from GCMs. However, we still think the use of this index is meaningful because of its straightforward interpretation and because it describes the presence of an non-zonal deviation from the usually fluctuating, but zonally symmetric jet stream. We will show that the detected blocking events are indeed meaningful, hence a blocked and an unblocked weather regime can be determined (see the following discussion in Section 5.2).

5.2 Blocking Events

Let us first look at the blocking rate. Comparing the different setups with the control runs (without orography), we can also assess the impact of the orography on the blocking. For reasons of symmetry, in absence of orography, the statistics of blocking does not depend on x.

The blocking rate (see Figure 5.1) kicks off when ΔT is larger than 50 K (even without orography). The orographic forcing creates two to three local maxima in the blocking rate downstream of the peak of orography. These maxima intensify for higher h_0 and for higher ΔT, but in the range of values considered here the impact of h_0 seems to be higher.

As mentioned before, two main configurations of the flow are identified. This can be further substantiated by considering the mean states of the unblocked and blocked flow (e.g. $\Delta T = 66K$ and $h_0 = 4.44km$ in Figure 5.2). In this way, we treat the unblocked and blocked phases as separate weather regimes and determine the "climate" of the two, respectively. Note that we divide the blocked regime again into

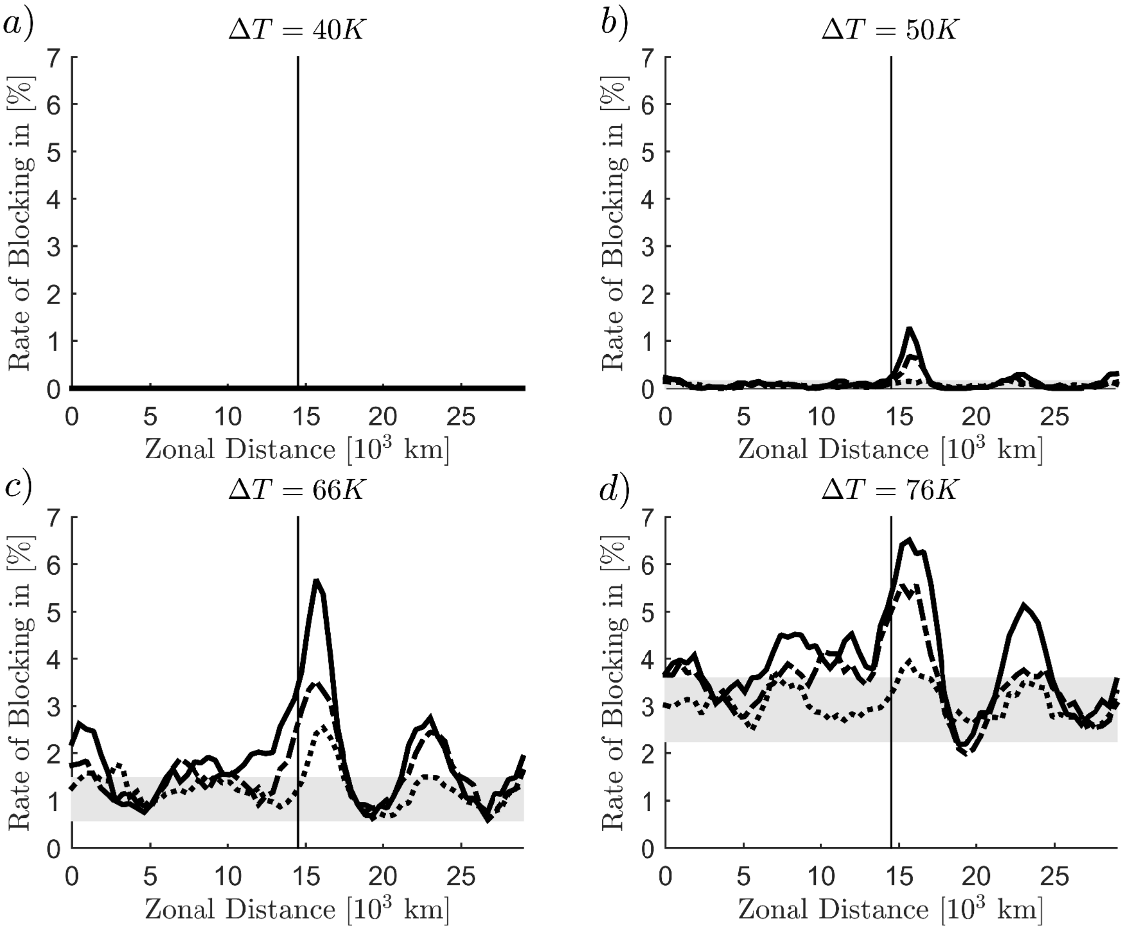

Figure 5.1: The number of blocked days is the highest behind the peak of the orography. The vertical black line indicates the peak of the orography. Downstream two secondary maxima can be identified. The x axis indicates the x coordinate where we detect blocking. The y axis shows the frequency of blocking in percent. The grey shaded area shows the range of the blocking rate along the x direction without orography.

"sub regimes" by computing the mean state of the flow if a particular x coordinate is blocked. Since the days where blocking is present are relatively rare, the mean state over the complete time series is more or less identical to the mean taken over days where no blocking is observed. Close to the blocked area a clear deviation from the zonal symmetric jet of the mean flow can be seen (the blocking high). We also see that the observed blocking is local and the regions far away from the blocked coordinate seem to converge towards the unblocked flow. The unblocked flow is more zonally symmetric then the blocked flow. Nevertheless, there is a non zonal disturbance with wave number four. This shows the presence of topographic Rossby waves induced by the orography (Holton, 2004). Note that the breaking of Rossby waves is intimately connected to the emergence of blocking events and the meandering of the jet fits roughly to the maxima of the blocking rate (Berrisford et al., 2007). The results shown in Figure 5.2 do not change significantly for the other setups and other locations, besides the shift of the blocking high to the

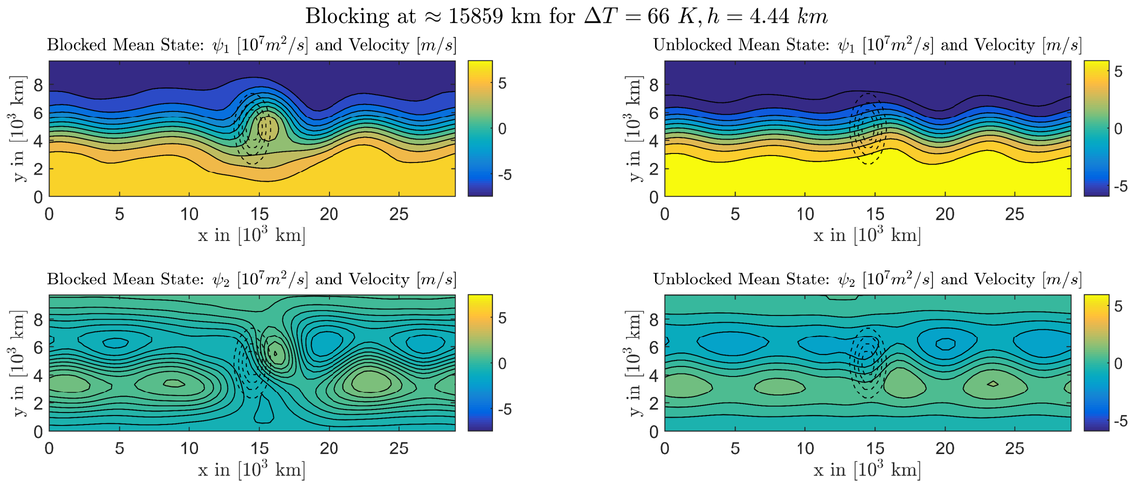

Figure 5.2: As an example of the observed blocking events, the mean blocked state at $x = 15859\,km$ and the unblocked state for $\Delta T = 66\,K$ and $h = 4.44\,km$ is shown. The left panels show the averaged stream function during blocking. The right panels show the average stream function for unblocked periods. The upper panels show the upper layer, the lower panels show the lower layer. The dashed lines show the position of orography. The blocking is affecting the flow only locally because, far from the blocking, the flow is the mean unblocked flow. We get similar results for blockings at different x coordinates and different values of ΔT and h_0.

corresponding x coordinate.

Let us turn our attention towards the number of blockings and their duration. We show the results for the position of the maximum of the blocking rate (see Figure 5.3) but the findings are similar at other x coordinates. The average blocking length (lifetime) changes only marginally, whereas the total number of blockings increases significantly by orography.

For the blocking rate and length (see Figures 5.1 and 5.3), it appears that as aforementioned, adding orography creates preferential geographical locations for the occurrence of blocking. Looking at the global statistics, we observe that, for a given value of ΔT, indeed, the number of blocking events and the number of blocked days increase with h_0, even if the catalyzing effect of orographic disturbances is relatively weaker when ΔT is large enough. The effect of ΔT on the blocking rate and the number of blockings is also found in observations since the meridional temperature gradient is higher in winter and is associated with a higher blocking rate (Tibaldi and Molteni, 1990). The blocking length are, to a good approximation, exponentially distributed, as opposed to the heavy tail properties found in Pelly and Hoskins (2003). Since we are using an extremely simple model of the atmosphere, it is not surprising, that the blocking rates and lengths do not match quantitatively with observations. The lack of many dynamical and physical ingredients in our model is likely to be responsible for this mismatch. Nevertheless, we conclude that the blocking index allows a meaningful definition of a blocked and an unblocked regime

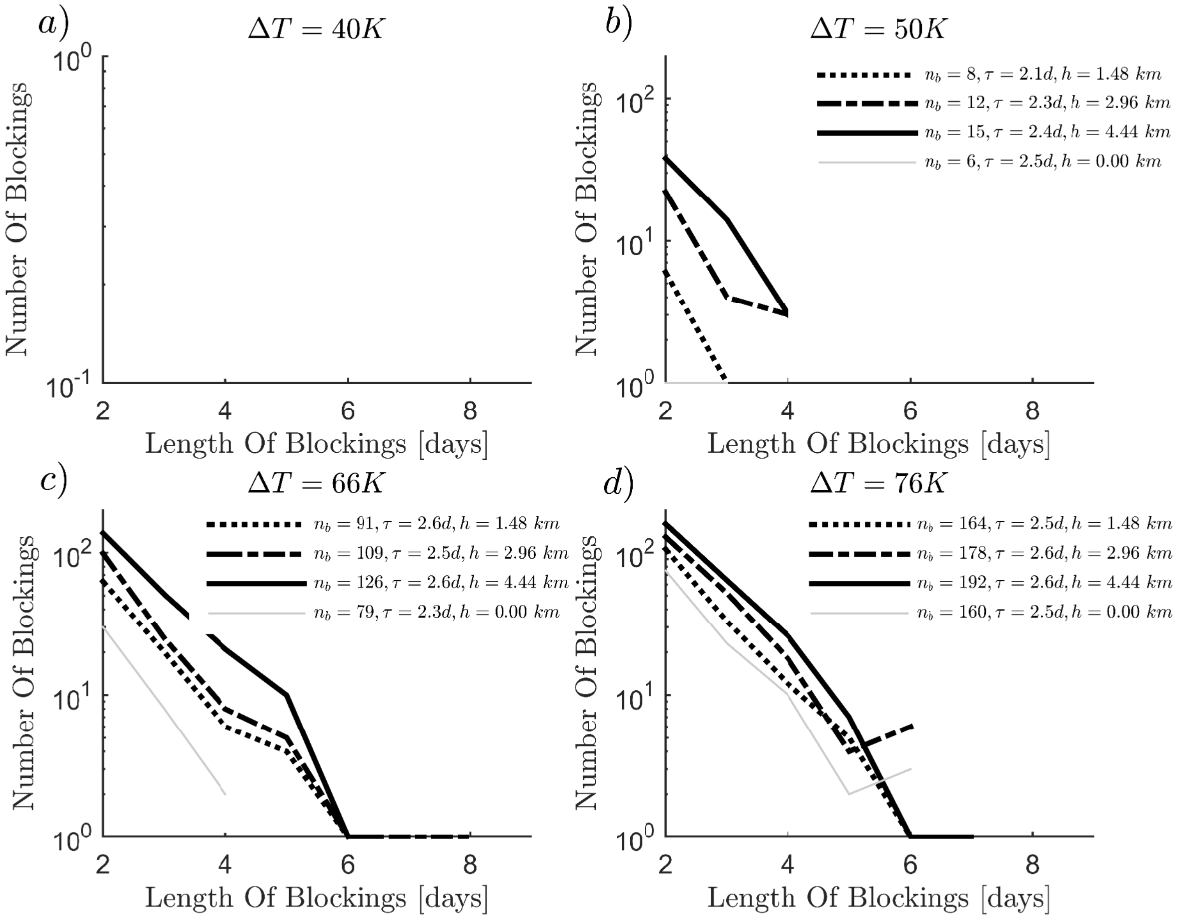

Figure 5.3: The distribution of blocking lengths at $x = 15859\,km$ with Orography in comparison to the control run without orography (light grey). The legends show also the lifetime τ of the blocking events and the number of blocked days per year n_b. The y-axis has a log scaling. The total length of the time series is 115705 days (31.7 years).

and blocking is enhanced if orography is added.

After having discussed the properties and quality of the detected blocking events, we will present in the next section the properties of the CLVs during these phases.

5.3 Properties of Covariant Lyapunov Vectors during Blocking

In this section, we will use the in Section 5.2 established blocked and unblocked phases of the flow to assess the properties of the CLVs during these phases. In Section 5.3.1, the linear stability in terms of the Lyapunov spectrum will be investigated. In Section 5.3.2, we will use the LEC of the CLVs with the background state (see Section 4.2) to explain the changed growth rates of the CLVs during blocking. Also, since blocking is a local change in the flow pattern, we will then continue by analysing the localization of the CLVs during blocking in Section 5.3.3.

5.3.1 Linear Stability of Blocking States

After having clarified in Section 5.2 that indeed we observe blocking events induced by orography, we will now evaluate the characteristics of the CLVs during blocked and unblocked phases. We follow up from the previous section and use the distinction between occurrence of blocking events and regular conditions to partition the attractor of the system. Then, we compute separately the statistical properties of CLVs and LEs in the two regions.

Table 5.1: Properties of the attractor without Orography

ΔT [K]	Positive Exponents	Kaplan-Yorke Dimension	Metric Entropy [1/day]	$1/\lambda_1$ [day]
39.81	17	35.8	0.25	28.8
49.77	55	125.8	3.15	6.8
66.36	88	206.8	12.51	2.6
76.31	98	232.1	18.66	1.9

Table 5.2: Properties of the attractor with Orography

ΔT [K]	Height [km]	Positive Exponents	Kaplan-Yorke Dimension	Metric Entropy [1/day]	$1/\lambda_1$ [day]
39.81	1.48	18	38.1	0.29	26.8
	2.96	19	41.5	0.35	24.5
	4.44	19	41.2	0.34	24.5
49.77	1.48	55	126.9	3.23	6.6
	2.96	55	129.6	3.42	6.4
	4.44	56	131.6	3.56	6.2
66.36	1.48	88	207.1	12.61	2.55
	2.96	88	207.5	12.72	2.54
	4.44	89	207.9	12.85	2.51
76.31	1.48	98	232.2	18.76	1.89
	2.96	99	232.2	18.82	1.89
	4.44	99	232.4	18.88	1.88

Let us start by examining basic dynamical and geometrical properties of the attractor, as we did in Section 4.3.1. Starting from the Lyapunov exponents we can derive the Kaplan-Yorke dimension and the metric entropy, see Tables 5.1 and 5.2.

Table 5.3: Metric Entropy during the blocked and the unblocked phase. This is the sum of the in the long term averaged positive LEs averaged during the blocked and unblocked phases, respectively.

ΔT [K]	Height [km]	Metric Entropy during blocking [1/day]	Metric Entropy no blocking [1/day]
39.81	1.48	-	0.26
	2.96	-	0.35
	4.44	-	0.35
49.77	1.48	3.37	3.20
	2.96	3.63	3.37
	4.44	3.80	3.54
66.36	1.48	12.79	12.53
	2.96	12.87	12.70
	4.44	12.96	12.79
76.31	1.48	18.84	18.66
	2.96	18.84	18.75
	4.44	18.92	18.84

Again, we find that with increasing ΔT the Kaplan-Yorke dimension and the metric entropy grow monotonically. While the observed motions are indeed chaotic for the studied values of ΔT and h_0, we can clearly see from these dynamical indicators that turbulence is much better developed for higher values of ΔT. The impact of the orography on these numbers is small but it shows a small upward trend for larger h_0. This tendency shows that predicting weather (regimes) become(s) more complicated if orography is added because the characteristic predictability time decreases. We take the inverse of the leading LE λ_1 (in Tables 5.1 and 5.2) as a rough measure for predictability since the rapid divergence of nearby trajectories is a necessary ingredient for having a fast error growth. Note that different dynamical indicators are better suited to study the actual predictability of a system. A better evaluation of the time scales of the system and the associated predictability could be obtained by studying systematically finite time/finite size LEs and the related multi-fractal properties (Boffetta et al., 1998, 2003), which is outside the scope of this study.

Let us now turn the focus on the average growth rates during the blocked phases and the unblocked phases. Since blocking conditions are relatively rare, this corresponds to comparing the finite time LEs computed during the blocked phase to the actual long-term LEs at all practical levels. The growth rates of the ten leading CLVs increase significantly during blocking for the two largest ΔT(see Figure 5.4). h_0 does not have an effect on the observed average growth rates. The ten fastest

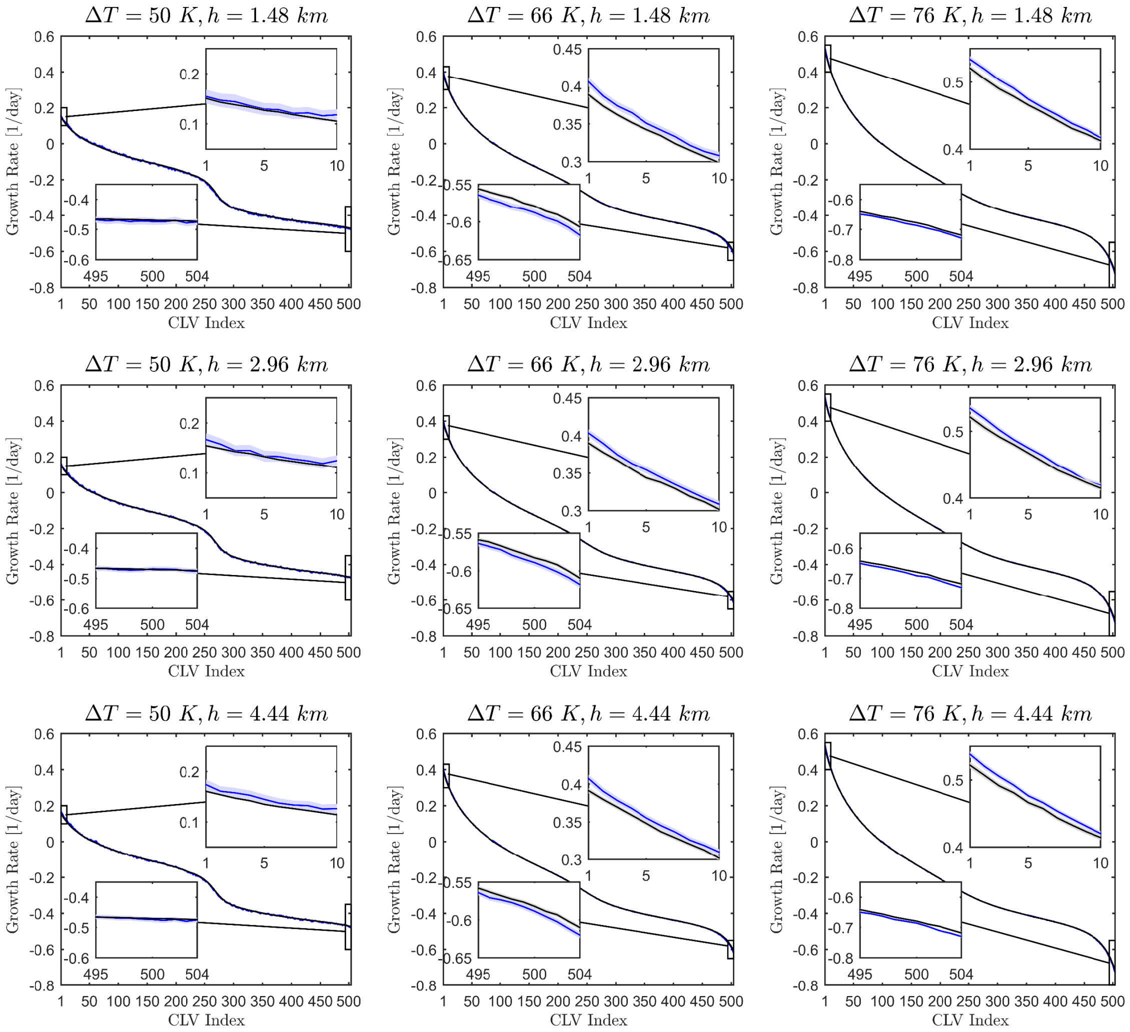

$\Delta T = 50\ K, h = 1.48\ km$ $\Delta T = 66\ K, h = 1.48\ km$ $\Delta T = 76\ K, h = 1.48\ km$

$\Delta T = 50\ K, h = 2.96\ km$ $\Delta T = 66\ K, h = 2.96\ km$ $\Delta T = 76\ K, h = 2.96\ km$

$\Delta T = 50\ K, h = 4.44\ km$ $\Delta T = 66\ K, h = 4.44\ km$ $\Delta T = 76\ K, h = 4.44\ km$

Figure 5.4: For the nine setups where we observe blocking (see Figure 5.1), the figure shows the differences in the growth rates during blocking (in blue color) versus unblocked phases (in black color). We additionally show the 3 σ bars of confidence estimated by computing the degrees of freedom of the time series (shaded areas). For $\Delta T = 66K$, $76K$ we can clearly estimate that for the CLVs with highest/lowest LEs the baroclinic conversion increases/decreases significantly. Such a tendency can not be clearly verified for $\Delta T = 50K$.

decaying CLVs have significantly higher decay rates during the blocked phase. The statistical significance is determined by considering the 3 σ confidence interval which is obtained by computing the degrees of freedom for each time series of the unblocked and blocked growth rates (Leith, 1973). This indicates that the unstable CLVs grow faster globally. The question remains whether this is due to changes in the CLVs near or far away from the blocked region. This question will be partly answered in the next Section 5.3.3 where we will be looking at spatial patterns. Considering that the Lyapunov exponents can be seen as a measure of predictability, the higher values of the positive LEs during blocking suggest that it is hard to predict the decay and onset of a blocked state. See also Table 5.3, where we loosely define a finite time metric entropy evaluated as the sum of the positive LEs taken over the time span where blocking occurs (or not). We would like to remark that while considering larger values of h_0 leads to more frequent blocking events, no significant effect is instead found on the average growth rate of the disturbances. Orography plays an important role as a catalyzer for blocking events. Interestingly, the role is bigger than influencing substantially their properties once they are realized.

5.3.2 Lorenz Energy Cycle during Blocking

In Section 4.3, we explained the growth and decay rate of the CLVs by looking at their Lorenz energy cycle, and studying each term responsible for energy conversions and sinks obtained from the tangent linear equations. Thus, we can provide a physical interpretation of the changes in the growth rates in the phases where blocking is present versus regular conditions (see Section 5.2) by examining the details of the Lorenz energy cycle. We focus here on the budget of the total energy of the j^{th} CLV $(\psi'_{1,j}, \psi'_{2,j})$ resulting from the interaction with the background state $\left(\psi_1^B, \psi_2^B\right)$ and from dissipative processes. For ease of notation, we will use the barotropic stream function $\psi_P = \frac{\psi_1+\psi_2}{2}$ and the baroclinic stream function $\psi_T = \frac{\psi_1-\psi_2}{2}$ as well as the respective geostrophic velocities $\mathbf{v} = (u, v) = (-\partial_y \psi, \partial_x \psi)$ for both fields and $\int d\sigma = 1/(L_x L_y) \int_0^{L_x} dx \int_0^{L_y} dy$:

$$\begin{aligned}\frac{\mathrm{d}}{\mathrm{dt}} E_{tot} = \int d\sigma \Big[&\Delta\psi'_{1,j}\mathbf{v}'_{1,j} \cdot \nabla\psi_1^B - k_h\left(\psi'_{1,j}\Delta^2\psi'_{1,j}\right) + \langle 1 \leftrightarrow 2 \rangle + 2r\psi'_{2,j}\Delta\psi'_{2,j} \\ &-\frac{2}{S}\psi'_{T,j}\mathbf{v}'_{P,j} \cdot \nabla\psi_T^B + 2\frac{\kappa}{S}\psi'_{T,j}\Delta\psi'_{T,j} - 2\frac{r_R}{S}\psi'^2_{T,j}\Big]\end{aligned} \tag{5.2}$$

Since the CLVs are growing/decaying perturbations, we normalize all the following energy conversion terms and sinks by the total energy (in the same manner as discussed in Section 4.2). We decompose the energy rate into the conversions of energy resulting from the coupling with the background state and the energy sinks. The baroclinic and barotropic energy conversion terms are defined as

$$\mathcal{C}_{BC} = \int d\sigma \left[-\frac{2}{S}\psi'_{T,j}\mathbf{v}'_{P,j} \cdot \nabla\psi_T^B\right] \tag{5.3}$$

and

$$\mathcal{C}_{BT} = \int d\sigma \left[\Delta\psi'_{1,j}\mathbf{v}'_{1,j} \cdot \nabla\psi_1^B + \Delta\psi'_{2,j}\mathbf{v}'_{2,j} \cdot \nabla\psi_2^B\right], \tag{5.4}$$

respectively. The energy loss is the sum of newtonian cooling, Ekman friction, and eddy diffusivity.

$$\begin{aligned}S = \int d\sigma \Big[&-2k_h\left(\psi'_{T,j}\Delta^2\psi'_{T,j} + \psi'_{P,j}\Delta^2\psi'_{P,j}\right) + r\psi'_{2,j}\Delta\psi'_{2,j} \\ &+2\frac{\kappa}{S}\psi'_{T,j}\Delta\psi'_{T,j} - 2\frac{r_R}{S}\psi'^2_{T,j}\Big]\end{aligned} \tag{5.5}$$

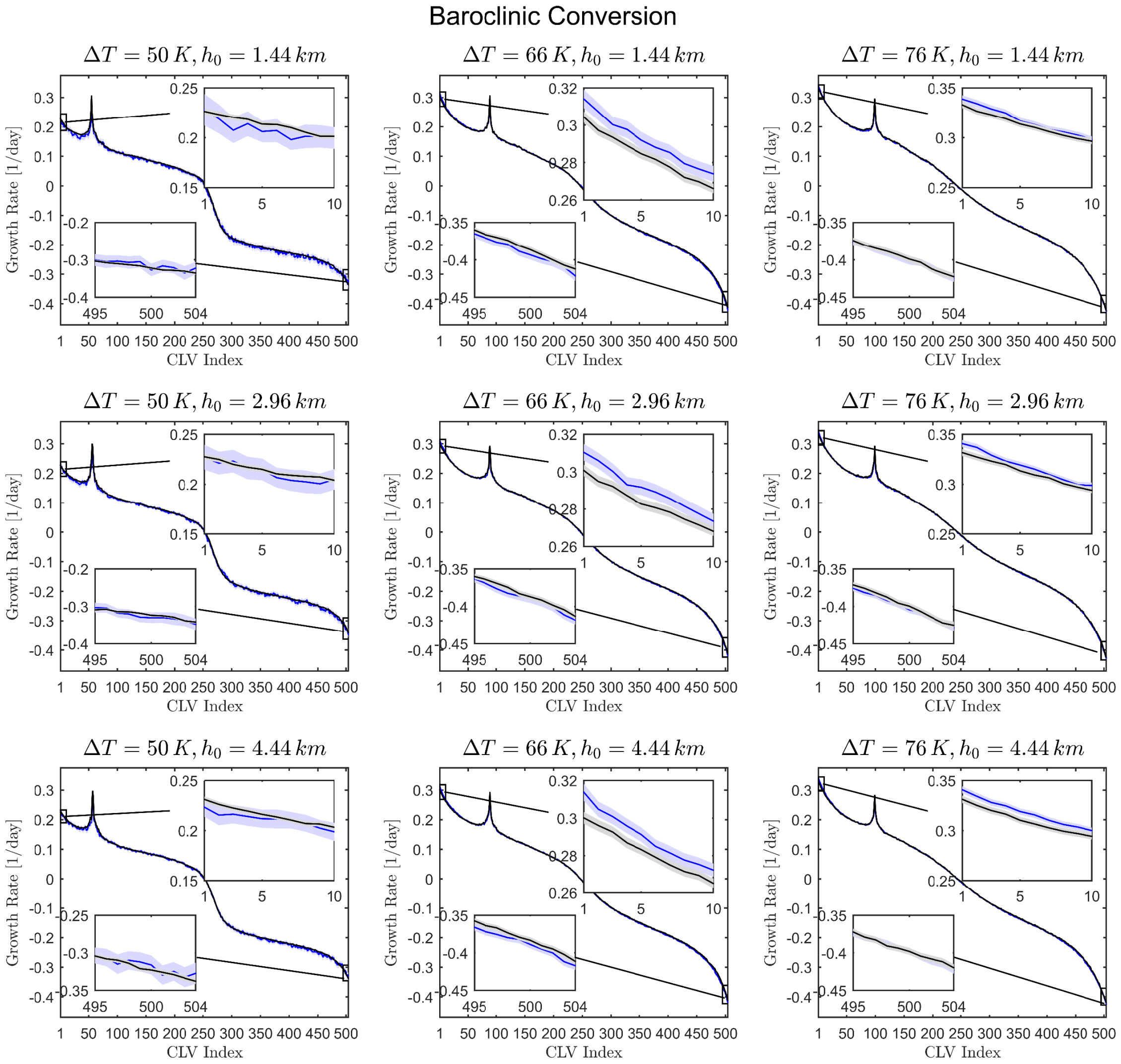

Figure 5.5: For the nine setups where we observe blocking (see Figure 5.1), this figure compares the baroclinic conversion $\mathcal{C}_{BC}$ during blocking (in blue color) versus unblocked phases (in black color). We additionally show the 3 σ bars of confidence estimated by computing the degrees of freedom of the time series (shaded areas). For $\Delta T = 66K$, $76K$ we can clearly estimate that for the fastest growing CLVs, the baroclinic conversion increases significantly. For the fastest decaying CLVs, a negative tendency can be observed yet with weaker statistical significance. Such a tendency can not be clearly verified for $\Delta T = 50K$.

A positive average value for the baroclinic term $\mathcal{C}_{BC}$ implies that available potential energy of the background flow is converted into available potential energy of the j^{th} CLV. The corresponding thermal fluctuations are then converted into kinetic energy of the CLV. Instead, an average positive value of the barotropic term $\mathcal{C}_{BT}$ implies a direct transfer of kinetic energy from the background flow to the j^{th} CLV. As we know from the previous Section 4.2, a positive rate of baroclinic (barotropic) energy conversion rate is associated to a heat (momentum) flux opposite to the temperature (zonal momentum) gradient of the background flow, thereby clarifying

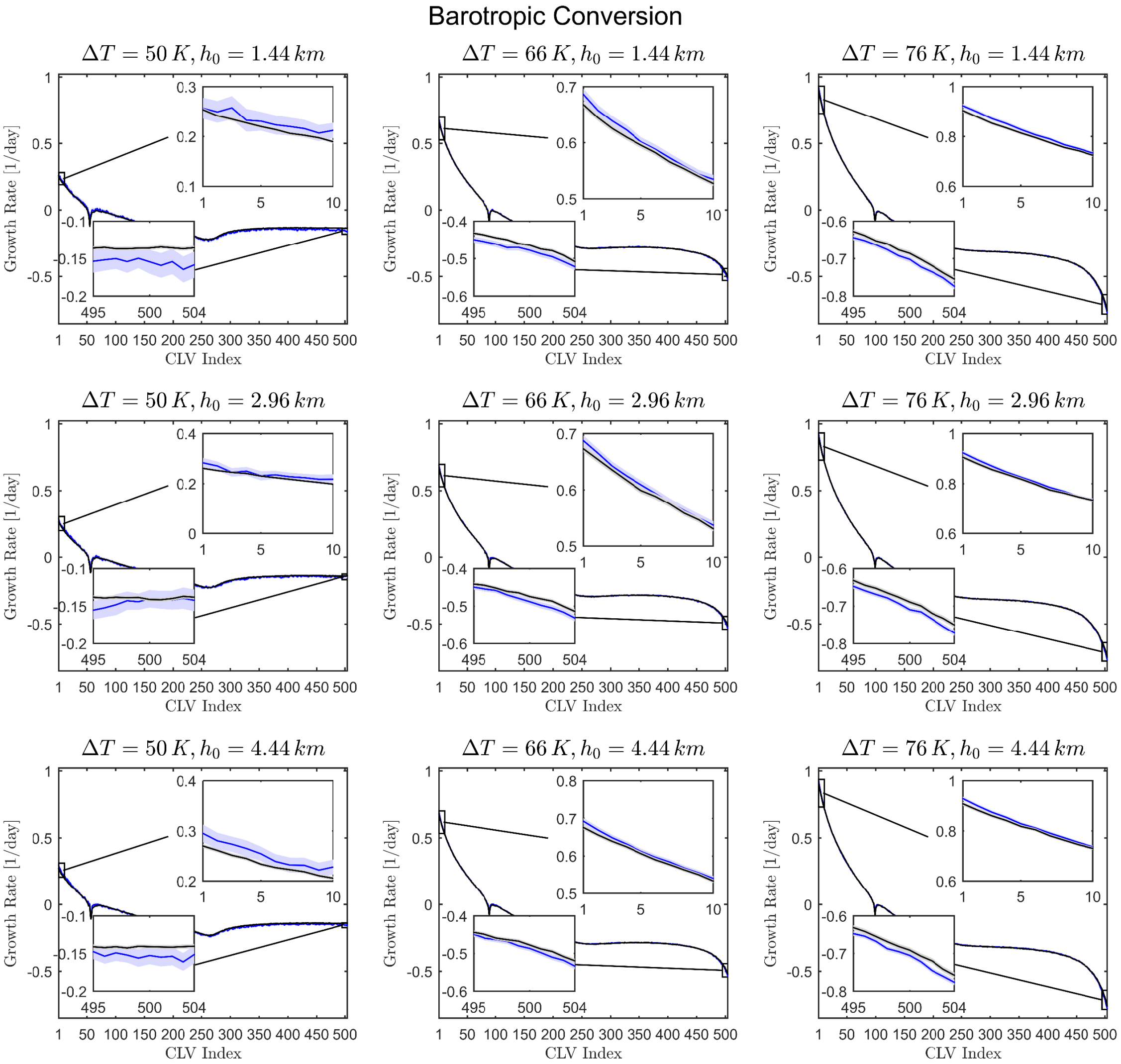

Figure 5.6: For the nine setups where we observe blocking (see Figure 5.1), the figure shows the differences in the barotropic conversion $\mathcal{C}_{BT}$ during blocking (in blue color) versus unblocked phases (in black color). We additionally show the 3 σ bars of confidence estimated by computing the degrees of freedom of the time series (shaded areas). For $\Delta T = 66K$, $76K$ we can clearly estimate that for the CLVs with the highest/lowest LEs, the barotropic conversion increases/decreases significantly. For $\Delta T = 50K$, such a tendency can not be clearly verified.

the presence of negative feedbacks. Clearly, it is a necessary condition for the LE corresponding to a CLV to be positive that at least one of the two terms $\mathcal{C}_{BC}$ or $\mathcal{C}_{BT}$ to be positive on the average.

We can now study how the baroclinic and barotropic energy conversion rates are influenced by the presence of blocked flow conditions. The results are shown in Figures 5.5 and 5.6 for barotropic and baroclinic processes, respectively. For completeness, we have also plotted the result for the energy sinks of the CLVs in Figure 5.7.

For all analyzed configurations and for all CLVs, blocked conditions support smaller

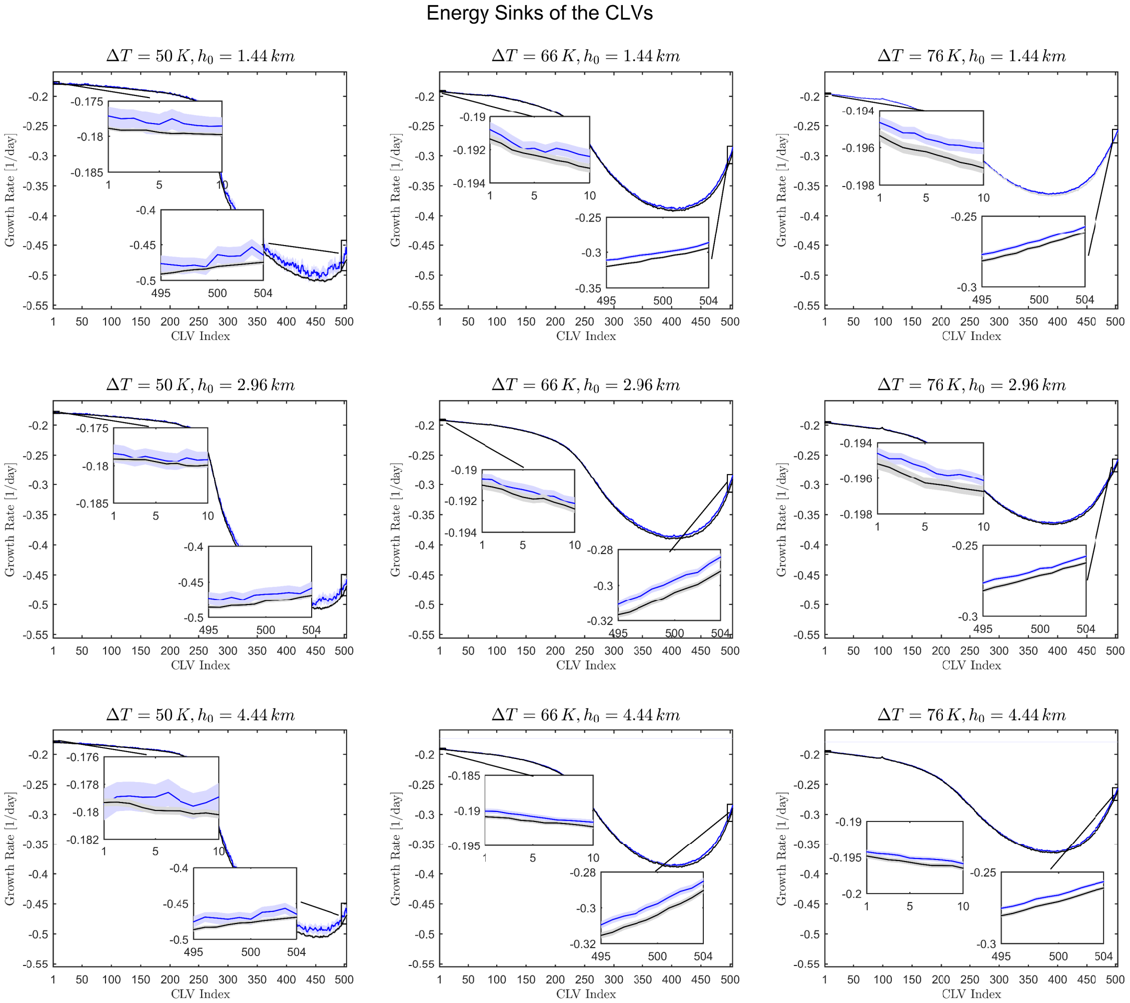

Figure 5.7: The energy losses of the CLVs are the sum of the Ekman Friction, the heat and eddy diffusivity and newtonian cooling (see Section 4.2). For the nine setups where we observe blocking (see Figure 5.1), the figure shows the sum of these terms during blocking (in blue color) versus unblocked phases (in black color). We additionally show the 3 σ bars of confidence estimated by computing the degrees of freedom of the time series (shaded areas). For all ΔT we can clearly estimate that for the CLVs with the highest/lowest LEs, the energy losses decrease significantly.

rates of energy dissipation than regular conditions. Nonetheless, such changes are numerically rather small and can be disregarded in the following discussion.

In the case of weak baroclinic forcing ($\Delta T = 50K$), the difference in the energetics of the CLVs between blocked and normal conditions is borderline or not statistically significant for most CLVs. Despite the lack of strong statistical evidence, some useful indications can be provided. Looking at the unstable CLV, we observe that during blocked phases the baroclinic conversion is lower than in usual conditions, whereas the opposite holds for the barotropic conversion. Therefore, we observe that the (modest) enhanced growth rate of the unstable CLVs observed in blocked conditions (see Figure 5.4) can be attributed to a more efficient barotropic conversion. Looking at the most stable CLVs, the situation is reversed, with barotropic (baroclinic) conversion rates being reduced (increased) in blocked conditions.

The situation changes when considering conditions where stronger baroclinic forcing is imposed on the system ($\Delta T = 66K$ and $\Delta T = 76K$). Blocked conditions are accompanied by stronger baroclinic and stronger barotropic conversion rates for the unstable CLVs, while, conversely, the both conversion rates are reduced when looking at the most stable CLVs.

These results seem to suggest that the energetics of blocking events is fundamentally different in background states featuring weak versus strong Equator to Pole temperature differences. In the former case, blocking is eminently related to modifications to the barotropic instability of the flow, while in the latter case, it results from modifications of both barotropic and baroclinic instabilities. The synergy between the two forms of instability is likely to be responsible for the increase in the number of blocking events for larger values of ΔT. Note that a strong sensitivity of the properties of the low-frequency variability on the intensity of the jet was already envisioned in Benzi et al. (1986) and verified by Ruti et al. (2006).

The properties of the blocked states in terms of the Lorenz energy cycle of the CLVs are weakly dependent on the value of the perturbation orography h_0, which confirms in physical terms the eminently catalyzing role of orography for blocking.

5.3.3 Localization of Covariant Lyapunov Vectors

In Section 2.1, we commented on the benefits of CLVs for investigating the tangent linear dynamics, that is the linear stability of the flow. Other Lyapunov bases describing linear perturbations are not actual trajectories evolving according to the tangent linear equations and they are constraint by the definition of a norm (Pazó et al., 2010). Also, as mentioned before, it has been shown that they are sensible to orographic disturbances (Szendro et al., 2008). Therefore, they are a good choice for finding the signature of blocking in the tangent linear dynamics.

For this, we will assess the localization of the CLVs during blocking conditions and compare it with what observed in normal unblocked phases. A measure for the localization is given by the temporal variance of the CLVs at the grid points on the domain. In the control runs without orography, the variance of the CLVs does not depend on x. If the zonal symmetry is broken due to orography, the CLVs will be localized in the x direction (Szendro et al., 2008). In Figure 5.8, we show, as an example, the variance of three CLVs in the blocked phase and the unblocked phase for the blockings shown previously in Figure 5.2 (for $\Delta T = 66\,K$ and $h_0 = 4.44\,km$ and blocking at $x_b = 15859\ km$). Figure 5.8 shows a clear impact of the blocking on the variance of the CLVs. Overall, the variance is localized in the meridional direction due to the symmetry break associated with the boundary conditions at

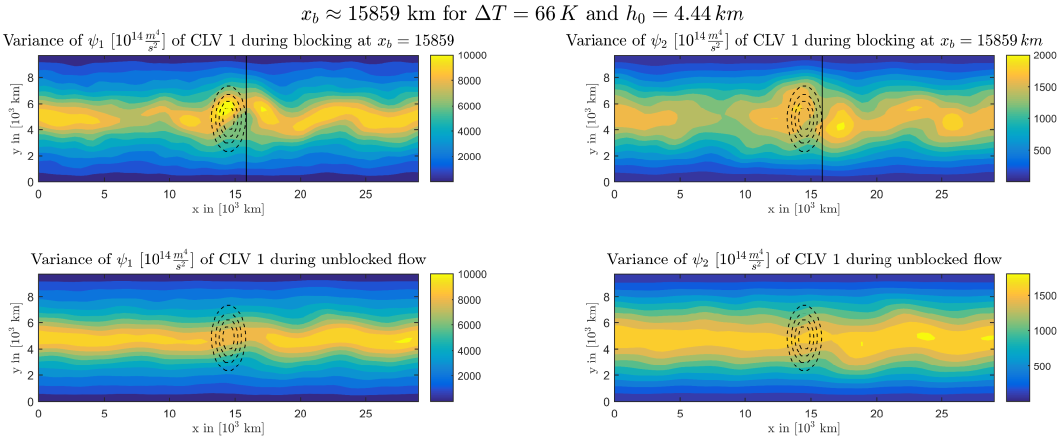

(a) The first CLV

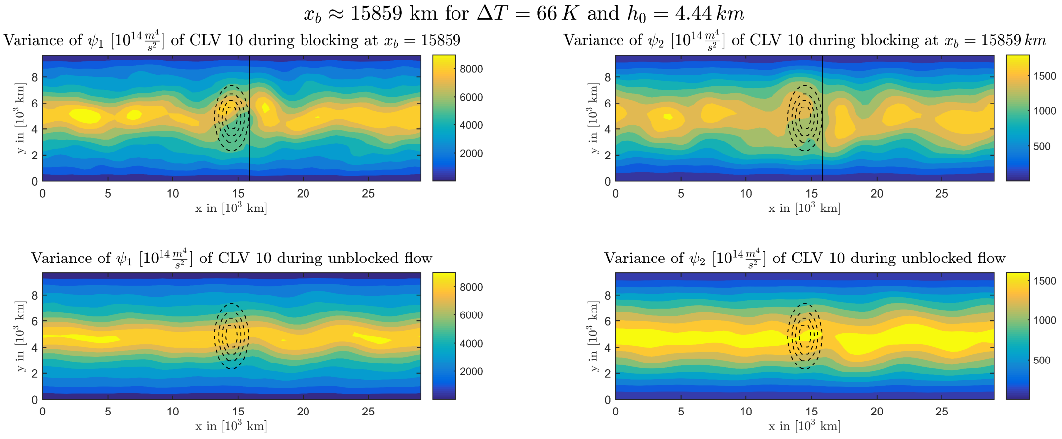

(b) The 10^{th} CLV

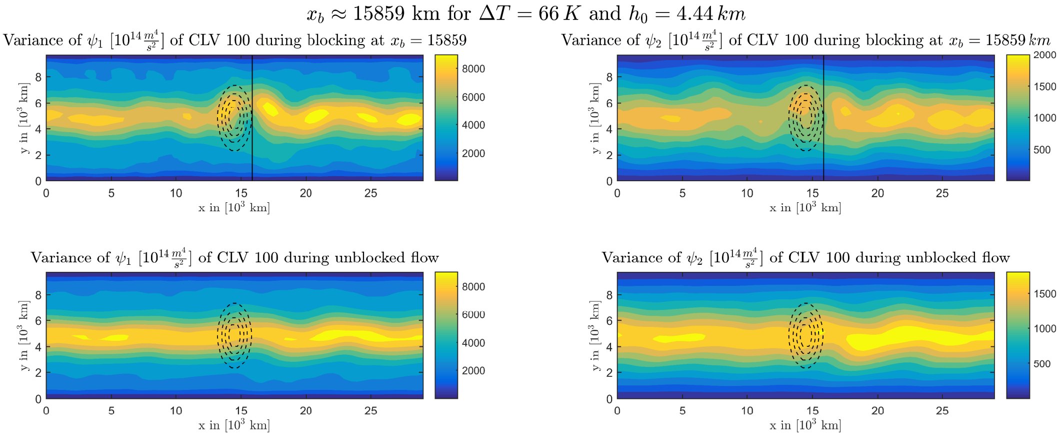

(c) The 100^{th} CLV

Figure 5.8: Variance of selected covariant Lyapunov vectors (1^{st} (a), 10^{th} (b), 100^{th} (c)). The stream function is shown (left side: ψ_1, right side: ψ_2). The blocked state, which is blocked at the vertical black line, is shown in the upper parts. The unblocked phase is shown in the lower parts. The orography is shown by dashed lines.

$y = 0, \pi$, but at the location of the blocking the variance is shifted northward. In the zonal direction, the variance has a weak x-dependence (even if we have no reasons to expect zonal symmetry) during the unblocked phase. Away from the blocking, we see again a non zonal disturbance with wave number four in both phases (see Section 5.2). Note that at the location of the block in the background state, the CLVs show a minimum of the variance (see Figure 5.2).

Before we discuss the implications of these results, we would like to analyze the variance for all CLVs by slightly reducing the complexity of the data. We average the variance along the meridional direction and focus on the x-dependence only. Furthermore, we do not analyze the average localization of the CLVs, but instead track the variations of the localization. Hence, we compute the ratio of the meridional average of the variance of the stream function of the CLVs (upper and lower layer) during blocking at a particular x_b

$$\sigma^{1/2}_{x_b}(x) = \frac{1}{|T_{x_b}|} \int_{t \in T_{x_b}} dt \int dy \left(\psi_{1/2}(x,y,t)^2 - \left\langle \psi_{1/2} \right\rangle^2 \right)$$

and during the unblocked phase

$$\sigma^{1/2}_{unbl}(x) = \frac{1}{|T_{unbl}|} \int_{t \in T_{unbl}} dt \int dy \left(\psi_{1/2}(x,y,t)^2 - \left\langle \psi_{1/2} \right\rangle^2 \right).$$

We define the set T_{x_b} to contain all time steps where the flow is blocked at x_b and T_{unbl} to contain all time steps which are not blocked. $|T|$ is the length of the respective phases. Our measure for the change of localization $\Delta\mathcal{L}$ in the zonal direction has then the following form.

$$\Delta\mathcal{L}(x) = \frac{\sigma^{1/2}_{x_b}(x)}{\sigma^{1/2}_{unbl}(x)} \tag{5.6}$$

Note that $\langle \cdots \rangle$ is the average along the complete time series. If $\Delta\mathcal{L} > 1$, then a higher activity of the CLV (y-axis) during blocking at a particular zonal coordinate (x-axis) is implied. The vertical dashed line is a reminder for the position of the peak of orography along the channel. We show the results for the upper layer stream function ψ_1 (left panel) and the lower layer stream function ψ_2 (right panel). We see that the activity of almost all CLVs is higher close to the blocking and lower in the rest of the channel. As an example, Figure 5.9 shows the results of the above Equation (5.6) for the three local maxima of the blocking rate for $\Delta T = 66\,K$ and $h_0 = 4.44\,km$ (see Figure 5.1). The other setups show similar results. The CLVs cluster around the region where blocking is detected. Note that the clustering occurs almost regardless of growth rate of the CLVs. Moreover, the localization in the lower layer is less strong, which explains the reduction in the dissipation during the blocked phases discussed before. The variance of the CLVs at the center of the blocking is lower. This indicates that stability is higher in the center of the blocking compared to its borders. In order to clarify unambiguously this point, the adjoint CLVs would have to be considered. These allow for projecting in a meaningful way

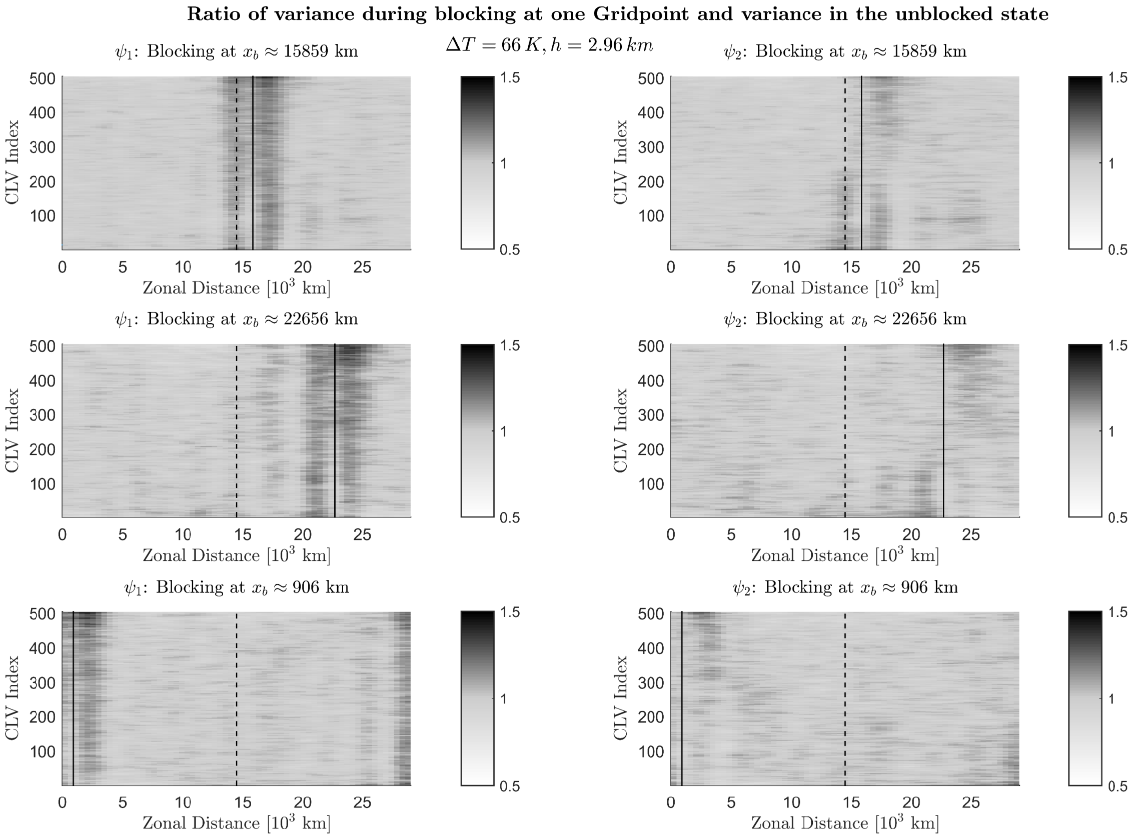

Figure 5.9: Since the localization of the CLVs is similar for the different setups with blocking events, we show here only results for $\Delta T = 66K$ and $h = 4.44$ km. For every CLV (y-axis) we show the quotient of the meridionally averaged variance during blocking at a particular x coordinate (vertical solid black lines) and unblocked phases ($\Delta\mathcal{L}$ in Equation (5.6)).

an arbitrary perturbation onto the non-orthogonal basis given by the CLVs. For a given time horizon, one could then obtain a characteristic growth/decay rate of linear perturbations in an arbitrary region of the flow. Note that using orthogonal Lyapunov vectors for this analysis would change the results. We can illustrate this by considering the example of optimal perturbations by Buizza and Molteni (1996). Here, only the first optimal perturbation localizes close to the blocking, because it converges for long optimization times towards the first CLV. The remaining optimal perturbations can not behave in this way (see comments in Section 2.1). The results obtained using the physically relevant CLV basis underline that a transition to a blocked state is a change in the flow regime which effects all time scales and processes. Hence, the linear dynamics of blocking events can not be reduced to a small number of changes on certain time scales and consequently, the detection of blocking events should take this into account.

We think these results encourage to search for a blocking detection scheme based on criteria employing all CLVs. This definition of blocking would have the advantage of clearly linking the local stability to the presence of a blocking regime. Moreover, such an approach would also allow for a more natural and intuitive definition of blocking because linear stability is directly tied to the persistence of a regime.

5.4 Summary and Discussion

In this chapter, we studied blocking events in a very simplified atmospheric model of the mid-latitudes. Blocking events are persistent deviations of the jet stream in the mid latitudes from the usual quasi zonal symmetry. Naturally, blocked states possess very unusual properties in terms of weather forecast and it is especially difficult to predict the onset and decay of blocking events. It is well known that orography plays a major role in fostering the occurrence of blocking. Thus, contrary to the experimental setup from Chapter four and in the spirit of previous analyses of blocking, we added an orographic forcing in order to produce enhanced blocking events in the flow (Charney and Straus, 1980). As orography, we used a Gaussian bump placed in the middle of the channel. We investigated four different values of ΔT (40 K, 50 K, 66 K and 76 K) in order to assess different degrees of large scale turbulence. The impact of orography was investigated with three different heights h_0 (1.48 km, 2.96 km and 4.44 km).

While such a setting is outdated and insufficient in terms of providing a realistic statistics of blocking events, it provides qualitatively meaningful results and contains some of the essential physical and mathematical ingredients. We wanted to consider, namely the possibility of having a turbulent state featuring a convincing Lorenz energy cycle fuelled by barotropic and baroclinic instabilities and damped by a variety of dissipative effects.

The main plus of such a simple model is that we are able to construct the CLVs, which are the covariant unstable and stable modes of the turbulent flow and provide a physical representation of the natural fluctuations of the flow. CLVs provide a complete description of the dynamics and geometry of the attractor of the system and are useful for providing a new characterization of the properties of blocked versus regular conditions. Consequently, as we pointed out throughout this thesis, CLVs are the suitable choice for such an investigation (see Section 2.1). We want to emphasize that our model is only a first step towards identifying the signature of the blocking events in the CLVs for a variety of models.

We detected the blocking events with an Tibaldi-Molteni scheme (Tibaldi and Molteni, 1990). Given the simplicity of the model we adopted, it is no surprise that the statistics of the events we label as blocking are only in qualitative agreement with what found in observations for all configurations we consider. Nevertheless, we show that the detected events are indeed blocking highs which divert the jet stream from its zonal symmetry. In the unblocked phase, it is also comforting to see that, the flow is more zonally symmetric and its mean state exhibits topographic Rossby waves. For higher meridional temperature gradients ΔT presence of the blocking rates increased, accompanied by a modest increase of its life time. The orography created localized regions of high blocking rates. Such regions were located downstream of the orographic disturbance and their prominence was more evident when higher mountains are considered. The orographic influence was weaker when adopting a stronger baroclinic forcing.

Each CLV is associated to a LE, which measures its average growth (for unstable CLVs) or decay (for stable CLVs) rate. Therefore, we have analyzed separately the growth rate of the various CLVs during the blocked and regular regimes. Furthermore, the spatial variance during the blocked and unblocked phases is used for the localization of the CLVs. Our results show a significant increase of the growth rate of the leading CLVs during blocked phases. Thus, the flow is more unstable during blocking. This might be interpreted as a trade off effect between increased stability in the blocked regions and less instability elsewhere in the flow. The increased instability also indicates that the transition from the blocked regime is in general difficult to predict. We have complemented the analysis of the instabilities by investigating the Lorenz energy cycle of the various CLVs and looking at the baroclinic and barotropic conversion rates. The enhancement of the growth rate in the blocked phase for the leading unstable CLVs is due to a strengthening of both barotropic and baroclinic conversion rates for intermediate and high values of ΔT. Instead, for low values of ΔT, enhanced instability of the unstable CLVs during blocked phase results from an enhancement of barotropic instability only. This clarifies that the dynamical processes behind blocking events are not the same in conditions of low versus high baroclinicty of the background flow. The localization of the CLVs is clustered around the blocked area. This hints for an increased instability at the boundaries of the detected blocking events and possibly, for more stable conditions at the center of the blocking. Given the fact that it is possible to find signatures of blocking across all CLVs, we think the results encourage to create a blocking definition which employs information from the various different processes on all time scales described by the CLVs.

Chapter 6

Conclusion and Outlook

Before we make our final concluding remarks and give an outlook for future research, we would like to give a short overview of the results. In this thesis, we extended classical linear stability analysis to chaotic non-linearly evolving flow of the mid latitudes atmosphere. The appropriate basis in tangent linear space to conduct such an investigation are the CLVs because they are the only Lyapunov vectors that are non-orthogonal and covariant with the tangent linear dynamics, thus they can be identified with nearby trajectories (see Chapter two). Note that the CLVs reduce to the classical normal modes when computed for fixed states. As a first step in a hierarchy of models, we chose to obtain the CLVs for a two-layer QG model featuring the basic baroclinic and barotropic processes commonly observed in the mid latitude atmosphere. The model is driven by a meridional temperature gradient ΔT and is dissipating energy via Ekman friction (see Chapter three). In Chapter four, we investigated three different ΔT representing different stages of well developed chaos (see Section 3.2.1) and we first demonstrated a straightforward generalization of the classical concept of a LEC for normal modes to the CLVs. This means the CLVs are subject to barotropic and baroclinic conversions imposed by the background state and they loose energy via dissipation and friction. This generalized LEC for CLVs is closely related to the classical LEC between the zonal mean and the eddy field featuring similar relations between transports of heat and momentum and the energy conversions (see Section 4.2). The energy growth described by the LEC of the CLVs can be connected to their euclidean norm growth rate because the euclidean norm and the energy norm are equivalent norms. We observe that CLVs with higher LEs gain energy via the baroclinic conversion, while energy is mainly lost by friction and diffusion. This is accompanied by a northward heat transport, while warm air rises in the south and cold air sinks in the north of the channel. For the lower negative LEs these processes are inverted. These qualitative features do not depend on ΔT. For the barotropic conversion, the fastest growing CLVs (for the two largest values of ΔT) gain energy by transporting momentum away from the baroclinic jet of the background trajectory. For slow growing CLVs and all decaying CLVs the barotropic conversion is always negative. It was not surprising to find that a positive baroclinic conversion was not a sufficient condition for a growing CLV. Instead, the sum of baroclinic and barotropic conversion minus dissipation determined the respective growth rates of the CLVs. Nevertheless, all growing CLVs were always baroclinically unstable. We then reconstructed the variance of the background state in a similar fashion to the application of EOFs. Here, the baroclinically active CLVs reconstruct reliably the variance of the background state with 95% for all setups. In Chapter five, we aimed at studying the fluctuations of the background state instead of the long term behavior. Therefore, we investigated blocking events as an example for a typically observed weather regime. In order to enhance the emergence of blocking, we added an orographic forcing with the shape of a Gaussian bump to our model and varied besides ΔT also the height h_0 of orography. Despite the weak manifestation of blocking events in the model, we can detect reasonable blocked and unblocked phases by employing a Tibaldi-Molteni detection scheme (Tibaldi and Molteni, 1990). Using this separation, the properties of the CLVs can be analyzed, respectively. We find in Section 5.2 that blocking increases with a higher meridional temperature gradient ΔT and is additionally enhanced by orography, which, by breaking the zonal symmetry, contributes as a catalyst to the process through a phase lock mechanism that allows standing perturbations to grow, as envisioned in Benzi et al. (1986). The spatial variance of the CLVs is dominantly located around the region where blocking occurs when compared to the average variance during unblocked phases (see Section 5.3.3). Furthermore, the growth rates of the fastest growing CLVs are higher during blocked phases, pointing at the fact that the system has globally a lower predictability during blocked phases. Possibly, this is as a result of the difficulty of predicting the onset and decay of the blocking events (see Section 5.3.1). We explain the changed growth behavior by using a generalization of the Lorenz energy cycle between the CLVs and the background state introduced in Section 4.2. We find that the increased instability is dominantly caused by an increased input of energy to the CLVs by baroclinic and barotropic conversions for high values of ΔT, while, for weakly baroclinic flows, the intensification of barotropic instability is the only active mechanism (see Section 5.3.2).

The results of this thesis show that the mean and the fluctuations of the CLVs' growth rate can be understood in terms of the LEC and the associated transports. It is remarkable that they can be used to characterize the linear stability of the background state over arbitrary long time intervals but also with respect to relatively short lived deviations (weather regimes). Therefore, the CLVs are not just an abstract mathematical tool. They offer two benefits at the same time: the physical interpretation in terms of nearby trajectories and the explanatory power for the observed variability. In contrast, the traditional stability analysis of single states or the use of other Lyapunov bases for chaotic/turbulent flows are not able to provide a comparable coherent connection between the linear stability and a physical interpretation. This connection is missing in both cases because they are not a solution of the tangent linear equation for such flows.

As we discussed in Section 2.2, the future potential of the CLVs lies in their efficient description of the stable and unstable manifold. The findings presented give us confidence that using CLVs in the context of earth system modeling and meteorology is of significant value and may offer valuable insight in future research. Therefore, we would like to proceed by proposing some directions of possible future research.

As we repeatedly stated in this thesis, we considered a minimal model of the mid latitudes atmosphere. This should only be a first step within a hierarchy of meteorological and earth system models for obtaining the CLVs. It seems promising to employ models featuring multiple temporal and spatial scales. Results from Posch and Hirschl (2000) support this stance. They found Hydrodynamic Lyapunov Modes (HLMs) which are very slow growing backward Lyapunov vectors that posses a large scale structure describing macroscopic processes, whereas the fast growing BLVs describe small scale instabilities. Interestingly, an unambiguous characterization and detection of HLMs is provided by the CLVs (Romero-Bastida et al., 2012). Clearly, our QG model was not suitable for investigating these interesting aspects of multi scale systems. In fact, analyzing the spectral density of the CLVs, we find that they do not differ in terms of their spatial or temporal scales. Moreover, we find that they have very broad spectral structures which is in agreement with the findings by Herrera et al. (2011) who observed that the CLVs rather possess heavily localized wave-like features which locally convert and dissipate energy. In our analysis of blockings in Chapter five, we also found that all CLVs have similar spatial scales and that the LEs, apart from those very close to zero, are similar. Hence, it seems worthwhile to follow the more specific ideas by Gallavotti (2014) who suggested that in multiscale systems, it should be possible to associate the different spatial and temporal scales of motion (e.g. macroscopic, mesoscopic and microscopic) to specific subsets of CLVs and related LEs. In particular, there is reason to expect that highly localized (extended) unstable CLVs might be associated to large (small) growth rates resulting from local (global) instabilities. Thus, our results are an "a posteriori" confirmation of the self-consistency of the scale analysis leading to the QG approximation.

It is tempting to follow this idea of investigating the vast amount of meteorological instabilities, but as mentioned before one needs to consider more complex models than the one adopted here. In particular, in a primitive equation model one could see whether it is possible to recognize small scale CLVs with high growth rate associated to mesoscale instabilities, while additionally, CLVs associated to convective events should be found when non-hydrostatic models are adopted. Potentially, these models would also allow for an analysis of the aforementioned HLMs. The HLMs could then maybe used to derive a parameterization from the respective statistics of the different scales which is similar to the approach of Majda et al. (2001).

Besides a primitive equation model, another possibility is to use the formalism of

CLVs and associated LEs to study a fluid model encompassing regions with different inertia and thermal inertia. A conventional method would be to use a coupled atmosphere-ocean model, which would allow to rigourously define and study, e.g., coupled modes of variability. Recently, Vannitsem and De Cruz (2013) have proposed a low-order atmosphere-ocean model which is a perfect candidate for this sort of studies. In such a model, the advantage of computational feasibility and capturing important aspects of the earth system dynamics would remain. It might be even beneficial to study the already mentioned approaches in a Lorenz 96 model featuring a coupling which allows to control the multiscale separations directly (Lorenz, 1996; Wilks, 2005).

It is also promising to study higher resolutions of a simple model of the atmosphere given the discovery of wave-dynamical and damped-advective Floquet vectors by Wolfe and Samelson in a high resolution QG two layer model (Wolfe and Samelson, 2006, 2008). We speculate that this might be related to the splitting of the CLVs into subsets of spurious and physical modes found by Yang et al. (2009) which we discussed in Section 2.2. The physical modes might allow for constructing the inertial manifold. This is a very promising approach for constructing reduced models in a rigorous way. In the context of the reduction of complexity, we speculate that the surprising efficiency of the baroclinically active CLVs in explaining the variability of the background might be another way to construct a reduced model without this splitting (see Section 4.4).

Moreover, the CLVs should be considered in the context of Ruelle's linear response theory (Ruelle, 1998; Lucarini and Sarno, 2011; Lucarini et al., 2014; Ragone et al., 2015) because they are a basis for the linear response operator of an arbitrary perturbation to a dynamical system. This means, the knowledge of CLVs for an unperturbed system would allow to construct the response of the ensemble mean to an arbitrary perturbation of the equations of motion. This would also allow for studying which type of perturbations lead to a large non-linear response. This could be a way for rigourously defining whether tipping points are close to the unperturbed dynamics.

This thesis shows that the CLVs provide a link between rather mathematical properties and the energetics of baroclinic and barotropic conversions. Given the potential of the above outlined suggestions for applications of CLVs, such connections between dynamical system theory and geosciences should be even more exploited. Both fields can benefit from this exchange: The geosciences by getting more rigorous objective tools for understanding climate models and dynamical system theory by getting a real world test case for studying high dimensional chaos.

References

Symbols

a	Aspect Ratio Of Domain
$B_j(t)$	Backward Lyapunov Vector
$B_j(t)$	Backward Lyapunov Vector
β	Beta Parameter of Coriolis Effect
$\mathcal{B}_n^{un}(t)$	Span of n CLVs at time t from most unstable CLV
$\mathcal{B}_n^{s}(t)$	Span of n CLVs at time t from most stable CLV
$c_j(t)$	Covariant Lyapunov Vector
$C_{ZK\rightarrow EK}$	Energy Conversion: Zonal Kinetic To Eddy Kinetic
$C_{ZP\rightarrow EP}$	Energy Conversion: Zonal Potential To Eddy Potential
$C_{EP\rightarrow EK}$	Energy Conversion: Eddy Potential To Eddy Kinetic
$C_{ZP\rightarrow ZK}$	Energy Conversion: Zonal Potential To Zonal Kinetic
$\mathcal{C}_{BC}$	Baroclinic Conversion for CLVs
$\mathcal{C}_{BT}$	Barotropic Conversion for CLVs
$\mathcal{C}_{PK}$	Conversion from Potential to Kinetic Energy for CLVs
ΔT	Forced Meridional Temperature Gradient
Δp	Pressure Scale
Δ	Deviation allowed used for Blocking Detection
D_{KY}	Kaplan-Yorke-Dimension
E_{pot}	Potential Energy
E_{kin}	Kinetic Energy
E_{tot}	Total Energy
f_0	Coriolis Parameter
$\mathcal{F}(t_2, t_1)$	Linear Propagator
$F_j(t)$	Forward Lyapunov Vector
$F_j(t)$	Forward Lyapunov Vector
h	Orography Field
h_0	Height of Orography
H	Height of Atmosphere
$J\left(\cdot,\cdot\right)$	Advective Jacobian
κ	Eddy-Heat Diffusivity
k_h	Eddy-Momentum Diffusivity
$\lambda_j(t)$	Finite Size Lyapunov Exponent
λ_j	Lyapunov Exponent
$\Delta\mathcal{L}$	Localization Measure of the CLVs
L_x	Zonal Extent Of Domain
L_y	Meridional Extent Of Domain
$\mathbf{p}_n^{un/s}(t, t_R)$	Orthogonal Projection of $\mathbf{x}(t)$ onto $\mathrm{B}_n^{un/s}(t_R)$
ψ	Geostrophic Stream Function
$\delta\psi_N$	averageψ in northern part for blocking detection

$\delta\psi_S$	averageψ in southern part for blocking detection
r_R	Thermal Dampening
r	Ekman Friction
R	Specific Gas Constant
S	Stability Parameter
$\mathcal{S}_{EEF}$	Eddy Ekman Friction
$\mathcal{S}_{EHD}$	Eddy Heat Diffusion
$\mathcal{S}_{EKD}$	Eddy Kinetic Diffusion
$\mathcal{S}_{ENC}$	Eddy Newtonian Cooling
$\mathcal{S}_{ZEF}$	Zonal Ekman Friction
$\mathcal{S}_{ZHD}$	Zonal Heat Diffusion
$\mathcal{S}_{ZKD}$	Zonal Kinetic Diffusion
$\mathcal{S}_{ZNC}$	Zonal Newtonian Cooling
$\sigma_{x_b}^{1/2}$	Mean Spatial Variance while x_b is blocked
$\sigma_{unbl}^{1/2}$	Mean Spatial Variance while unblocked flow
σ_x	Zonal Length Scale Of Orography
σ_y	Meridional Length Scale Of Orography
τ	Average Lifetime Of Blocking Events
n_b	Number of Blocked Days per Year
u	Zonal Geostrophic Velocity
u_N	Average u in Northern part for Block Detection
u_S	Average u in Southern part for Block Detection
v	Meridional Geostrophic Velocity
$\mathbf{v}$	Geostrophic Velocity Vector
$V_j^+(t)$	Forward Lyapunov Subspace
$V_j^-(t)$	Backward Lyapunov Subspace
$W^+(t)$	Far Future Operator
$W^-(t)$	Far Past Operator
ω	p-velocity at level 1.5 (500 hPa)
x	Zonal Coordinate
y	Meridional coordinate
y_S	Southern y coordinate f. Blocking Detection
y_0	Middle y coordinate f. Blocking Detection
y_N	Northern y coordinate f. Blocking Detection

Acronyms

BLV	Forward Lyapunov Vector
CLV	Covariant Lyapunov Vector
EMD	Eddy Mean Decomposition
EOF	Empirical Orthogonal Functions
FFT	Fast Fourier Transform
FLV	Backward Lyapunov Vector
GCM	General Circulation Model
HLM	Hydrodynamic Lyapunov Modes
PDE	Partial Differential Equation
LEC	Lorenz energy cycle
LE	Lyapunov Exponent
QG	Quasi Geostrophy

Subscripts, Superscripts and Annotations

X_1	Upper Layer X
X_2	Lower Layer X
X_P	Barotropic X
X_T	Baroclinic X
X^E	Eddy Component
$[X]$	Zonal Mean
X'	Linear Perturbation
X^B	Background State

List of Figures

2.1 A schematic view of the algorithm proposed by Ginelli et al. (2007). The picture is inspired by Kuptsov and Parlitz (2012) 14

3.1 The domain of the QG model. The right panel shows in dashed lines a potential orographic forcing imposed on $\omega_{2.5}$ 18

3.2 These snapshots show the stream function fields for the upper and lower layer. The upper is on the left side and the lower layer is found on the right side. Note that in order to use a grey scale, the scale of the colorbars is different in every panel. The flow shows a clearly baroclinically unstable and barotropically stable configuration (see Section 4.1) 22

4.1 The mean state of the trajectory (averaged over a period of 25 years) for the three forced meridional temperature gradients ΔT (dotted: $39.81K$, dashed: $49.77K$, solid: $66.36K$). The superscript E indicates the eddy terms. 26

4.2 Flow Chart of the Lorenz energy cycle for three ΔT (Units of Conversions are $10^5 m^2/s^3$). The arrows indicate the average sign of the energy conversions, sinks and sources of the zonal and eddy energies. For every temperature gradient ($\Delta T_1 = 39.81K$, $\Delta T_2 = 49.77K$ and $\Delta T_3 = 66.36K$) the dominant source of energy is Newtonian cooling, which inputs energy to the zonal mean potential energy. The important conversions are the baroclinic conversion which is related to the northward heat transport (see Figure 4.1 c) and the barotropic conversion related to the center pointed momentum transport (see Figure 4.1 d). The main energy losses occur by converting the potential energy of the eddies into kinetic energy, where it is lost mainly due to kinetic diffusion and Ekman friction. We observe an intensification of the cycle for a larger meridional temperature gradient ΔT. 29

4.3 The graphs show the modulus of the average correlation $\frac{<\psi^B,\psi'>}{||\psi^B||||\psi'||}$ between the background state and the CLVs, where the bilinear product $< \cdot, \cdot >$ is defined via the kinetic, potential and total energy. The grey shaded areas are the 3 σ confidence intervals. We estimated the effective number of degrees of freedom by dividing the time series into blocks corresponding to the e folding time of the autocorrelation function (Leith, 1973). The x axis indexes the CLVs. Similar results have been obtained for non zonal stationary states (Niehaus, 1981) 32

4.4 Lyapunov Exponents [1/day] for three meridional temperature gradients (dotted: $39.81K$, dashed: $49.77K$, solid: $66.36K$) 36

4.5 Left Side: The three figures show the dependence of the inputs and the conversion of the Lorenz energy cycle on the corresponding Lyapunov exponent for each of the three meridional temperature gradients (dotted: $39.81K$, dashed: $49.77K$, solid: $66.36K$). The magnified view (right side) shows the CLVs with near zero growth rate including the corresponding average eddy observables from the classical Lorenz energy cycle (gray horizontal lines). The y axis units are in 1/day. 37

4.6 Left Side: The four figures show the dependence of the different sinks of the Lorenz energy cycle on the corresponding Lyapunov exponent for each of the three meridional temperature gradients (dotted: $39.81K$, dashed: $49.77K$, solid: $66.36K$). The magnified view (right side) shows the CLVs with near zero growth rate including the corresponding average eddy observables from the classical Lorenz energy cycle (gray horizontal lines). The y axis units are in 1/day. 38

4.7 Left (a, c, e): The mean zonal profiles of Convergence of Momentum Transport. Right (b, d, f): Northward Heat Transport (b, d, f). The x axis indicates the jth CLV. In (a, c, e) the solid lines indicate the sign switch of the barotropic conversion $\mathcal{C}_{BT}$ from positive to negative. In (b, d, f) the dash-dotted lines indicate the sign switch of the baroclinic conversion $\mathcal{C}_{BC}$ from positive to negative. The black dotted lines show the CLV with smallest positive LE. The y axis shows the distribution in the meridional direction in $10^3 km$. 40

4.8 The mean zonal profiles of the conversion of heat $S\omega$ for the three meridional temperature gradients plotted for every CLV ((a) ΔT = 39.81 K, (b) ΔT = 49.77 K and (c) ΔT = 66.36 K). The black vertical dash-dotted lines indicate the change of sign from positive to negative of the baroclinic conversion $\mathcal{C}_{BC}$. The dashed lines indicate the change of sign in the conversion from potential to kinetic energy $\mathcal{C}_{PK}$. The black dotted lines show the CLV with the smallest positive LE. The y-axis shows the distribution in the meridional direction in units of 103 km. The x-axis indicates the j^{th} CLV. 41

4.9 The panels show the average correlation (solid lines) of the subspaces spanned by the n fastest growing CLVs (a) and the n fastest decaying CLVs (b) with the considered trajectories of ΔT (dotted: $39.81K$, dashed: $49.77K$, solid: $66.36K$). The parameter n is indicated on the x axis. The average is done over the mean correlation for different reference points of the CLVs (41 reference points, equally distributed over a 12 years period). The corresponding σ area is indicated by the grey shaded regions. The vertical dashed dotted lines indicate where the expansion includes exactly all baroclinically unstable CLVs (a) or all baroclinically stable CLVs (b). (b) also shows the expansion into a randomly chosen basis (almost diagonal dashed lines). The comparison of both panels shows the higher explanatory power of CLVs with a higher LE. 43

5.1 The number of blocked days is the highest behind the peak of the orography. The vertical black line indicates the peak of the orography. Downstream two secondary maxima can be identified. The x axis indicates the x coordinate where we detect blocking. The y axis shows the frequency of blocking in percent. The grey shaded area shows the range of the blocking rate along the x direction without orography. 51

5.2 As an example of the observed blocking events, the mean blocked state at $x = 15859\,km$ and the unblocked state for $\Delta T = 66\,K$ and $h = 4.44\,km$ is shown. The left panels show the averaged stream function during blocking. The right panels show the average stream function for unblocked periods. The upper panels show the upper layer, the lower panels show the lower layer. The dashed lines show the position of orography. The blocking is affecting the flow only locally because, far from the blocking, the flow is the mean unblocked flow. We get similar results for blockings at different x coordinates and different values of ΔT and h_0. 52

5.3 The distribution of blocking lengths at $x = 15859\,km$ with Orography in comparison to the control run without orography (light grey). The legends show also the lifetime τ of the blocking events and the number of blocked days per year n_b. The y-axis has a log scaling. The total length of the time series is 115705 days (31.7 years). 53

5.4 For the nine setups where we observe blocking (see Figure 5.1), the figure shows the differences in the growth rates during blocking (in blue color) versus unblocked phases (in black color). We additionally show the 3 σ bars of confidence estimated by computing the degrees of freedom of the time series (shaded areas). For $\Delta T = 66K$, $76K$ we can clearly estimate that for the CLVs with highest/lowest LEs the baroclinic conversion increases/decreases significantly. Such a tendency can not be clearly verified for $\Delta T = 50K$ . . 56

5.5 For the nine setups where we observe blocking (see Figure 5.1), this figure compares the baroclinic conversion $\mathcal{C}_{BC}$ during blocking (in blue color) versus unblocked phases (in black color). We additionally show the 3 σ bars of confidence estimated by computing the degrees of freedom of the time series (shaded areas). For $\Delta T = 66K$, $76K$ we can clearly estimate that for the fastest growing CLVs, the baroclinic conversion increases significantly. For the fastest decaying CLVs, a negative tendency can be observed yet with weaker statistical significance. Such a tendency can not be clearly verified for $\Delta T = 50K$. 58

5.6 For the nine setups where we observe blocking (see Figure 5.1), the figure shows the differences in the barotropic conversion $\mathcal{C}_{BT}$ during blocking (in blue color) versus unblocked phases (in black color). We additionally show the 3 σ bars of confidence estimated by computing the degrees of freedom of the time series (shaded areas). For $\Delta T = 66K$, $76K$ we can clearly estimate that for the CLVs with the highest/lowest LEs, the barotropic conversion increases/decreases significantly. For $\Delta T = 50K$, such a tendency can not be clearly verified. 59

5.7 The energy losses of the CLVs are the sum of the Ekman Friction, the heat and eddy diffusivity and newtonian cooling (see Section 4.2). For the nine setups where we observe blocking (see Figure 5.1), the figure shows the sum of these terms during blocking (in blue color) versus unblocked phases (in black color). We additionally show the 3 σ bars of confidence estimated by computing the degrees of freedom of the time series (shaded areas). For all ΔT we can clearly estimate that for the CLVs with the highest/lowest LEs, the energy losses decrease significantly. 60

5.8 Variance of selected covariant Lyapunov vectors (1^{st} (a), 10^{th} (b), 100^{th} (c)). The stream function is shown (left side: ψ_1, right side: ψ_2). The blocked state, which is blocked at the vertical black line, is shown in the upper parts. The unblocked phase is shown in the lower parts. The orography is shown by dashed lines. 62

5.9 Since the localization of the CLVs is similar for the different setups with blocking events, we show here only results for $\Delta T = 66K$ and $h = 4.44\ km$. For every CLV (y-axis) we show the quotient of the meridionally averaged variance during blocking at a particular x coordinate (vertical solid black lines) and unblocked phases ($\Delta\mathcal{L}$ in Equation (5.6)). 64

List of Tables

3.1 Parameters and Variables used in this model and the respective adimensionalization scheme. Note that the scales for time and length are $t = 10^4 s = 1/f_0$ and $L = \frac{10^7}{\pi} m$ 20

4.1 Properties of the attractor 35

4.2 Transports and Conversions - The conversion is positive if the correlation between gradient of the background state and eddy transport of the CLVs is negative. Note that for $\mathcal{C}_{PK}$ the baroclinic stream function ψ_T is proportional to the vertical gradient of the stream function. 42

5.1 Properties of the attractor without Orography 54

5.2 Properties of the attractor with Orography 54

5.3 Metric Entropy during the blocked and the unblocked phase. This is the sum of the in the long term averaged positive LEs averaged during the blocked and unblocked phases, respectively. 55

Acknowledgements

I would like to thank my supervisor Valerio Lucarini for giving me the opportunity to write this thesis on a topic which is exciting and in my view a promising field for the future. Let me also express my sincere thanks to my panel chair Prof. Björn Stevens and my Co-Supervisor Prof. Reiner Lauterbach.

This project would have been impossible without the support of the IMPRS-ESM which allowed me to exclusively focus on my research project and provided a framework for a successful transition of a physicist to the field of meteorology.

I would like to thank Prof. Thomas Frisius for providing the inital version of the QG model.

For the many discussions and support throughout the years, my gratitude goes to Athanasia Nikolaou, Jeroen Wouters, Robert Boschi, Tamas Bodai and Markus Kilian. I would also like to thank Frank Lunkeit, Richard Blender and Christian Franzke for always answering every fundamental question, I had on meteorology in general.

For answering questions regarding clouds, the weather and all that or ensuring that I don't miss any retreats and that sort of things: Malte Rieck, David Bröhan, Sebastian Schirber and Ulrike Port.

For support and being there: Lisa.

Aus dieser Dissertation hervorgegangene Vorveröffentlichungen und Einsendungen

List of Publications and Submissions

Schubert, S., Lucarini, V. (2015). Covariant Lyapunov vectors of a quasi-geostrophic baroclinic model: analysis of instabilities and feedbacks. Quarterly Journal of the Royal Meteorological Society, n/a-n/a. doi:10.1002/qj.2588

Schubert, S., & Lucarini, V. (2015): Dynamical Analysis of Blocking Events: Spatial and Temporal Fluctuations of Covariant Lyapunov Vectors, submitted to QJRMS.

Eidesstattliche Versicherung

Declaration on Oath

Hiermit erkläre ich an Eides statt, dass ich die vorliegende Dissertationsschrift selbst verfasst und keine anderen als die angegebenen Quellen und Hilfsmittel benutzt habe.

I hereby declare, on oath, that I have written the present dissertation by myself and have not used other than the acknowledged resources and aids.

Hamburg, den March 9, 2016